15

NASA Contractor Report 3813

Propeller Aircraft Interior Noise Model

L. D. Pope, E. G. Wilby,
and J. F. Wilby

CONTRACT NAS1-15782
JULY 1984

NASA Contractor Report 3813

Propeller Aircraft Interior Noise Model

L. D. Pope, E. G. Wilby,
and J. F. Wilby
Bolt Beranek and Newman Inc.
Canoga Park, California

Prepared for
Langley Research Center
under Contract NAS1-15782

National Aeronautics
and Space Administration

**Scientific and Technical
Information Branch**

1984

Page intentionally left blank

Page intentionally left blank

TABLE OF CONTENTS

TABLE OF CONTENTS
(Continued)

TABLE OF CONTENTS
(Continued)

LIST OF FIGURES

LIST OF FIGURES
(Continued)

LIST OF FIGURES
(Continued)

LIST OF TABLES

Appendix - Table No. Page

1.0 SUMMARY

An analytical model for aircraft interior noise prediction is considered in this report. The model can be used to predict the sound levels inside an airplane cabin caused by the rotation of a propeller (of any design) alongside. The fuselage model is that of a cylinder with a structurally integral floor. The cabin sidewall and the floor are stiffened by ring frames and stringers or floor beams of arbitrary configurations. The cabin interior is covered with a trim (i.e., layers of insulation and septa with a lining) to increase the sidewall sound isolation and provide absorption in the cabin.

The results are the culmination of a three phase program sponsored by NASA Langley Research Center. In Phase I the basic analytical modeling of the transmission problem (interaction of the structure with the exterior and interior acoustic fields) was undertaken and preliminary validation studies were completed using an unpressurized, unstiffened cylinder as a test article. Results of that work are presented in Reference [3]. In Phase II, the general aircraft interior noise model was developed and preliminary work on the laying out of the basic master computer program began. Validation studies were conducted using more advanced test articles (one being a stiffened cylinder with a floor partition and interior trim). Results of that work are found in References [4] and [7]. In Phase III, the analytical models and the software were completed (including the propeller excitation work). Validation studies using a scale model fuselage excited by a propeller were undertaken and the documentation of the finalized model and software package was completed.

The present model is believed to be the only one in existence that can be used to calculate the interior sound levels using as input data, the precise propeller noise signature over the fuselage.

2.0 INTRODUCTION

This report presents the details of a basic airplane interior noise model. The elements of this model include a fuselage and a propeller (Figures 1 and 2). The fuselage consists of a cylinder stiffened by ring frames and stringers, and a floor that is structurally an integral part of the fuselage. The cabin space is the volume above the floor. The interior surface of the cabin (sidewall) is finished out with a trim consisting of insulation covered with a lining. The propeller rotates about an axis parallel to the centerline of the fuselage. The model can be used to predict the sound levels in the cabin space for each of the various harmonics of the propeller.

The excitation of the exterior of the fuselage is obtained using a propeller noise prediction model developed by NASA Langley. The present model works with the pressure time histories (signatures) as defined over the fuselage at a number of closely spaced points on a grid that lies in the fuselage skin. The pressure signatures are Fourier analyzed to define the amplitudes and phases of each of the harmonics of the propeller tones (at each location on the grid). The cross power spectral density function for each harmonic, for all grid point pairs (a delta function in the frequency domain) is used to compute the values of the generalized forces for each structural mode of the fuselage.

The fuselage structural modes are developed for the case of a stiffened cylinder with a floor partition. The structural modes are described by their eigenvalues (resonance frequencies), eigenvectors (mode shapes), and loss factors. The mode shapes include not only the cylinder wall normal displacement (w component) but also the normal displacement of the floor, and the in-plane axial and circumferential displacements (u and v components) of cylinder and floor as well. The loss factors of

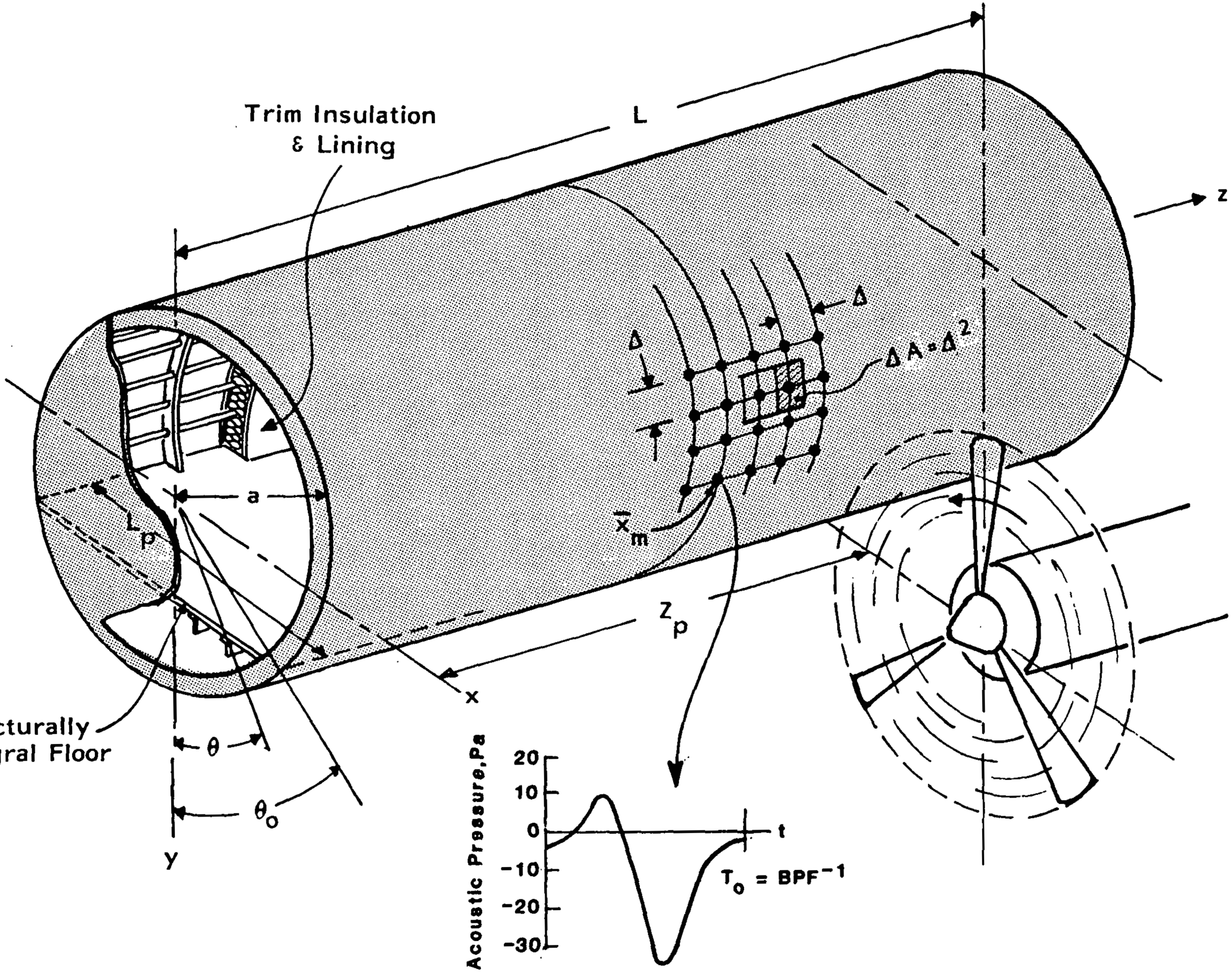

FIGURE 1. PROPELLER AIRCRAFT INTERIOR NOISE MODEL

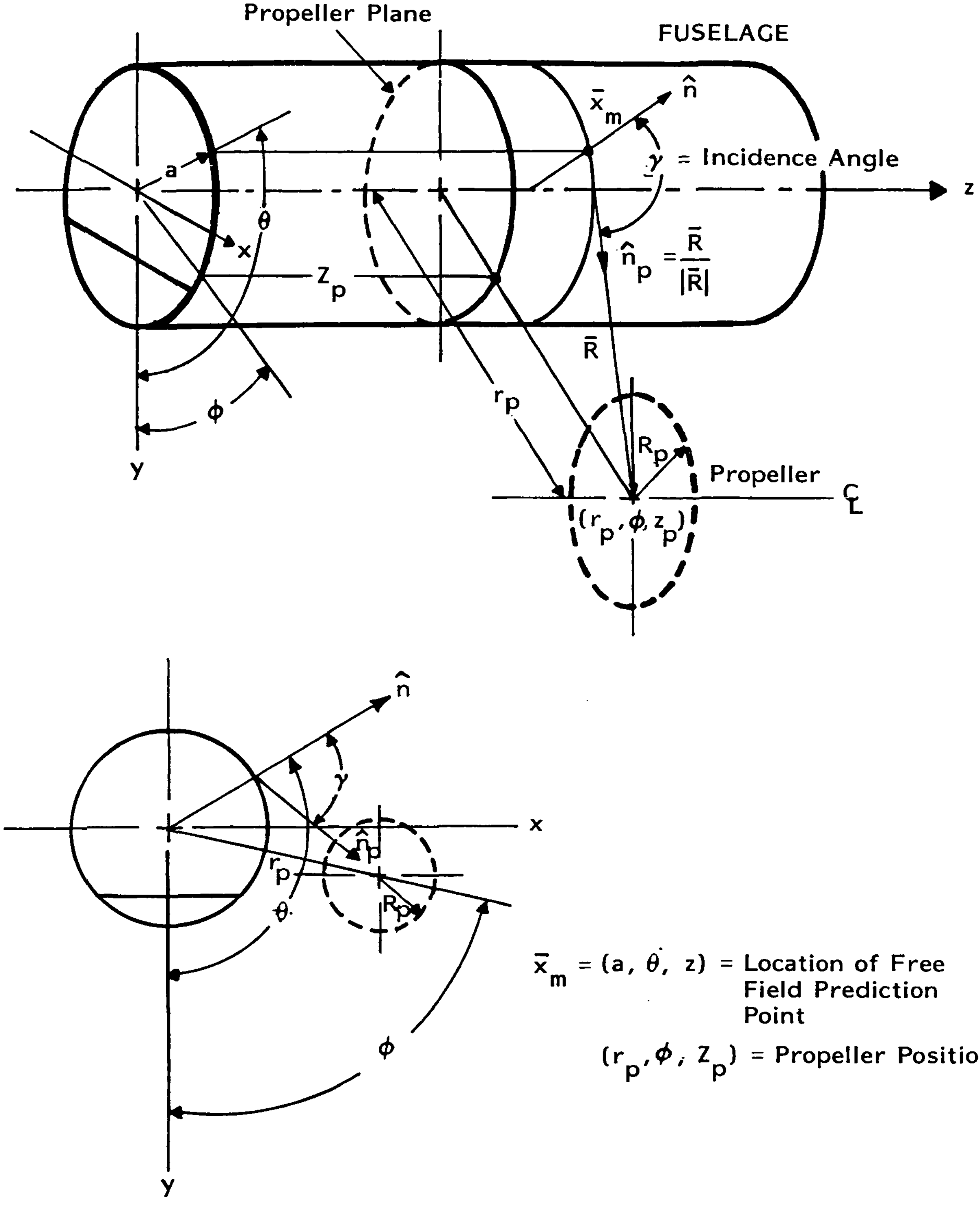

$\bar{x}_m = (a, \theta, z)$ = Location of Free Field Prediction Point

(r_p, ϕ, Z_p) = Propeller Position

FIGURE 2. PROPELLER AND FUSELAGE SURFACE POINT GEOMETRY

the bare fuselage are input and must come from measurements. When trim is installed on the sidewall, the structural losses increase due to the trim's presence against the sidewall and this is computed for the particular trim installation.

The displacement of the trim lining induced by the fuselage skin vibration is determined using a transfer matrix which relates the pressures on the inside of the skin and the inside of the lining to the displacement of the skin and of the lining. The transfer matrix contains all of the physical properties of the insulation and lining required for the calculation. The wave impedance of the insulation and complex acoustic wavenumber are input as physical parameters to describe the insulation.

The coupling of the lining to the interior acoustic field is calculated for each acoustic and structural mode. The acoustic modes are defined by their resonance frequencies, mode shapes, and loss factors. The acoustic loss factors must be input for a bare fuselage but are calculated when a cabin trim is installed, from elements of the trim transfer matrix.

The model allows for the calculation of the space average mean square pressure in the cabin for each propeller harmonic (up to a maximum of ten (10) harmonics).

2.1 Report Organization

This report considers the analytical derivations, experimental tests, and validation studies. The analytical derivations are presented in Section 3 and Appendices A through D. Appendix E is devoted to test comparisons and to the determination of the quality of the predictions. Appendix F is a list of symbols used.

Early in Section 3, general solutions are given for the basic sound transmission problems of concern. Problems of tone transmission (propeller) and noise transmission (reverberant exterior field) are considered. Solutions that are to be used in the low and high frequency regimes are presented (the low frequency formulations apply until the acoustic modal density of the cabin space is equivalent to 10 to 15 modes in every one-third octave band). Beginning with Section 3.4, the various terms appearing in the general solutions are evaluated, literally specialized to create the desired interior noise model. These terms include the generalized forces for propeller noise excitation, interior coupling factors, joint acceptances, resonance frequencies and loss factors. Information needed to complete these calculations are derived in the first four appendices.

The model validation undertaken in Phase III is considered in Appendix E. The experiment and the data acquired are discussed and a statistical comparison of predictions and measurements is presented.

2.2 Program Management

The work was accomplished in joint effort by BBN/Los Angeles and NASA Langley Research Center. The experimental work was done at NASA Langley by C. M. Willis and W. H. Mayes. Mr. Mayes acted as LaRC technical representative of the contracting officer (TRCO). L. D. Pope served as BBN program manager.

3.0 ELEMENTS OF THE PROPELLER AIRCRAFT INTERIOR NOISE MODEL

A detailed description of the propeller aircraft interior noise prediction model is given in the following paragraphs. It is the intention of the authors to present all of the background needed to understand the equations and their origins. This is done partly through the use of a series of Appendices that summarize the primary results from two previous phases and the now concluding phase of work that have led to the present model. References to some published papers and books are also required.

A concern in this report is to define a reasonable level at which to begin the technical presentation. This model is based on the general solutions of sound transmission problems for cases of tonal and broadband noise excitations. Parts of the report deal with the theory of fluid-structure interaction problems with direction at the development of a sufficiently general solution as needed for the present purpose. Because the propeller is an integral part of the model the field of "aeroacoustics" is inherently involved. Due to the complexity of the fuselage models and the geometry of the cabin space, the structural dynamics of stiffened shell structures must be considered and numerical procedures for calculation of the acoustic characteristics of complex spaces devised. The presence of sidewall trim (insulation and lining) leads to the use of the properties of porous materials.

The ultimate user of this model will not necessarily be knowledgeable in all of these areas. For instance, one well versed in the fluid-structure intraction problem may have little or no experience in propeller noise. Keeping this in mind, an effort has been made to ease the transition between the various disciplines and the introduction to each topic is kept at what might be considered an intermediate level.

3.1 General Solution for the Sound Transmission Problem

The fundamental goal of this model is the prediction of the sound level inside an airplane cabin due to noise on the exterior caused by the rotation of a propeller. The propeller noise of concern is at discrete frequencies and is not really a noise at all, rather a series of tones. The lowest frequency tone is at the blade passage frequency (BPF) and the other tones are its harmonics, that is, they occur at frequencies that are integral multiples of the BPF. As a secondary goal of this model, predictions for the cases of an arbitrary exterior harmonic (tonal) field and for a reverberant exterior (noise) field are sought. Sound transmission through the fuselage sidewall and the trim insulation and lining is of concern.

The basic method used herein to solve the sound transmission problem is that of a power balance.

$$W_{in} = W_{diss} \quad . \tag{1}$$

The band-limited net time-averaged power, W_{in}, flowing into the cabin must equal the net time-averaged power, W_{diss}, dissipated on the cabin walls. By expressing the inflowing power in terms of the exterior exciting pressure and the dissipated power in terms of the interior response pressure and equating the expressions according to Eq.(1), one can solve for the interior pressure.

A primary feature of the power flow approach adopted is that integration of spectral components has been performed analytically to achieve band-limited levels, i.e.,

$$W_{in} = \int_{\Delta\omega} \mathrm{Re}\left[W_{rad}^{int}(\omega)\right] d\omega$$
$$W_{diss} = \int_{\Delta\omega} \mathrm{Re}\left[W_{abs}^{int}(\omega)\right] d\omega \quad . \tag{2}$$

$W_{rad}^{int}(\omega)$ is the complex spectral density of the power radiated by the structure into the interior acoustic space and $W_{abs}^{int}(\omega)$ is the spectral density of power absorbed on the inner wall of the space from the interior acoustic field. In the case of tone transmission, these quantities contain delta functions in the frequency domain. Eqs. (2) have applicability at all frequencies and can be applied in discrete modal representations even when there are no acoustic or structural modes resonant in the band $\Delta\omega$.

Power flow into each individual acoustic mode is computed, whether the mode is resonant in the band or not. If the mode is resonant in the band, one can speak of the "resonant response" of the mode; if the mode is resonant outside the band, the "nonresonant response" of the mode *in the band* $\Delta\omega$. Similarly power flowing out of the acoustic field to the inside wall is computed mode-by-mode. By equating the power into a mode to the power out, the space-average mean-square modal pressure for mode n, limited to band $\Delta\omega$, is obtained, i.e., $\langle p_n^2 \rangle_{s,t}$, where s and t indicate the space and time averages, respectively. The band-limited, space-average mean-square pressure in the interior is the sum

$$\langle p_i^2 \rangle_{s,t} = \sum_n \langle p_n^2 \rangle_{s,t} \quad . \tag{3}$$

Here n is the complete set of acoustic modes, i.e., those resonant inside $\Delta\omega$ (denoted by the symbolism, $n \in \Delta\omega$), as well as those resonant above ($n > \Delta\omega$) and below $\Delta\omega$ ($n < \Delta\omega$). It is noted here that the letter "n" always denotes acoustic modes and the letter "r" structural modes, usually being used as subscripts, superscripts, or indexes.

Power Flow

The concern is with a closed volume V, into which sound energy is propagating. The excitation of the space occurs at its boundary with the enclosing structure which vibrates due to an exterior source. For the present, the excitation can be considered to be a broadband random acoustic field. For the specific case where the noise reduction is desired, the exterior field is taken to be diffuse (reverberant).

The fundamental equation for the inflowing power comes from results developed in Refs. [1] and [2]. Specifically, use is made of Eq.(3) of Ref. [2]:

$$W_{in} = \frac{\rho c_o^2 A^4}{V} S_{pbl}(\omega) \sum_r \frac{j_r^2(\omega)}{M_r^2 \omega_r^4} \sum_n \frac{\varepsilon_n \eta_n f'^2(n,r)}{\omega_n^2}$$
$$\times \int_{\Delta\omega} \frac{\omega^3 d\omega}{\{[1-(\omega^2/\omega_n^2)]^2+\eta_n^2\}\{[1-(\omega^2/\ \omega_r^2)]^2+\eta_r^2\}} \ . \qquad (4)$$

W_{in} is the band-limited time averaged power which is being accepted by the acoustic field inside the enclosure, that is, the power received over frequencies lying in band $\Delta\omega$. The band has a width $\Delta\omega = c_\omega \omega$ where ω is the center frequency of the band. c_ω is a constant percentage which defines the bandwidth

(c_ω = 0.232 for one-third octaves). The quantity $S_{pbl}(\omega) = \langle p_{bl}^2 \rangle / c_\omega \omega$ is the power spectral density of the average exciting "blocked pressure" which acts on the transmitting structure. $\langle p_{bl}^2 \rangle$ is the average mean-square pressure as would be measured in band $\Delta\omega$ obtained with a microphone sampling the surface pressure on the (hypothetical) immobilized (blocked) structure. The transmitting structure has an area A exposed to volume V. The average surface mass of the structure is m. The structure has a mass law sound transmission coefficient $\tau_{ML} = (2\rho c_o/\omega m)^2$, where ρ and c_o are the density and sound speed of air.

The normalization of structural modes is taken such that the modal mass is

$$M_r = \int_{\bar{x}} m(\bar{x}) \psi^{r^2}(\bar{x}) d\bar{x} \quad ,$$

where $\psi^r(\bar{x})$ is the structural mode shape (mode r) at location $\bar{x}$. $\bar{x}$ ranges over the entire structure, both transmitting and non-transmitting surfaces. Thus, if the rth mode of the transmitting structure (fuselage) is restrained in any way, say perhaps by the cabin floor, M_r will take on a large value that will suppress transmission by that particular mode. The normalization of the acoustic modes is such that

$$\int_V \phi_n^2 d\bar{v} = \frac{V}{\varepsilon_n} \quad ,$$

where $\phi_n(\bar{\xi})$ is the value of the cabin acoustic mode shape (mode n) at location $\bar{\xi}$.

The coupling of the exterior field to the rth mode of the transmitting structure is given in terms of the joint acceptance $j_r^2(\omega)$. In the case where the exterior field is a noise it is assumed that $j_r^2(\omega)$ changes little across $\Delta\omega$, i.e. by evaluating $j_r^2(\omega)$ at the center frequency of the band, a good approximation is obtained all across $\Delta\omega$. For this reason $\Delta\omega$ must not be too wide, typically one-third octave or less. If the exterior field is reverberant, $j_r^2(\omega)$ takes the appropriate form for that field. The same would be true for a progressive wave field.

The coupling of a structural mode to an acoustic mode of the volume is given by the term

$$f'(n,r) = \frac{1}{A}\int_A \phi_n(\bar{x})\psi^r(\bar{x})d\bar{x} \quad .$$

In the above, $\bar{x}$ represents a point on the surface of the transmitting structure. Note that $f'(n,r)$ is non-dimensional (hence the prime as a reminder) and that $f'(n,r)$ is always squared. $f'^2(n,r)$ is a positive number less than unity. The power flow depends on the location of the resonance frequencies ω_n and ω_r, i.e. relative to each other and to the band $\Delta\omega$, and upon the acoustic and structural loss factors η_n and η_r.

Consider now the right-hand side of Eq. (1). W_{diss} is the band-limited, time-averaged power that flows out of the interior acoustic field to the inner wall of the enclosure. This power flow is given by Eqs. (6) and (8) of Section III of [2] which reduce to

$$W_{diss} = \frac{V}{\rho c_o^2} \sum_n \frac{\eta_n \omega_n^2}{\omega} \langle p_n^2 \rangle_{s,t} \quad , \tag{5}$$

where $\langle p_n^2 \rangle_{s,t}$ is the interior space-average mean-square pressure in band $\Delta\omega$ attributable to the nth acoustic mode. The development of Eq. (5) is presented in the appendix of [2].

In the case of a random exterior field, in which $S_{pbl}(\omega)$ varies slowly in frequency, $j_r^2(\omega)$ can be brought outside the integral as done in Eq. (4). However, for the general circumstance where tones are present, $j_r^2(\omega)$ must be included under the integral sign, and replaced by its defining relation

$$j_r^2(\omega) = \frac{\iint C_{pbl}(\bar{x}|\bar{x}';\omega)\psi^r(\bar{x})\psi^r(\bar{x}')d\bar{x}d\bar{x}'}{\bar{A}^2 S_{pbl}(\omega)} \quad ,$$

where $C_{pbl}(\bar{x}|\bar{x}';\omega)$ is the cospectral density function of the blocked exterior pressure field.

Also, in order to get Eq. (4) in the desired form for the present model it must be modified in two other respects. First, to include fuselage sidewall trim, Eq.(4) is modified to include factor τ_t, i.e. the trim transmission coefficient, to account for transmission through the trim, and the structural loss factor η_r is replaced by η_r' to account for the added damping of the sidewall when trim is present. Second, proper account of the influence of the internal radiation damping of structural modes leads to the introduction of another term, η_r''. The analytical developments for τ_t and η_r' are given in Appendix A; η_r'' will be discussed in a subsequent section. After some rearrangement and the inclusion of the above results, Eq. (4) can be written in the following general form

$$W_{in} = \frac{2\pi}{\rho V}\left(\frac{mA}{4}\right)^2 \tau_{ML}\,\frac{2}{\pi}\,\omega^2 \sum_n \frac{\varepsilon_n \eta_n}{\omega_n^2}$$

$$\times \sum_r \frac{\bar{f}'^2(n,r)}{M_r^2\omega_r^4} \int_{\Delta\omega} \int_{\bar{x}}\int_{\bar{x}'} C_{p_{bl}}(\bar{x}|\bar{x}';\omega)\psi^r(\bar{x})\psi^r(\bar{x}')d\bar{x}d\bar{x}'$$

$$\times \frac{\omega^3 d\omega}{\left[\left(1-\frac{\omega^2}{\omega_n^2}\right)^2 + \eta_n^2\right]\left[\left(1-\frac{\omega^2}{\omega_r^2}\right)^2 + (\eta_r'+\eta_r'')^2\right]} \, . \qquad (6)$$

A bar over f'(n,r) indicates trim factor τ_t has been introduced. Eq. (6) is basically the same as Eq. (21) of Ref. [3], except modified to include trim and the proper influence of the internal radiation damping of resonant structural modes closely coupled in frequency to resonant acoustic modes.

The solution of a sound transmission problem is obtained by setting the nth term of Eq. (5) equal to the nth term of Eq.(6), solving for the individual modal pressures $<p_n^2>_{s,t}$ one-by-one, and by adding the results according to Eq. (3), to obtain the interior level.

3.2 Transmission of a Tone

The fundamental model of concern here is one having to do with tone transmission. The propeller noise is, as stated, at discrete frequencies, each tone being a harmonic of the BPF. Let the various harmonics be ω_1, ω_2, ..., ω_H where

$$\begin{aligned} \omega_1 &= 2\pi \text{ x BPF} \\ \omega_2 &= 2\omega_1 \\ \omega_H &= H\omega_1 \quad , \end{aligned}$$

where H is the harmonic index. For a tone at frequency ω_H, the co-spectral density function is defined by

$$C_{p_{bl}}(\bar{x}|\bar{x}')\ \delta(\omega-\omega_H) = C_{p_{bl}}(\bar{x}|\bar{x}';\omega) \quad ,$$

$$C_{p_{bl}}(\bar{x}|\bar{x}';\omega) = 2\ \bar{C}_{p_{bl}}(\bar{x}|\bar{x}';\omega)\ ; \quad 0 \le \omega < \infty \quad ,$$

$$\bar{C}_{p_{bl}}(\bar{x}|\bar{x}';\omega) = \mathrm{Re}\left[\frac{1}{2\pi}\int_{-\infty}^{\infty} R_{p_{bl}}(\bar{x}|\bar{x}';\tau)\ e^{i\omega\tau}d\tau\right] \quad ,$$

where $R_{p_{bl}}(\bar{x}|\bar{x}';\tau)$ is the average cross correlation of the pressure over the blocked (immobile) fuselage, given by

$$R_{p_{bl}}\ (\bar{x}|\bar{x}';\tau) = \lim_{T\to\infty}\ \frac{1}{T}\int_{-\frac{T}{2}}^{\frac{T}{2}} \mathrm{Re}\left[p_{bl}(\bar{x},t)\right]\ \mathrm{Re}\left[p_{bl}(\bar{x}',t+\tau)\right]\ dt.$$

Inserting the first of the relations into Eq. (6) leads to the expression for the inflowing power to the cabin for the propeller tone at frequency ω_H.

$$W_{in} = \frac{2\pi}{\rho V}\left(\frac{mA}{4}\right)^2 \tau^H_{ML} \frac{2}{\pi}\, \omega_H^2 \sum_n \frac{\varepsilon_n \eta_n}{\omega_n^2}$$

$$\cdot \sum_r \frac{\bar{f}'^2(n,r)}{M_r^2 \omega_r^4} \int_{\bar{x}} \int_{\bar{x}'} C_{p_{bl}}(\bar{x}|\bar{x}')\psi^r(\bar{x})\psi^r(\bar{x}')d\bar{x}d\bar{x}'$$

$$\cdot \frac{\omega_H^3}{\left[\left(1-\frac{\omega_H^2}{\omega_n^2}\right)^2 + \eta_n^2\right]\left[\left(1-\frac{\omega_H^2}{\omega_r^2}\right)^2 + \left(\eta_r' + \eta_r''\right)^2\right]} \quad . \qquad (7)$$

In this result, τ^H_{ML} and τ^H_t (in $\bar{f}'(n,r)$) are evaluated at ω_H.

The space average mean square modal pressure is computed on a mode-by-mode basis using Eqs. (1), (5), and (7) (where $\omega = \omega_H$):

$$\langle p_n^2\rangle^H_{s,t} = \frac{4c_o^2}{V^2}\left(\frac{mA}{4}\right)^2 \tau^H_{ML} \frac{\omega_H^6\, \varepsilon_n}{\omega_n^4} \cdot \sum_r \frac{\bar{f}'^2(n,r)}{M_r^2\omega_r^4}$$

$$\times \int_{\bar{x}}\int_{\bar{x}'} C_{pbl}(\bar{x}|\bar{x}')\psi^r(\bar{x})\psi^r(\bar{x}')d\bar{x}d\bar{x}'$$

$$\times \frac{1}{\left[\left(1-\frac{\omega_H^2}{\omega_n^2}\right)^2 + \eta_n^2\right]\left[\left(1-\frac{\omega_H^2}{\omega_r^2}\right)^2 + (\eta_r' + \eta_r'')^2\right]} \quad . \qquad (8)$$

The interior space average level is then obtained from Eq. (3). Note that since

$$\langle p_n^2\rangle^H_{s,t} = \frac{\langle p_n^2\rangle^H}{V}\int \phi_n^2 d\bar{v} \quad ,$$

where $<p_n^2>^H$ is the mean square modal amplitude, the modal amplitude is determinable from

$$<p_n^2>^H = \varepsilon_n <p_n^2>^H_{s,t} \quad ,$$

and theoretically, the mean square pressure at every interior point can be obtained with

$$<p_i^2(\bar{\xi},\omega)>^H_t = \sum_n \varepsilon_n <p_n^2>^H_{s,t} \phi_n^2(\bar{\xi}) \quad . \tag{9}$$

It is emphasized here that a good point-by-point prediction may require better input data than can ever be generated, but the point-by-point prediction might be quite informative nevertheless.

Eq.(8) is the fundamental result for calculating the interior sound pressure level. The modal forcing functions are given by the term

$$\Psi_G(r,H) = \int_{\bar{x}} \int_{\bar{x}'} C_{p_{bl}}(\bar{x}|\bar{x}')\psi^r(\bar{x})\psi^r(\bar{x}')d\bar{x}d\bar{x}' \ , \tag{10}$$

and must be evaluated for the propeller noise excitation. Once a particular harmonic H is chosen, the function $\Psi_G(r,H)$ must be computed for all structural modes r. The calculation of $\Psi_G(r,H)$ using the output from the ANOPP program [Ref.5] is considered in Section 3.4.

High Frequencies

When the acoustic and structural modal densities are large enough, the transmission can be expected to be dominated by modal response close to the excitation frequency. Only the modes lying in a narrow band $\Delta\omega$ containing ω_H need be of concern. Thus at sufficiently high frequencies the space average mean interior pressure for harmonic H is (assuming that only the sidewall contributes)

$$<p_i^2>^H_{s,t} = \frac{4c_o^2}{V^2}\left(\frac{mA}{4}\right)^2 \tau^H_{ML}\tau^H_t\omega_H^6 \sum_{n\epsilon\Delta\omega} \frac{\epsilon_n}{\omega_n^4}$$

$$\times \sum_{r\epsilon\Delta\omega} \frac{f'^2(n,r)}{M_r^2\omega_r^4}\left\{\int_{\bar{x}}\int_{\bar{x}'} C_{p_{bl}}(\bar{x}|\bar{x}')\psi^r(\bar{x})\psi^r(\bar{x}')d\bar{x}d\bar{x}'\right\}$$

$$\times \frac{1}{\left[\left(1-\frac{\omega_H^2}{\omega_n^2}\right)^2 + \eta_n^2\right]\left[\left(1-\frac{\omega_H^2}{\omega_r^2}\right)^2 + (\eta_r' + \eta_r'')^2\right]} \quad . \qquad (11)$$

To facilitate the calculation of Eq.(11), it first is rearranged (keeping in mind that $\Psi_G(r,H)$ is computed for high frequencies for each structural mode as it is for low frequencies, but the calculation is limited to those modes whose resonance frequencies lie close to ω_H). Define average loss factors for the modes near ω_H, i.e., let

$$\eta_n \simeq \bar{\eta}_n ; \; \eta_r' + \eta_r'' \simeq \bar{\eta}_r$$

$\bar{\eta}_r$ is the average loss factor for the structural modes. Also, let

$$g_n(\omega_H/\omega_n) = \left[\left(1-\frac{\omega_H^2}{\omega_n^2}\right)^2 + \bar{\eta}_n^2\right]^{-1}$$

$$g_r(\omega_H/\omega_r) = \left[\left(1-\frac{\omega_H^2}{\omega_r^2}\right)^2 + \bar{\eta}_r{}^2\right]^{-1}$$

$$Q_H = \frac{4c_o^2}{V^2}\left(\frac{mA}{4}\right)^2 \tau^H_{ML}\tau^H_t\omega_H^6 \quad .$$

Then Eq.(11) can be written as

$$\langle p_i^2\rangle^H_{s,t} = Q_H \sum_{n\varepsilon\Delta\omega} \frac{\varepsilon_n g_n}{\omega_n^4} \sum_{r\varepsilon\Delta\omega} \frac{f'^2(n,r)\, g_r \Psi_G(r,H)}{M_r^2 \omega_r^4} \quad . \qquad (12)$$

The interior response is sought for the case where ω_n and ω_r are given equal probabilities of lying anywhere in the band $\Delta\omega$.

Eq.(12) can be simplified somewhat by noting that the resonance frequencies are approximately equal to the harmonic frequency ω_H of concern.

$$\langle p_i^2\rangle^H_{s,t} = \frac{Q_H}{\omega_H^8} \sum_{n\varepsilon\Delta\omega} \varepsilon_n g_n \sum_{r\varepsilon\Delta\omega} \frac{f'^2(n,r)}{M_r^2} g_r \Psi_G(r,H) \quad . \qquad (13)$$

The expected value of the above is now calculated given ω_n and ω_r as independent random variables uniformly distributed across $\Delta\omega$.

$$E\left[\langle p_i^2\rangle^H_{s,t}\right] = E\left[\frac{Q_H}{\omega_H^8} \sum_{n\varepsilon\Delta\omega} \varepsilon_n g_n \sum_{r\varepsilon\Delta\omega} \frac{f'^2(n,r)}{M_r^2} g_r \Psi_G(r,H)\right]$$

$$= \frac{Q_H}{\omega_H^8} \frac{1}{N_n} \sum_{n\varepsilon\Delta\omega} N_n \varepsilon_n E\left[g_n\right] \frac{1}{N_r} \sum_{r\varepsilon\Delta\omega} N_r \frac{f'^2(n,r) E}{M_r^2} \left[g_r\right] \Psi_G(r,H) \quad . \qquad (14)$$

In Eq.(14), N_r is the number of structural modes in $\Delta\omega$ and N_n is the number of acoustic modes in $\Delta\omega$.

Now

$$E\left[g_n\right] = \int_{\Delta\omega} g_n(\omega_H/\omega_n)\, p(\omega_n)\, d\omega_n \qquad ,$$

where $p(\omega_n)$ is the probability density function for ω_n in $\Delta\omega$.

The probability distribution function is taken to be simply

$$P(\omega_n) = \frac{\omega_n - \omega_H}{\Delta\omega} + \frac{1}{2} \quad .$$

The probability density function is therefore simply

$$p(\omega_n) = \frac{dP(\omega_n)}{d\omega_n} = \frac{1}{\Delta\omega} \qquad ,$$

so

$$E[g_n] = \frac{1}{\Delta\omega} \int_{\Delta\omega} g_n(\omega_H/\omega_n)\, d\omega_n \qquad ,$$

that is $E[g_n]$ is just the average

$$E[g_n] = \frac{1}{\Delta\omega} \int_{\omega_H - \frac{\Delta\omega}{2}}^{\omega_H + \frac{\Delta\omega}{2}} \frac{d\omega_n}{(1-\omega_H{}^2/\omega_n^2)^2 + \bar{\eta}_n^2} \qquad ,$$

which becomes

$$= \frac{\omega_H}{2\bar{\eta}_n \Delta\omega} \left[\tan^{-1}\left(\frac{\Delta\omega}{\bar{\eta}_n \omega_H}\right) - \tan^{-1}\left(\frac{-\Delta\omega}{\bar{\eta}_n \omega_H}\right)\right] \quad .$$

Assuming that the product $\bar{\eta}_n \omega_H << \Delta\omega$ (this can be assured by taking the sampling band wide enough), the term in the brackets, [ ], above reduces to π, giving

$$E\left[g_n\right] = \frac{\pi \omega_H}{2\bar{\eta}_n \Delta\omega} \quad .$$

Similarly, it can be shown that

$$E[g_r] = \frac{\pi\omega_H}{2\bar{\eta}_r\Delta\omega}$$

Substituting into Eq.(14) gives

$$E\left[\langle p_i^2\rangle^H_{s,t}\right] = \frac{Q_H}{\omega_H^8}\,\frac{1}{N_n}\sum_{n\varepsilon\Delta\omega}\varepsilon_n\left(\frac{N_n}{\Delta\omega}\right)\left(\frac{\pi\omega_H}{2\bar{\eta}_n}\right)$$

$$\times\left[\frac{1}{N_r}\sum_{r\varepsilon\Delta\omega}\frac{f'^2(n,r)}{M_r^2}\Psi_G(r,H)\left(\frac{N_r}{\Delta\omega}\right)\left(\frac{\pi\omega_H}{2\bar{\eta}_r}\right)\right] .$$

But $n_n = N_n/\Delta\omega$ is the modal density of the acoustic modes, and

$n_r = N_r/\Delta\omega$ is the modal density of the structural modes.

Therefore

$$E\left[\langle p_i^2\rangle^H_{s,t}\right] = \frac{\pi^2 c_o^2}{V^2}\,\frac{n_r n_n}{\bar{\eta}_r\bar{\eta}_n}\left(\frac{mA}{4}\right)^2\tau^H_{ML}\tau^H_t\left[\frac{1}{N_r}\sum_{r\varepsilon\Delta\omega}\frac{\Psi_G(r,H)}{M_r^2}\langle\varepsilon_n f'^2(n,r)\rangle_{\Delta\omega}\right] \quad (15)$$

where

$$\langle\varepsilon_n f'^2(n,r)\rangle_{\Delta\omega} = \frac{1}{N_n}\sum_{n\varepsilon\Delta\omega}\varepsilon_n f'^2(n,r) \quad .$$

It can be shown that

$$n_n\langle\varepsilon_n f'^2(n,r)\rangle_{\Delta\omega} \simeq \frac{\omega_H^2 V}{\pi^2 c_o^3}\,j_r^{2\,\mathrm{rev}}(\omega_H) \quad .$$

Substituting this result gives

$$E\left[\langle p_i^2\rangle^H_{s,t}\right] = \frac{\omega_H^2}{c_o V}\,\frac{n_r \tau_{ML}^H\,\tau_t^H}{\bar{\eta}_r \bar{\eta}_n}\left(\frac{mA}{4}\right)^2\left[\frac{1}{N_r}\sum_{r\varepsilon\Delta\omega}\frac{\Psi_G(r,H)}{M_r^2}\;j_r^{2\,rev}(\omega_H)\right] \tag{16}$$

In (16), $\Delta\omega$ is taken just wide enough to assure smoothness of the average calculated in the brackets.

3.3 Calculation of the Noise Reduction

In addition to the calculation of transmission of propeller noise, there may be occasions where the noise reduction of the fuselage is of interest, that is, for a condition where the exterior is bathed in a reverberant (diffuse) acoustic field. For such a case, the expression for the inflowing power is again obtained from Eq.(6). However, in this instance, the joint acceptance can be reinserted and brought outside the integral as in Eq.(2). Then after the integration is performed, it is found that [2]

$$\begin{aligned}
W_{in} = {} & \frac{\langle p_{bl}^2\rangle}{c_\omega \omega}\,\frac{2\pi\bar{A}^2}{\rho V}\left(\frac{mA}{4}\right)^2 \tau_{ML}\cdot\sum_n \varepsilon_n \eta_n \\
& \cdot\sum_r \frac{j_r^2(\omega)\bar{f}'^2(n,r)}{M_r^2}\left\{\frac{2}{\pi}\,\frac{\omega^2\omega_n^2}{D_{nr}}\left[\left(\frac{c_r - c_n}{4}\right)\ln_n\right.\right. \\
& + \left(\frac{2c_n(b_r-b_n)-b_n(c_r-c_n)}{4\eta_n\omega_n^2}\right)\arctan_n + \left(\frac{c_n-c_r}{4}\right)\ln_r \\
& \left.\left. + \left(\frac{2c_r(b_n-b_r)-b_r(c_n-c_r)}{4(\eta_r' + \eta_r'')\omega_r^2}\right)\arctan_r\right]\right\}\,,
\end{aligned} \tag{17}$$

where $\bar{A}$ is the cylinder surface area and A is the coupling area.

For n or r = j,

$$\ln_j = \ln\left\{\frac{|(1+c_\omega/2)^4\omega^4+b_j(1+c_\omega/2)^2\omega^2+c_j|}{|(1-c_\omega/2)^4\omega^4+b_j(1-c_\omega/2)^2\omega^2+c_j|}\right\} ,$$

$$\arctan_j = \tan^{-1}\left[\frac{(2+c_\omega)^2\omega^2-4\omega_j^2}{4\eta_j\omega_j^2}\right] -\tan^{-1}\left[\frac{(2-c_\omega)^2\omega^2-4\omega_j^2}{4\eta_j\omega_j^2}\right]$$

where when $j = r$, η_j above $= \eta_r' + \eta_r''$, and when $j = n$, $\eta_j = \eta_n$. Also

$$D_{nr} = (c_r-c_n)^2 + (b_n-b_r)(b_nc_r - b_rc_n) ,$$

$$b_n = -2\omega_n^2 \; ; \; b_r = -2\omega_r^2 ,$$

$$c_n = \omega_n^4 (1 + \eta_n^2) \; ; \; c_r = \omega_r^4 \left[1 + (\eta_r' + \eta_r'')^2\right] .$$

The above is identical to Eq.(5) of Reference [2] except that $\bar{f}'(n,r)$ replaces $f'(n,r)$ and $\eta_r'+\eta_r''$ replaces η_r.

Noise Reduction Calculation

The interior pressure is obtained by setting $W_{in} = W_{diss}$ (using Eqs.(17) and (5)) solving for the mean square modal pressures $\langle p_n^2\rangle_{s,t}$ one-by-one, and adding according to Eq.(3).

The result is found to be

$$\frac{\langle p_i^2\rangle_{s,t}}{\langle p_e^2\rangle_{s,t}} = \frac{8}{c_\omega \omega}\,\frac{\bar{A}^2}{V^2}\left(\frac{mA}{4}\right)^2 \tau_{ML}\; c_o^2\; \omega^3$$

$$\cdot\sum_n \epsilon_n \sum_r \frac{j_r^{2\,rev}(\omega)\; \bar{f}'^2(n,r)}{M_r^2\; D_{nr}}\left\{\left(\frac{c_r-c_n}{4}\right) \ln_n\right.$$

$$+ \left(\frac{2c_n(b_r-b_n) -b_n(c_r-c_n)}{4\eta_n\omega_n^2}\right)\arctan_n \tag{18}$$

$$\left.+ \left(\frac{c_n-c_r}{4}\right)\ln_r + \left(\frac{2c_r(b_n-b_r) -b_r(c_n-c_r)}{4(\eta_r' + \eta_r'')\omega_r^2}\right)\arctan_r\right\} ,$$

where the exterior space average mean square pressure $<p_e^2>_{s,t}$ is (for the reverberant field) related to the mean square blocked pressure by

$$<p_e^2>_{s,t} = <p_{bl}^2>/2 \quad .$$

High Frequencies

When the acoustic modal density is greater than, say, ten or more modes in a third octave band, a high frequency model is needed, developed along the lines of [1,2, and 3]. In the case of an added trim, there are three surface areas of concern: 1) the transmitting area with trim, which will be called A_t, 2) the absorbing surface area S, and, 3) the transmitting area without trim A'. The total transmitting area is A_t+A' and the inflowing power takes the form (assuming that only the sidewall contributes)

$$W_{in} = \left\{ \frac{A_t\tau_R}{4\rho c_o} + \frac{8\bar{A}A_t}{\pi m^2}\,\frac{\rho}{c_o} \sum_{r<\Delta\omega} \left[j_r^{2\,\text{rev.}}(\omega) \right]^2 \right\} \tau_t <p_e^2>_{s,t}$$

$$+ \left\{ \frac{A'\tau_R}{4\rho c_o} + \frac{8\bar{A}A'}{\pi m^2}\,\frac{\rho}{c_o} \sum_{r<\Delta\omega} \left[j_r^{2\,\text{rev.}}(\omega) \right]^2 \right\} <p_e^2>_{s,t}$$

$$- \left\{ \frac{\bar{\eta}_r A'\tau_R}{\eta_{rad}^{ext}(4\rho c_o)} + \frac{8\bar{A}A'}{\pi m^2}\,\frac{\rho}{c_o} \sum_{r<\Delta\omega} \left[j_r^{2\,\text{rev.}}(\omega) \right]^2 \right\} <p_i^2>_{s,t} \quad , \qquad (19)$$

where $\bar{A}$ denotes the surface area of the complete cylinder. $\bar{\eta}_r$ is the sum of the average external radiation loss factor, i.e., η_{rad}^{ext}, and the average structural loss factors $\eta_r'+\eta_r''$. τ_t is the trim transmission coefficient, and τ_R is the resonance transmission coefficient for the diffuse field case,

$$\tau_R = \left(2n_r \pi^2 c_o \eta_{rad}^{ext} \eta_{rad}^{int} / \rho_o \omega \bar{n}_r \right) \cdot 4\rho\, c_o / \bar{A} \quad .$$

In this expression n_r is the modal density of the fuselage structure (modes/rad/sec). The summation $r<\Delta\omega$ in Eq.(19) implies a sum over all structural modes ω_r that are resonant below the frequency band of concern. ρ_o is the exterior air density. The radiation loss factors are

$$\eta_{rad}^{ext} = \frac{2\rho_o \omega \bar{A}}{\pi m c_o} \langle j_r^2(\omega) \rangle_r^{rev.} \quad ,$$

and

$$\eta_{rad}^{int} = \frac{2\rho \omega \bar{A}}{\pi m c_o} \langle j_r^2(\omega) \rangle_r^{rev.} \quad ,$$

where $\langle j_r^2 \rangle_r^{rev.}$ is the joint acceptance averaged over the structural modes resonant in the band.

Let τ_f = field incidence transmission coefficient for mass controlled panels as defined in [3].

$$\tau_f \equiv \frac{32}{\pi} \rho^2 \frac{\bar{A}}{m^2} \sum_{r<\Delta\omega} \left[j_r^2(\omega)^{rev} \right]^2 \quad . \tag{20}$$

Then Eq.(19) becomes

$$W_{in} = \frac{1}{4\rho c_o} \left[\tau_t (\tau_R + \tau_f) A_t + (\tau_R + \tau_f) A' \right] \langle p_e^2 \rangle_{s,t}$$
$$- \frac{A'}{4\rho c_o} \left[\frac{\bar{n}_r}{\eta_{rad}^{ext}} \tau_R + \tau_f \right] \langle p_i^2 \rangle_{s,t} \quad . \tag{21}$$

The power absorbed on the wall is again given by Eq.(5). Since at these high frequencies the response is resonant acoustic, ω_n can be considered to lie in $\Delta\omega$ and Eq.(5) reduces to

$$W_{diss} = \frac{V}{\rho c_o^2} \sum_{n \varepsilon \Delta\omega} \frac{\eta_n \omega_n^2}{\omega} \langle p_n^2 \rangle_{s,t} \quad .$$

Further, noting that for this case $\omega_n \simeq \omega$ for any n, and letting the group of acoustic modes have an average loss factor $\bar{\eta}_n$, this reduces to

$$W_{diss} = \frac{V}{\rho c_o^2} \omega \bar{\eta}_n \sum_{n \varepsilon \Delta\omega} \langle p_n^2 \rangle_{s,t} = \frac{V}{\rho c_o^2} \omega \bar{\eta}_n \langle p_i^2 \rangle_{s,t} \quad ,$$

which is Eq.(7), Section III of [2]. Finally, setting

$$\bar{\eta}_n = \frac{\bar{\alpha} c_o S}{4 \omega V} \quad ,$$

where $\bar{\alpha}$ is the band average absorption coefficient and S the absorbing surface area, the above reduces to the familiar form

$$W_{diss} = \frac{\bar{\alpha} S}{4 \rho c_o} \langle p_i^2 \rangle_{s,t} \quad . \tag{22}$$

S includes the area A covered with trim and any other absorbing surface area. Equating W_{in} to W_{diss} gives the desired high frequency result [4]:

$$\frac{\langle p_e^2 \rangle_{s,t}}{\langle p_i^2 \rangle_{s,t}} \quad \frac{\bar{\alpha} S + \left[\tau_f + \tau_R (\bar{\eta}_r / \eta_{rad}^{ext})\right] A'}{\tau_t \tau A_t + \tau A'} \quad , \tag{23}$$

where $\tau = \tau_f + \tau_R$.

This is the fundamental result with trim present. Note that if all transmitting surface is covered with trim, $A' = 0$, and

$$\frac{\langle p_e^2 \rangle_{s,t}}{\langle p_i^2 \rangle_{s,t}} = \frac{\bar{\alpha} S}{\tau_t \tau A_t} \quad .$$

On the other hand, if trim does not exist, $\tau_t = 1$, $A_t = 0$, and

$$\frac{\langle p_e^2 \rangle_{s,t}}{\langle p_i \rangle_{s,t}} = \frac{\bar{\alpha} S + \left[\tau_f + \tau_R (\bar{\eta}_r / \eta_{rad}^{ext})\right] A'}{\tau A'} \quad ,$$

which is the result in [3] without trim.

Finally, $\bar{\alpha}$ is estimated with the relation

$$\bar{\alpha} = \frac{4\omega V}{c_o S} \bar{\eta}_n \quad . \tag{24}$$

When trim is present $\bar{\eta}_n$ is calculated with results developed in Appendix A.

3.4 Calculation of the Generalized Forces for Propeller Noise Excitation

Consideration is now given to the various terms that appear in the equations representing the solutions of the sound transmission problem. In this particular section, the calculation of the generalized (or modal) forces for propeller noise excitation is discussed. Specifically, consideration here is given to the term $\Psi_G(r,H)$ as defined in Eq.(10) and that appears in Eqs.(8) and (16).

ANOPP Computer Program Output

In the present case, the fluctuating pressure field acting on the fuselage due to the rotation of a propeller is determined with the NASA Langley computer program ANOPP [5]. This particular program is one of a number of such programs to exist in the aircraft industry. It was especially developed to allow predictions of noise from propellers that have advanced blade geometries. In the present case, the concern is more with the standard type of general aviation propeller. The ANOPP program easily handles the typical general aviation aircraft propeller blade.

For purposes of the present model, the primary concern is with the form of the output data from ANOPP. Referring to Fig. 1, on the fuselage structure, there will be a finite number of grid points at which the pressure time histories will be available. At each point, the modal deflection will also be available, say $\psi^r(\bar{x}_m)$. Associated with each grid point is the area ΔA where (Fig.1) $\Delta A = \Delta^2$ with Δ being the grid spacing. Now in Eq.(10) $d\bar{x}$ is an element of area, so in discrete form (10) becomes

$$\Psi_G(r,H) = \Delta^4 \sum_m \sum_{m'} C_{p_{b1}}(\bar{x}_m|\bar{x}_{m'})\psi^r(\bar{x}_m)\psi^r(\bar{x}_{m'}) \quad ,$$

where

$$\psi^r(\bar{x}_m) = \psi^r(z_k,\theta_\ell) \quad ; \quad \psi^r(\bar{x}_{m'}) = \psi^r(z_{k'},\theta_{\ell'}) \quad ,$$

and m identifies each grid point (k,ℓ),k being the axial index and ℓ the circumferential one. In the present model, the grid is confined to the side of the fuselage where the propeller is located.

To compute $\Psi_G(r,H)$, the form of $C_{p_{b1}}(\bar{x}_m|\bar{x}_{m'})$ that will result from the use of the data output by ANOPP is first needed. At each point m, there will be a pressure time history that will repeat itself over a period $T_o = BPF^{-1}$ as shown in Figure 1. Naturally from point-to-point on the grid, this pressure signature will be different. Note that T_O is 1/B of the period T of rotation: T = 60/N, where B is the number of propeller blades.

Now $C_{p_{b1}}(\bar{x}_m|\bar{x}_{m'})$ is defined in terms of the pressure time histories for the point pair (m,m'). To calculate $C_{p_{b1}}(\bar{x}_m|\bar{x}_{m'})$ the equations appearing in Section 3.2 are considered in sequence. First

$$R_{p_{b1}}(\bar{x}_m|\bar{x}_{m'};\tau) = \lim_{T\to\infty} \frac{1}{T} \int_{-T/2}^{T/2} \mathrm{Re}[p_{b1}(\bar{x}_m,t)]\mathrm{Re}[p_{b1}(\bar{x}_{m'},t+\tau)]dt \qquad (25)$$

Since $p_{b1}(\bar{x}_m,t)$ and $p_{b1}(\bar{x}_{m'},t)$ are periodic with period T_o, the time average can be performed over one period, yielding

$$R_{p_{b1}}(\bar{x}_m|\bar{x}_{m'};\tau) = \frac{1}{T_o}\int_0^{T_o} \mathrm{Re}[p_{b1}(\bar{x}_m,t)]\mathrm{Re}[p_{b1}(\bar{x}_{m'},t+\tau)]dt \ .$$

In the present case $p_{b1}(\bar{x}_m,t)$ is real so

$$R_{p_{b1}}(\bar{x}_m|\bar{x}_{m'};\tau) = \frac{1}{T_o}\int_0^{T_o} p_{b1}(\bar{x}_m,t)p_{b1}(\bar{x}_{m'},t+\tau)dt \ . \tag{26}$$

Also since $p_{b1}(\bar{x}_m,t)$ is composed of discrete frequencies, a Fourier series representation can be used

$$p_{b1}(\bar{x}_m,t) = \frac{a_o^m}{2} + \sum_{H=1}^{\infty} a_H^m\cos\omega_H t + b_H^m\sin\omega_H t \ . \tag{27}$$

By definition $\omega_H = 2\pi f_H = H(2\pi f_1)$

where $f_1 = 1/T_1$ and $T_1 = T_o = 1/BPF$,

$$a_o^m = \frac{2}{T_1}\int_0^{T_1} p_{b1}(\bar{x}_m,t)dt \ , \tag{28}$$

$$a_H^m = \frac{2}{T_1}\int_0^{T_1} p_{b1}(\bar{x}_m,t)\cos\omega_H t \ dt \ , \tag{29}$$

$$b_H^m = \frac{2}{T_1}\int_0^{T_1} p_{b1}(\bar{x}_m,t) \sin\omega_H t \ dt \ , \tag{30}$$

Let

$$A_H^m = \sqrt{(a_H^m)^2 + (b_H^m)^2} \tag{31}$$

and

$$\phi_H^m = \tan^{-1}\frac{b_H^m}{a_H^m} \tag{32}$$

Then

$$p_{b1}(\bar{x}_m,t) = \frac{a_o^m}{2} + \sum_{H=1}^{\infty} A_H^m \cos\,(\omega_H t-\phi_H^m) \quad , \tag{33}$$

and

$$p_{b1}(\bar{x}_{m'},t+\tau) = \frac{a_o^{m'}}{2} + \sum_{H=1}^{\infty} A_H^{m'} \cos[\omega_H(t+\tau) -\phi_H^{m'}] \quad . \tag{34}$$

Substituting these into Eq.(26) (using $T_o = T_1$) gives

$$\begin{aligned}
R_{p_{b1}}(\bar{x}_m|\bar{x}_{m'};\tau) &= \frac{1}{T_1}\int_o^{T_1} \frac{a_o^m}{2}\cdot\frac{a_o^{m'}}{2}\;dt \\
&+ \frac{1}{T}\int_o^{T_1} \left(\frac{a_o^m}{2}\right) \sum_{H'=1}^{\infty} A_{H'}^{m'}\cos\,[\omega_{H'}(t+\tau)-\phi_{H'}^{m'}]dt \\
&+ \frac{1}{T_1}\int_o^{T_1} \left(\frac{a_o^{m'}}{2}\right) \sum_{H=1}^{\infty} A_H^m\cos(\omega_H t-\phi_H^m)\;dt \\
&+ \frac{1}{T_1}\int_o^{T_1} \sum_{H=1}^{\infty}\sum_{H'=1}^{\infty} A_H^m A_{H'}^{m'}\cos(\omega_H t-\phi_H^m)\;x\;\cos[\omega_{H'}(t+\tau)-\phi_{H'}^{m'}]dt.
\end{aligned} \tag{35}$$

There are four terms appearing in Eq.(35). It is easy to show that the second and third terms are identically zero. The remaining two terms give upon setting $\Delta\phi_H^{mm'} = \phi_H^m - \phi_H^{m'}$,

$$R_{p_{b1}}(\bar{x}_m|\bar{x}_{m'};\tau) = \frac{a_o^m a_o^{m'}}{4} + \sum_{H=1}^{\infty}\left(\frac{A_H^m A_H^{m'}}{2}\right)\cos\left[\omega_H\tau + \Delta\phi_H^{mm'}\right] \tag{36}$$

It can be seen that the mean-square pressure at $\bar{x}_m$ is

$$R_{pb1}(\bar{x}_m|\bar{x}_m;o) = \langle p^2_{b1}(\bar{x}_m, t)\rangle_t$$

$$= \frac{\left(a^m_o\right)^2}{4} + \sum_{H=1}^{\infty} \frac{\left(A^m_H\right)^2}{2}$$

$$= \frac{\left(a^m_o\right)^2}{4} + \sum_{H=1}^{\infty} \frac{\left(a^m_H\right)^2 + \left(b^m_H\right)^2}{2} .$$

Continuing now, with $R_{p_{b1}}(\bar{x}_m|\bar{x}_{m'};\tau)$ defined, the next step is to compute the two-sided cross spectrum using

$$\bar{C}_{p_{b1}}(\bar{x}_m|\bar{x}_{m'};\omega) = \mathrm{Re}\left[\frac{1}{2\pi}\int_{-\infty}^{\infty} R_{p_{b1}}(\bar{x}_m|\bar{x}_{m'};\tau)e^{i\omega\tau}d\tau\right] . \qquad (37)$$

From Eqs.(36) and (37), it is found that

$$\bar{C}_{p_{b1}}(\bar{x}_m|\bar{x}_{m'};\omega) = \frac{a^m_o a^{m'}_o}{4}\,\delta(\omega)$$

$$+ \sum_{H=1}^{\infty}\left(\frac{A^m_H A^{m'}_H}{4}\right)\cos\Delta\phi_H^{mm'}\left[\delta(\omega+\omega_H) + \delta(\omega-\omega_H)\right] . \qquad (38)$$

The one-sided cross spectrum is therefore

$$C_{p_{b1}}(\bar{x}_m|\bar{x}_{m'};\omega) = \frac{a^m_o a^{m'}_o}{2}\,\delta(\omega) + \sum_{H=1}^{\infty}\frac{A^m_H A^{m'}_H}{2}\cos\Delta\phi_H^{mm'}\,\delta(\omega-\omega_H) . \quad (39)$$

Finally using $C_{p_{b1}}(\bar{x}_m|\bar{x}_{m'};\omega) = C_{p_{b1}}(\bar{x}_m|\bar{x}_{m'})\delta(\omega-\omega_H)$, it follows that

$$C_{p_{b1}}(\bar{x}_m|\bar{x}_{m'}) = \frac{A^m_H A^{m'}_H}{2}\cos\Delta\phi_H^{mm'} . \qquad (40)$$

Note that each harmonic ω_H corresponds to the tone frequency in Eq.(8). To compute Eq.(8), a harmonic is first selected. For that particular harmonic, from Eqs.(10) and (40)

$$\Psi_G(r,H) = \frac{\Delta^4}{2} \sum_m A_H^m \, \psi^r(\bar{x}_m) \sum_{m'} A_H^{m'} \psi^r(\bar{x}_{m'}) \cos\Delta\phi_H^{mm'} \quad . \qquad (41)$$

One of the things to note about this result is that all of the information that can be garnered from the propeller noise signatures is used. However, a disturbing feature of Eq.(41) is that for a big grid, the total number of numerical summations required can be extremely large. Since $\Psi_G(r,H)$ must be computed for each structural mode, the computations could be very time consuming. Fortunately Eq.(41) can be reduced to a more efficient result using the trigonometric identity

$$\cos\Delta\phi_H^{mm'} = \cos\phi_H^m \cos\phi_H^{m'} + \sin\phi_H^m \sin\phi_H^{m'} \quad ,$$

to yield

$$\Psi_G(r,H) = \frac{\Delta^4}{2} \left[\left(\sum_m A_H^m \psi^r(\bar{x}_m) \cos\phi_H^m \right)^2 + \left(\sum_m A_H^m \psi^r(\bar{x}_m) \sin\phi_H^m \right)^2 \right] \cdot \qquad (42)$$

In Eq.(42), (2m + 1) summations are required as opposed to the m^2 summations needed using Eq.(41).

Geometrical Considerations and Reflecting Surface Effects

The ANOPP program computes the acoustic pressure for the case of a propeller in a free-field. Here the presence of the fuselage structure needs to be taken into account since acoustic waves will be reflected by the surface. In this model, the amplitudes of the various harmonics are increased in proportion to the incidence angle. The phases computed with the ANOPP program are not modified. Until now the amplitudes A_H^m in Eq.(42) have been considered to be the ANOPP results. However, henceforth, they shall represent the blocked pressure amplitudes. To distinguish between the blocked amplitudes and the free field amplitudes, the free field values from ANOPP will be redefined by placing a bar over A_H^m . The blocked amplitudes are calculated from the free field values using

$$A_H^m = \left\{ 10^{[0.3 - 0.000224e^{0.08\gamma}]} \right\} \bar{A}_H^m \quad . \tag{43}$$

This empirically fitted curve corresponds to that found by Magliozzi [6]. γ is the "incidence angle", that is, the angle between a line running from the propeller hub to the point $\bar{x}_m$ on the fuselage and the normal to the surface at that point. The angle is calculated using (refer to Figure 2):

$$\gamma = \cos^{-1}\left\{ \frac{(r_p\cos\phi - a\cos\theta)(\cos\theta) + (r_p\sin\phi - a\sin\theta)(\sin\theta)}{\sqrt{(r_p\cos\phi - a\cos\theta)^2 + (r_p\sin\phi - a\sin\theta)^2 + (z_p - z)^2}} \right\} \tag{44}$$

3.5 Interior Coupling Factor f'(n,r)

This term determines the spatial coupling occurring between a fuselage structural mode and a cabin acoustic mode and is defined in Section 3.1 as

$$f'(n,r) = \frac{1}{A}\int_A \phi_n(\bar{x})\psi^r(\bar{x})d\bar{x}, \tag{45}$$

where $\bar{x}$ represents a point on the transmitting structure. $\phi_n(\bar{x})$ is the eigenvector for the nth cabin mode which is obtained using a finite-difference technique as detailed in Appendix C. $\psi^r(\bar{x})$ is the structural mode shape and its calculation for the present fuselage model, a cylinder with a structurally integral floor, is considered in Appendix D.

Calculation of f'(n,r) for Cylinder with Floor

The modes of the fuselage are given by Eqs.(D.22)-(D.26) in Appendix D. For the symmetric modes of the shell, these are

$$\psi_s^r(z,\theta) = +\sin\frac{M\pi z}{L} \sum_{n=0}^{n^*} C_{Mn}^{sr}(-1)^n \cos n\theta \qquad (46)$$

and for the antisymmetric modes

$$\psi_s^r(z,\theta) = -\sin\frac{M\pi z}{L} \sum_{n=1}^{n^*} C_{Mn}^{sr}(-1)^n \sin n\theta \qquad (47)$$

C_{Mn}^{sr} are the generalized coordinates defined by Peterson [13], as tabulated for an example case in Table D.1 of Appendix D. Also as shown in Figure 1, $\theta = 0$ at the bottom centerline, $\theta = \pi$ at the top centerline. ψ_s is positive along the outward normal.

For the floor (plate), the symmetric modes are

$$\psi_p^r(z,x) = \sin\frac{M\pi z}{L} \sum_{n=0}^{n^*} C_{Mn}^{pr} \cos\frac{n\pi x}{L_p} \quad , \qquad (48)$$

and the antisymmetric modes are

$$\psi_p^r(z,x) = \sin\frac{M\pi z}{L} \sum_{n=1}^{n^*} C_{Mn}^{pr} \sin\frac{n\pi x}{L_p} \quad , \qquad (49)$$

where (Figure 1), x is measured from the center of the floor, ψ_p is positive in the upward (inward) vertical direction, and L_p is the width of the floor plate,

$$L_p = 2a \sin\theta_o \quad .$$

The acoustic mode eigenvector calculated with the finite difference technique takes on discrete values on the bounding surfaces of the cabin. Consider the boundary point j = (m,n) of Fig.C-2.

From Appendix C, Eq.(C.9), the nth acoustic mode evaluated at any point $\bar{\xi}$ in the cabin is

$$\phi_n(\bar{\xi}) = \phi_{qi}(\bar{\xi}) = \cos\frac{q\pi z}{L}\,\phi_i(j) \quad . \tag{50}$$

On the cabin bounding surfaces, i.e., $\bar{\xi} = \bar{x}$ the eigenvector takes the values

$$\phi_n(\bar{x}) = \phi_{qi}(\bar{x}) = \cos\frac{q\pi z}{L}\,\phi_i(\theta_j) \quad , \tag{51}$$

where $\phi_i(\theta_j)$ is the same as $\phi_i(j)$ when j is a boundary point. To include trim on the sidewall (with a bare cabin floor) the transmission coefficient τ_t is introduced with the result

$$\bar{f}'(n,r) = \bar{f}'(qi,r) = \frac{1}{L}\int_0^L \cos\frac{q\pi z}{L}\,\sin\frac{M\pi z}{L}dz$$
$$\times \frac{1}{L_p+2a(\pi-\theta_o)}\left[\sqrt{\tau_t^H}\int_{\theta_o}^{2\pi-\theta_o} a\psi_s^r(\theta)\phi_i(\theta)d\theta - \int_{-L_p/2}^{L_p/2}\psi_p^r(x)\phi_i(x)dx\right] . \tag{52}$$

A bar is placed over f'(n,r) to indicate inclusion of sidewall trim. Eq. (52) is an approximation and not an exact result. It should be sufficiently accurate for the present needs. It is noted that the $\phi_i(\theta)$ are the boundary values of the acoustic eigenvector, i.e., the same as the $\phi_i(\theta_j)$ in Eq.(51) and $\psi_s^r(\theta)$ and $\psi_p^r(x)$ are given by the summations in Eqs.(46)-(49). Since $\phi_i(\theta)$ is known only at discrete points $\theta = \theta_j$, $j = 1, \ldots, n_b$, the last two integrals in Eq.(52) are approximated numerically.

Let θ_{1j} and θ_{2j} define the points on the circumference of the cabin cavity half-way between boundary point (m,n) and the two adjacent boundary points. The eigenvector $\phi_i(\theta_j)$ is then assumed to apply over the range θ_{1j} to θ_{2j}. For the shell, the second integral in Eq.(52) becomes

$$\left\{ C_{Mo}^{sr} \sum_{j=1}^{n_b} \phi_i(\theta_j)(\theta_{2j}-\theta_{1j})\, a \right.$$

$$\left. + \sum_{n=1}^{n^*} (-1)^n\, C_{Mn}^{sr} \sum_{j=1}^{n_b} \phi_i(\theta_j) \cdot \frac{a}{n} \left[\sin n\theta_{2j} - \sin n\theta_{1j} \right] \right\} \quad , \qquad (53)$$

that is, if both the acoustic and structural modes are symmetric. If both modes are antisymmetric, it is found that the integral evaluates to

$$\sum_{n=1}^{n^*} (-1)^n C_{Mn}^{sr} \sum_{j=1}^{n_b} \phi_i(\theta_j) \cdot \frac{a}{n} \left[\cos n\theta_{2j} - \cos n\theta_{1j} \right] \quad . \qquad (54)$$

The integral is zero if one mode is symmetric and the other antisymmetric.

Next consider

$$\int_{-L_p/2}^{L_p/2} \psi_p^r(x)\phi_i(\theta)dx \quad .$$

For two symmetric modes, this becomes

$$C_{Mo}^{pr} \sum_{j=1}^{n_b'} \phi_i(\theta_j)(x_{2j}-x_{1j})$$

$$+ \frac{L_p}{\pi} \left\{ \sum_{n=1}^{n^*} C_{Mn}^{pr} \sum_{j=1}^{n_b'} \phi_i(\theta_j) \cdot \frac{1}{n} \left[\sin \frac{n\pi x_{2j}}{L_p} - \sin \frac{n\pi x_{1j}}{L_p} \right] \right\} \quad , \qquad (55)$$

and for two antisymmetric modes

$$\frac{L_p}{\pi} \sum_{n=1}^{n^*} C_{Mn}^{pr} \sum_{j=1}^{n_b'} \phi_i(\theta_j) \cdot \frac{1}{n} \left[\cos \frac{n\pi x_{1j}}{L_p} - \cos \frac{n\pi x_{2j}}{L_p} \right] \quad . \qquad (56)$$

The integral is zero if one mode is symmetric and the other antisymmetric. In this case n_b' is the number of boundary points at which the acoustic mode has been computed on the floor. Finally, let

$$f_{qM} = \frac{1}{L} \int_0^L \cos\frac{q\pi z}{L} \sin\frac{M\pi z}{L} \, dz \quad .$$

For the case considered (shell length L = cavity length L_c),

$$f_{qM} = \begin{cases} \frac{1}{2\pi}\left[\frac{1-\cos(M+q)\pi}{M+q} + \frac{1-\cos(M-q)\pi}{M-q}\right] & ; \; M \neq q \\ 0 \quad ; \; M = q \end{cases} \tag{57}$$

If $L \neq L_c$, f_{qM} is given by the relations in Reference [3].

3.6 Joint Acceptances for Cylinder with Structurally Integral Floor

The joint acceptance function appearing in Eqs. (16), (18), (19), etc., describes the coupling between the excitation field and the structure, and is defined by the relation

$$j_r^2(\omega) = \frac{1}{\bar{A}^2 S_{pbl}(\omega)} \iint S_{pbl}(\bar{x}|\bar{x}';\omega)\psi^r(\bar{x})\psi^r(\bar{x}')d\bar{x}d\bar{x}' , \tag{58}$$

where $\bar{A}$ is the excited structural area, $S_{pbl}(\omega)$ is the blocked pressure power spectral density, and $S_{pbl}(\bar{x}|\bar{x}';\omega)$ is the blocked pressure cross power spectral density.

It has been general practice, when representing random pressure fields with spatially decaying correlation, to use a correlation function of the form

$$C_p(\bar{x}|\bar{x}';\omega) = \frac{\mathrm{Re}\{S_p(\bar{x}|\bar{x}';\omega)\}}{S_p(\omega)} \quad . \tag{59}$$

It is assumed in the present analysis that this function is separable in the longitudinal and transverse directions, i.e.,

$$C_p(\bar{x}|\bar{x}';\omega) = C_x(\xi,\omega)C_y(\zeta,\omega) \quad ,$$

where

$$\xi = x-x' \quad ; \quad \zeta = y-y' \quad .$$

The representation for a diffuse (reverberant) excitation field is well known and is given by

$$C_x(\xi,\omega) = \frac{\sin(k\xi)}{k\xi}$$
$$C_y(\zeta,\omega) = \frac{\sin(k\zeta)}{k\zeta} \quad , \qquad .(60)$$

where k is the acoustic wavenumber.

Consider the structural mode shapes for a freely supported (ideal) cylinder:

$$\psi^r(\bar{x}) = \overset{MN}{\psi}(z,\theta) = \sin\frac{M\pi z}{L}\begin{Bmatrix}\cos N\theta \\ \sin N\theta\end{Bmatrix} \quad . \qquad (61)$$

The joint acceptances for this simple modal system have long been available [17]. Now for the case of the reverberant field, the joint acceptance functions for the cylinder must consider both sines and cosines of the circumferential wavenumber. One can write $j_r^2(\omega) = j_r^2(\omega)^{rev.} = j_{MN}^2(\omega)^{rev.}$ in the form

$$j_{MN}^{2\,rev}(\omega) = j_{MN}^{2\,rev}(\omega,\psi) + j_{MN}^{2\,rev}(\omega,\phi) = j_M^{2\,rev}(\omega)\left[j_N^{2\,rev}(\omega,\psi) + j_N^{2\,rev}(\omega,\phi)\right], \qquad (62)$$

where ψ represents the cosine and ϕ the sine of the wavenumber.

The joint acceptance for the axial component of the cylinder modes, $j_M^{2\,rev}(\omega)$, is given by [17]:

$$j_M^{2\,rev}(\omega) = I_1(M) + I_2(M) + I_3(M) \quad , \qquad (63)$$

where
$$I_1(M) = \frac{1}{2\pi MkL}\{\mathrm{Cin}(kL + M\pi) - \mathrm{Cin}|M\pi - kL|\}$$

$$I_2(M) = \frac{1}{2kL}\{\mathrm{Si}(kL + M\pi) - \mathrm{Si}(M\pi - kL)\}$$

$$I_3(M) = \frac{1-(-1)^M \cos kL}{(M\pi)^2 - (kL)^2}$$

Si and Cin are the sine and cosine integrals [18].

The joint acceptances for the circumferential modes are [17],

$$j_N^2(\omega,\psi) = \int_0^1\int_0^1 \frac{\sin 2\pi ka(y_1-y_2)}{2\pi ka(y_1-y_2)} \cos 2N\pi y_1 \cos 2N\pi y_2\, dy_1 dy_2$$

$$j_N^2(\omega,\phi) = \int_0^1\int_0^1 \frac{\sin 2\pi ka(y_1-y_2)}{2\pi ka(y_1-y_2)} \sin 2N\pi y_1 \sin 2N\pi y_2\, dy_1 dy_2 ,$$

where $y_1 = y/2\pi a$, $y_2 = y'/2\pi a$, y and y' being circumferential coordinates of the two correlated points, and k the acoustic wavenumber. It follows that

$$j_N^{2\,rev}(\omega) = j_N^{2\,rev}(\omega,\psi) + j_N^{2\,rev}(\omega,\phi)$$

$$= \int_0^1\int_0^1 \frac{\sin 2\pi ka(y_1-y_2)}{2\pi ka(y_1-y_2)} \cos 2N\pi(y_1-y_2)\, dy_1 dy_2 \quad .$$

This reduces to

$$j_N^{2\,rev}(\omega) = 2\int_0^1 \frac{\sin 2\pi ka\bar{\eta}}{2\pi ka\bar{\eta}} (1-\bar{\eta}) \cos 2\pi N\bar{\eta}\, d\bar{\eta} \quad ,$$

and

$$j_0^{2\,rev}(\omega) = \int_0^1 \frac{\sin 2\pi ka\bar{\eta}}{2\pi ka\bar{\eta}} (1-\bar{\eta})\, d\bar{\eta} \quad ,$$

where $\bar{\eta} = y_1 - y_2$. Performing the integration results in

$$j_N^{2\,\mathrm{rev}}(\omega) = \frac{1}{2\pi ka}\left\{ \mathrm{Si}\left[2\pi(N+ka)\right] - \mathrm{Si}\left[2\pi(N-ka)\right]\right\} + \frac{1}{2(N\pi)^2}\;\frac{1-\cos(2\pi ka)}{1-\left(\frac{ka}{N}\right)^2} \quad , \tag{64}$$

and

$$j_o^{2\,\mathrm{rev}}(\omega) = \left[\frac{\mathrm{Si}(2\pi ka)}{\pi ka} - \frac{1-\cos(2\pi ka)}{2\pi^2 (ka)^2}\right] . \tag{65}$$

The cylinder structural model in the present case is much more complicated and the cylinder modes are given by Eqs. (46) and (47) of Section 3.5. However, the joint acceptances for the modes of the cylinder with the structurally integral floor can almost be expressed in terms of the joint acceptances for the simple cylinder because the mode shapes given in Eqs. (46) and (47) are in a form similar to that of Eq.(61), that is, they are given in terms of sine and cosine functions. The joint acceptance for the axial component of the cylinder modes, $j_M^{2\,\mathrm{rev}}(\omega)$ is thus the same as for the simple cylinder and is given by Eq.(63), and the desired joint acceptance $j_r^{2\,\mathrm{rev}}(\omega)$ is given by

$$j_r^{2\,\mathrm{rev}}(\omega) = j_M^{2\,\mathrm{rev}}(\omega) \cdot j_N^{2\,\mathrm{rev}}(\omega) \quad , \tag{66}$$

where for symmetric modes,

$$j_N^{2\,\mathrm{rev}}(\omega) = \sum_{n=0}^{\infty} \left(C_{Mn}^{sr}\right)^2 \; j_n^2(\omega,\psi) \quad , \tag{67}$$

and for anti-symmetric modes,

$$j_N^{2\,\mathrm{rev}}(\omega) = \sum_{n=1}^{\infty} \left(C_{Mn}^{sr}\right)^2 \; j_n^2(\omega,\phi) \tag{68}$$

Note here that N is a counter and is defined only in the sense of the duo (r,M), that is, for each r, there is an M and a sequence of C_{Mn}^{sr} that are identified with index N.

It is fairly straightforward to show that

$$j_n^2(\omega,\psi) = \begin{cases} \dfrac{\mathrm{Si}(2\pi ka)}{\pi ka} - \dfrac{1-\cos(2\pi ka)}{2\pi^2(ka)^2} \ ; & n=0 \\ I_2(n) + I_3(n) - I_1(n) \ ; & n>0 \end{cases} \tag{69}$$

and

$$j_n^2(\omega,\phi) = I_1(n) + I_2(n) + I_3(n) \quad , \tag{70}$$

where

$$I_1(n) = \frac{1}{4\pi nk(2\pi a)} \left\{ \mathrm{Cin}[2\pi(n+ka)] - \mathrm{Cin}[|2\pi(n-ka)|] \right\} \tag{71}$$

$$I_2(n) = \frac{1}{4\pi ka} \left\{ \mathrm{Si}[2\pi(n+ka)] - \mathrm{Si}[2\pi(n-ka)] \right\} \tag{72}$$

$$I_3(n) = \frac{1}{4(n\pi)^2} \left\{ \frac{1-\cos 2\pi ka}{1-(ka/n)^2} \right\} \tag{73}$$

3.7 Resonance Frequencies

The frequencies ω_n and ω_r of concern pertain to cabin and structural modes respectively. The cabin resonance frequencies, ω_r are determined with Eq.(C.7) or (C.11) of Appendix C using the eigenvalues from a two-dimensional finite difference calculation as detailed in that appendix. The structural resonance frequencies, ω_r, are obtained from the analysis considered in Appendix D leading to the associated program output as shown (for an example case) in Table D-1.

3.8 Loss Factors

There are a number of different loss factors that must be considered. Referring to Eqs.(8) and (18) of Sections 3.2 and 3.3, there are the loss factors η_n , η_r, η_r', and η_r''. In Eq.(16), the loss factors $\bar{\eta}_n$ and $\bar{\eta}_r$ appear. Finally, in Eqs.(19) and (23), there are the loss factors η_{rad}^{int} and η_{rad}^{ext}.

3.8.1 Acoustic Loss Factors η_n and $\bar{\eta}_n$

Bare Fuselage (Cabin)

The acoustic loss factor η_n of a bare cabin is defined herein to be a measurement for a particular acoustic mode and $\bar{\eta}_n$ the average acoustic loss factor measured for a group of modes whose resonance frequencies lie in a narrow band $\Delta\omega$.

Calculation of η_n when sidewall trim is present

The calculation of the acoustic loss factor at any frequency ω has been discussed in Appendix A (resulting in Eq.(A.12)). That result has to be formatted properly for the case where the floor is present. Also, the absorption of the ends of the cabin has to be considered. In cases where the sidewall and the surfaces at each end of the cabin are covered with a trim, the loss factor for the interior is calculated with

$$\eta_n = \frac{\omega c_o}{\omega_n^2} \frac{\varepsilon_n}{V} \left[\xi \int_{\substack{\text{curved}\\ \text{surface}}} \phi_n^2 d\bar{x} + 2\xi_e \int_{\text{ends}} \phi_n^2 d\bar{x} \right] \quad . \tag{74}$$

Here ξ is the sidewall conductance and ξ_e is the conductance of the end surfaces. The first integral in Eq.(74) is

$$\int_{\substack{\text{curved}\\ \text{surface}}} \phi_n^2 d\bar{x} = \frac{L}{2} \varepsilon_q a \sum_{j=1}^{n_b} \phi_i^2(\theta_j) \left[\theta_{2j} - \theta_{1j}\right] \quad , \tag{75}$$

where n_b is the number of boundary points. The second integral is

$$\int_{\text{ends}} \phi_n^2 d\bar{x} = \sum_{j=1}^{n_j} \phi_i^2(j) h^2 C(j) \quad , \tag{76}$$

where n_j is the number of interior and boundary points. Therefore at low frequencies, the loss factor is found to be

$$\eta_n = \frac{\omega c_o}{\omega_n^2} \frac{\varepsilon_n}{V} \left\{ \xi \frac{L}{2} \varepsilon_q a \sum_{j=1}^{n_b} \phi_i^2(j) \left[\theta_{2j} - \theta_{1j} \right] + 2\xi_e a^2 \Phi_G(i) \right\} \quad , \tag{77}$$

where $\Phi_G(i)$ is the generalized mass for the two-dimensional mode indexed i (i = 0, 1, ..., i') of Appendix C and ε_n is the normalization constant given by Eq.(C.10) of that appendix. Also $\varepsilon_q = 2$ for $q = 0$; 1 for $q > 0$.

At high frequencies, the average loss factor is used and is

$$\bar{\eta}_n = \frac{8 c_o}{4 \omega V} \left[\xi S + 2\xi_e S_e \right] \quad , \tag{78}$$

S and S_e being the sidewall and ends' surface areas.

In cases where the average absorption coefficient $\bar{\alpha}$ is available for the various frequency bands, $\bar{\eta}_n$ can be calculated with Eq.(24). However, in general it is $\bar{\alpha}$ that is to be calculated from $\bar{\eta}_n$ and $\bar{\eta}_n$ is to be analytically derived using Eq.(74) where the conductances ξ and ξ_e are based on the trim admittance calculations made with Eq.(A.16) of Appendix A.

3.8.2 Structural Loss Factors

The structural loss factor η_r is defined as the sum of two components, one due to dissipation in the structure (in vacuo) and the other due to radiation losses, i.e.,

$$\eta_r = \eta_r^{struc} + \eta_r^{rad} \quad . \tag{79}$$

η_r^{struc} is either a measured value or an estimate based upon measurements for, say, similar structures. In the absence of any actual measured data, it is recommended that one use [19]

$$\eta_r^{\mathrm{struc}} = \frac{C}{f_r} \quad , \qquad (80)$$

where f_r is the resonance frequency and the constant C typically ranges between 2 and 4.

The acoustic loss factor η_r^{rad} is the external radiation loss factor for mode r. It is calculated using

$$\eta_r^{\mathrm{rad}} = \frac{2\rho_o \omega \bar{A}}{\pi m c_o}\, j_r^{2\,\mathrm{rev}}(\omega)_r \quad , \qquad (81).$$

where $j_r^{2\,\mathrm{rev}}(\omega)$ is given by Eq.(66) of Section 3.6.

Influence of trim on structural damping

If trim is present on the sidewall, the loss factor η_r' is given by Eq.(A.7) of Appendix A, i.e.,

$$\eta_r' = \left\{ \frac{|C_w|^2}{m^2\omega_r^4} - \frac{2C_w^I \eta_r}{m\omega_r^2} + \eta_r^2 \right\}^{\frac{1}{2}} \quad . \qquad (82)$$

C_w is a (complex) parameter dependent on the values of the coefficients of the trim transfer matrix and it is given by Eq.(A.8) of Appendix A.

Influence of internal radiation: closely coupled structural and acoustic modes

The loss factor η_r'' modifies the damping level of a structural mode when its resonance frequency lies very close to a resonance frequency of an acoustic mode. The increased damping is due to power flow from the structural mode to that particular highly receptive acoustic mode. It is given by [7]

$$\eta_r'' = \frac{\rho c_o^2 A^2 \varepsilon_n f'^2(n,r)}{\omega_n^2 M_r V} \; \frac{\eta_n}{\left[(1-\omega_r^2/\omega_n^2)^2 + \eta_n^2\right]} \quad . \qquad (83)$$

The mode r is typically a structural mode lying within a bandwidth $\Delta\omega_n = \eta_n\omega_n$ centered on ω_n.

Average radiation loss factors

The radiation loss factors η_{rad}^{ext} and η_{rad}^{int} are given by the relations in Section 3.3, namely

$$\eta_{rad}^{ext} = \frac{2\rho_o\omega\bar{A}}{\pi m c_o} <j_r^2(\omega)>_r^{rev} \quad , \tag{84}$$

$$\eta_{rad}^{int} = \frac{2\rho\omega\bar{A}}{\pi m c_o} <j_r^2(\omega)>_r^{rev} \quad . \tag{85}$$

Again $<j_r^2(\omega)>_r^{rev}$ is the joint acceptance averaged over the structural modes resonant in the band. Each $j_r^{2\,rev}(\omega)$ is calculated with Eq.(66) of Section 3.6.

3.9 Validation Studies

Comparisons of analytical model predictions with measurements taken in a model validation experiment are considered in Appendix E.

REFERENCES

1. Pope, L.D., and Wilby, J.F., "Band-Limited Power Flow into Enclosures," *J.Acoust. Soc. Am.,* **62**, 4, 906-911 (1977).

2. Pope, L.D., and Wilby, J.F., "Band-Limited Power Flow into Enclosures,II," *J.Acoust. Soc. Am.,* **67**, 3, 823-826 (1980).

3. Pope, L.D., Rennison, D.C., Willis, C.M., and Mayes, W.H., "Development and Validation of Preliminary Analytical Models for Aircraft Interior Noise Prediction," *J. Sound and Vib.,*82, 4, 541-575 (1982).

4. Pope, L.D., Wilby, E.G., Willis, C.M., and Mayes, W.H., "Aircraft Interior Noise Models: Sidewall Trim, Stiffened Structures, and Cabin Acoustics with Floor Partition,"*J.Sound and Vib.,* **89**, 3, 371-417 (1983).

5. Padula, S.L., and Block, D.J.W., "Acoustic Prediction Methods for the NASA Generalized Advanced Propeller Analysis System (GAPAS)," AIAA Paper 84-2243, July 1934.

6. Magliozzi, B., "Acoustic Pressures on a Prop-Fan Aircraft Fuselage Surface," *J. Aircraft*, **19**, 2, 104-111 (1980).

7. Pope, L.D., and Wilby, E.G., "Analytical Prediction of the Interior Noise for Cylindrical Models of Aircraft Fuselages for Prescribed Exterior Noise Fields. Phase II: Models for Sidewall Trim, Stiffened Structures, and Cabin Acoustics with Floor Partition," NASA CR-165869, 1982.

8. Goldstein, M.E., Aeroacoustics, McGraw-Hill Book Co., New York, 1976.

9. Ffowcs, Williams, J.E., and Hawkings, D.L., "Sound Generation by Turbulence and Surfaces in Arbitrary Motion," *Phil. Trans. Roy. Soc. London*, **A264** (1969).

10. Farassat, F., "Linear Acoustic Formulas for Calculation of Rotating Blade Noise," *AIAA Journal*, **19**, 9, 1122-1130 (1981).

11. Woan, C.J., and Gregorek, G.M., "The Exact Numerical Calculation of Propeller Noise," AIAA Paper 78-1122 (1978).

12. Farassat, F., and Succi, G.P., "The Prediction of Helicopter Rotor Discrete Frequency Noise," VERTICA, Vol.7, No.4, pp. 309-320, 1983.

13. Peterson, M.R., "A Study of the Effects of a Longitudinal Interior Plate on the Free Vibrations of Circular Cylindrical Shells," Ph.D. Thesis, Oklahoma State University (1973).

14. Peterson, M.R., and Boyd, D.E., "Free Vibrations of Circular Cylinders with Longitudinal, Interior Partitions," *J. Sound and Vib.*, **60**, 1, 45-62 (1978).

15. Mikulas, M.M. Jr., and McElman, J.A., "On Free Vibrations of Eccentrically Stiffened Cylindrical Shells and Flat Plates," NASA TN D-3010 (1965).

16. Leissa, A.W., "Vibration of Shells," NASA SP-288, 1973.

17. Cockburn, J.A., and Jolly, A.C., "Structural-Acoustic Response, Noise Transmission Losses and Interior Noise Levels of an Aircraft Fuselage Excited by Random Pressure Fields," AFFDL-TR-68-2, 1968.

18. Abramowitz, M., and Stegun, I.A., Hdbk of Math.Functions, U.S. Dept. of Commerce, Nat'l Bureau of Standards, Amer.Math. Series 55. Washington: Govt.Printing Office, 1964.

19. Anon., "Damping in Acoustically Excited Structures," Engineering Sciences Data Unit Item No. 73011, ESDU International Ltd. (1973).

20. Wilby, J.F., and Scharton, T.D., "Acoustic Transmission through a Fuselage Sidewall," NASA CR-132602, 1975.

21. Schultz, T.J., "Wrappings, Enclosures and Duct Linings," Chapter 15 in Noise and Vibration Control, L.L. Beranek, Editor, McGraw-Hill, New York, 1971.

APPENDIX A

SIDEWALL TRIM: TRANSMISSION AND ABSORPTION MODELS

APPENDIX A - SIDEWALL TRIM

Transmission

In Section 3, the basic power flow and dissipation expressions used to solve the sound transmission problems are presented. The relations include a transmission coefficient τ_t and a structural loss factor η_r' that appear once fuselage sidewall trim is assumed to be present. In this appendix, the analyses that lead to these terms are briefly reviewed. Most of this material can be found in greater detail in the Phase II report, Ref.[7]. As stated in [7], to incorporate the effects of sidewall trim in the transmission analysis, the interactions of the exterior pressure field, fuselage structure, insulation and lining, and interior field must be considered. To integrate the trim dynamics into the analysis, the basic expressions that describe the response, transmission, and absorption characteristics of the various components of the sidewall system must be considered. To this end, the trim is assumed to be representable by a transfer matrix:

$$\begin{Bmatrix} p_2^i \\ w_2 \end{Bmatrix} = \begin{bmatrix} a_{11} & a_{12} \\ a_{21} & a_{22} \end{bmatrix} \begin{Bmatrix} p_1^i \\ w_1 \end{Bmatrix} , \qquad (A.1)$$

where referring to Figure A-1: w_1 is the displacement of the fuselage skin at $\bar{x}$, p_1^i is the pressure on the inner surface of the skin at $\bar{x}$, w_2 is the displacement of the trim panel at $\bar{x}$, and p_2^i is the pressure on the trim inside surface at $\bar{x}$ (cavity side). Reference [7] should be consulted for more discussion of this trim model.

In addition to the trim equations there is the basic expression for the response of the sidewall. For harmonic excitation it is

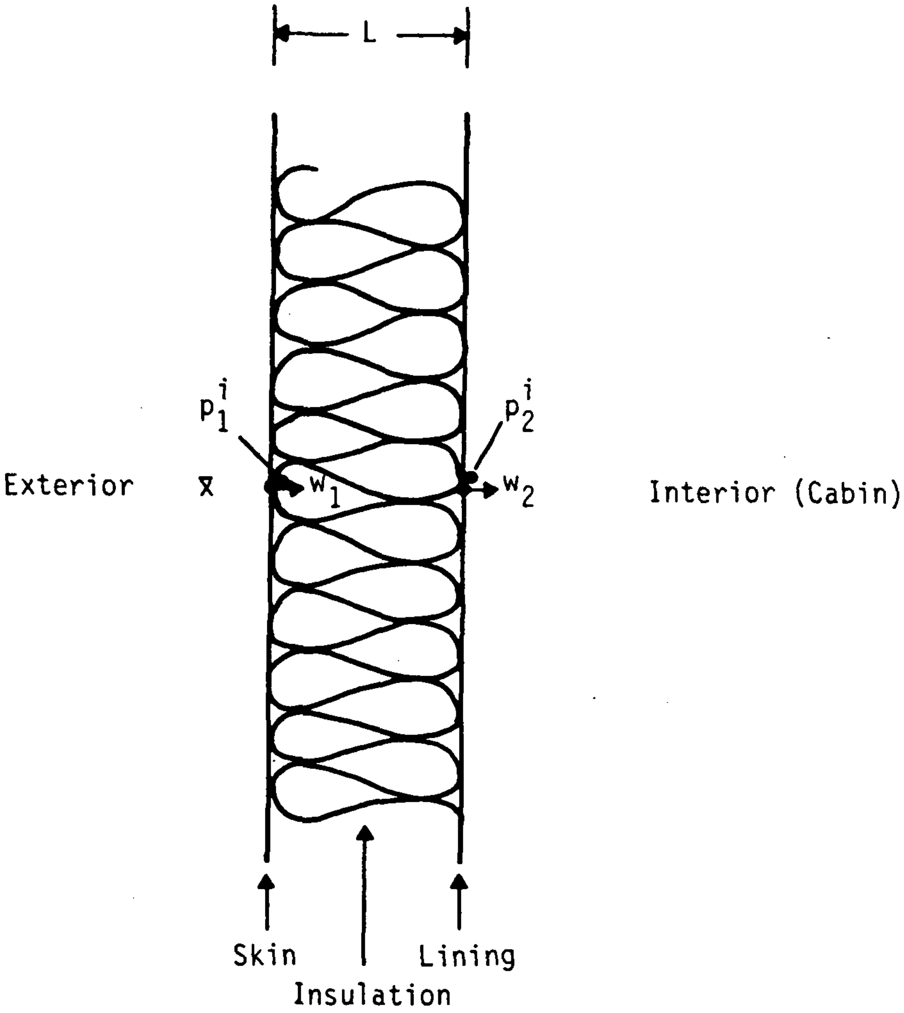

FIGURE A-1. A BASIC SIDEWALL TRIM: INSULATION AND LINING

$$w_1(\bar{x}) = \int G(\bar{x}|\bar{x}';\omega)[p^o(\bar{x}') - p_1^i(\bar{x}')]\, d\bar{x}' \quad , \qquad (A.2)$$

where $G(\bar{x}|\bar{x}';\omega)$ is the structure's Green's function, and $p^o(\bar{x}')$ is the exciting exterior pressure field. The integral is performed over the excited structural area.

Also, the interior acoustic field acting on the trim lining is

$$p_2^i(\bar{x}') = -\rho\omega^2 \int G_p(\bar{x}|\bar{x}';\omega)\, w_2(\bar{x})\, d\bar{x} \quad , \qquad (A.3)$$

where $G_p(\bar{x}|\bar{x}';\omega)$ is the Green's function for the cavity and ρ is the density in the cabin.

Finally, the exterior field is

$$\begin{aligned} p^o(\bar{x}') &= p_{b1}(\bar{x}') + \rho_o\omega^2 \int G_p^o(\bar{x}|\bar{x}';\omega) w_1(\bar{x}) d\bar{x} \\ &= p_{b1}(\bar{x}') + p_r(\bar{x}') \quad , \qquad (A.4) \end{aligned}$$

ρ_o is the exterior air density,
$G_p^o(\bar{x}|\bar{x}';\omega)$ is the exterior space Green's function,
$p_r(\bar{x}')$ is the radiated pressure field on the exterior surface,
$p_{b1}(\bar{x}')$ is the blocked pressure field on the exterior surface.

Equations (A.2), (A.3) and (A.4) and the trim transfer matrix (A.1) form a system of five equations in five unknowns: p_1^i, p_2^i, w_1, w_2, and p_r (or p^o); the blocked pressure field is assumed to be determinable once the geometry of the structure is fixed and the excitation defined. The solution of this system of equations determines the effects introduced by the presence of the trim. Note that if the trim is removed $p_1^i = p_2^i$ and $w_1 = w_2$ reducing Eqs.(A.2), (A.3), and (A.4) to the set solved in References [1] and [2].

In Reference [7] it is shown that the trim panel displacement is very nearly given by the result

$$w_2(\bar{x}) \approx C^W w_1(\bar{x}) \quad , \tag{A.5}$$

where $C^W = a_{11}^{-1}$ and a_{11} comes from the trim transfer matrix. The acoustic power radiated into the cabin is computed with the theory presented in Ref.[1] and [2], and it is shown in Ref.[7] that the inflowing power is given by Eq.(6) of Section 3.1 of this report, where C^W appears in the form of its magnitude squared, which is defined to be

$$\tau_t = |C^W|^2 = |a_{11}|^{-2} \tag{A.6}$$

Since this term multiplies a power flow expression that basically remains the same whether trim is present or not, $|C^W|^2$ is easily interpreted as a transmission coefficient for the trim.

It is also found that when trim is present, the structural loss factor η_r is augmented. Thus if η_r is defined to be that due to dissipation in the structure when trim is absent and η_r' is the total structural loss factor when trim is present, then according to the analysis in [7]

$$\eta_r'^2 = \frac{|C_w|^2}{m^2 \omega_r^4} - \frac{2C_w^I}{m} \frac{\eta_r}{\omega_r^2} + \eta_r^2 \quad , \tag{A.7}$$

where

$$C_w = C_w^R + i\, C_w^I \quad ,$$

and is obtained from the remaining three elements of the trim transfer matrix from the result

$$C_w = \frac{-a_{12}a_{22}}{1+a_{12}a_{21}} \quad . \tag{A.8}$$

Trim Transfer Matrix

The transfer matrix for a layer of insulation is the following (Appendix A of Ref.[7]):

$$\begin{Bmatrix} p_2 \\ v_2 \end{Bmatrix} = \begin{bmatrix} C & -WS \\ -\frac{S}{W} & C \end{bmatrix} \begin{Bmatrix} p_1 \\ v_1 \end{Bmatrix} \quad , \tag{A.9}$$

where $C = \cosh \gamma L$; $S = \sinh \gamma L$; $\gamma = \alpha - ik = \alpha - i2\pi/\lambda m$

γ is the propagation constant of the insulation (complex). W is the wave impedance of the insulation (refer to Fig.A.2). It is noted here that Eq.(A.9) is not in the form of Eq.(A.1). The matrix of concern, given in Eq.(A.1) relates pressures and displacements, rather than pressures and velocities. Since

$$v_i = -i\omega w_i \quad ,$$

Eq.(A.9) is more properly written as

$$\begin{Bmatrix} p_2 \\ w_2 \end{Bmatrix} = \begin{bmatrix} C & +i\omega WS \\ -\frac{iS}{\omega W} & C \end{bmatrix} \begin{Bmatrix} p_1 \\ w_1 \end{Bmatrix} \quad . \tag{A.10}$$

In the case where the trim is nothing more than a layer of insulation, the trim transfer matrix would be given by Eq.(A.10).

If there is a lining consisting of a limp mass, the transfer matrix across it is the following:

$$\begin{Bmatrix} p_2 \\ w_2 \end{Bmatrix} = \begin{bmatrix} 1 & \omega^2 m_t + i\omega^2 \eta_t m_t \\ 0 & 1 \end{bmatrix} \begin{Bmatrix} p_1 \\ w_1 \end{Bmatrix} \quad , \tag{A.11}$$

where the index 2 is the output terminal of the four-pole and 1 is the input. m_t is the mass per unit of area of the lining and η_t is some assumed loss factor that arises because of flexure of

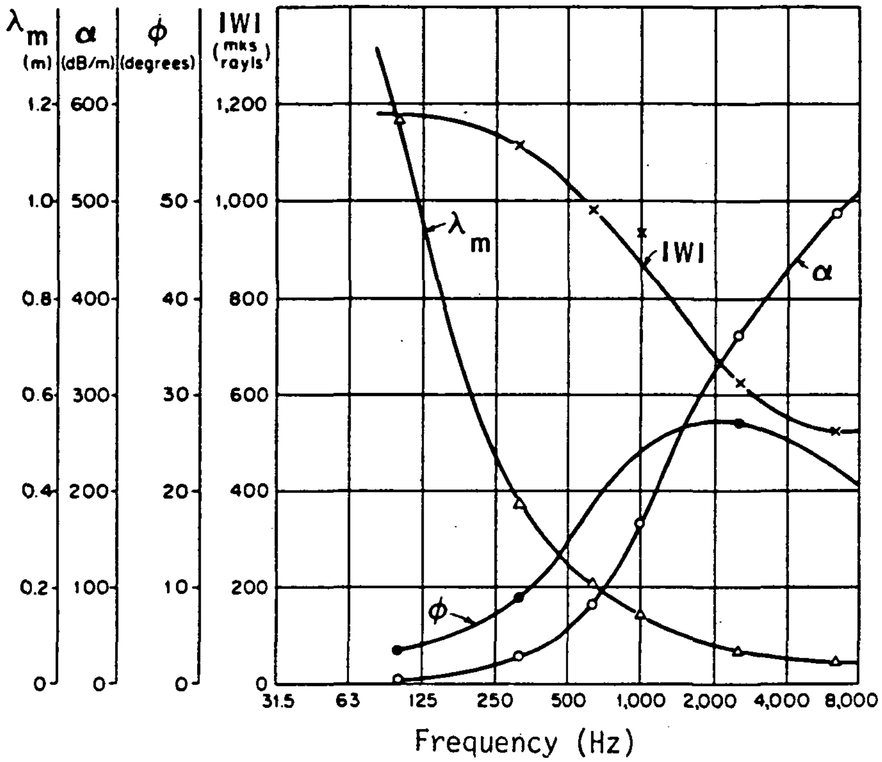

FIGURE A-2. ACOUSTICAL PROPERTIES OF OWENS-CORNING PF-105 FIBERGLAS: DENSITY 9.6 kg/m^3 (0.6 lb/ft^3), [21].

the lining (the stiffness being ignored). For a multielement trim the transfer matrix across all elements of the trim is

$$\begin{Bmatrix} p_2^i \\ w_2 \end{Bmatrix} = \begin{bmatrix} a_{11} & a_{12} \\ a_{21} & a_{22} \end{bmatrix}_n \begin{bmatrix} a_{11} & a_{12} \\ a_{21} & a_{22} \end{bmatrix}_{n-1} \cdots \begin{bmatrix} a_{11} & a_{12} \\ a_{21} & a_{22} \end{bmatrix}_2 \begin{bmatrix} a_{11} & a_{12} \\ a_{21} & a_{22} \end{bmatrix}_1 \begin{Bmatrix} p_1^i \\ w_1 \end{Bmatrix}$$

$$= \begin{bmatrix} a_{11} & a_{12} \\ a_{21} & a_{22} \end{bmatrix} \begin{Bmatrix} p_1^i \\ w_1 \end{Bmatrix} \quad , \qquad (A.12)$$

where 1 is trim element in contact with the skin and n is the finishing element in the cabin. The transfer matrix for the trim of Figure C-1 can be determined using Eqs. (A.10), (A.11), and (A.12)

$$\begin{Bmatrix} p_2^i \\ w_2 \end{Bmatrix} = \begin{bmatrix} (C - i\omega m_t \frac{S}{W} + \omega \eta_t m_t \frac{S}{W}) & (i\omega WS + \omega^2 m_t C + i\omega^2 \eta_t m_t C) \\ -\frac{iS}{\omega W} & C \end{bmatrix} \begin{Bmatrix} p_1^i \\ w_1 \end{Bmatrix} . \qquad (A.13)$$

According to the definition of the trim transmission coefficient, see Eq.(A.6), for this case

$$\tau_t = |a_{11}|^{-2} \quad ,$$

where

$$a_{11} = (C + \omega \eta_t m_t \frac{S}{W}) - i\omega m_t \frac{S}{W} \quad . \qquad (A.14)$$

Note that C, S, and W are complex.

Eq. (A.12) can be used to as high a frequency as is found (through experimental comparison) to be valid. In practical trims, the mechanical vibration transmission from fuselage skin to trim panel will become significant at high frequencies and eventually the errors involved with (A.1) may require that some alternate approach be considered to obtain the correct input data for the trim. Because of the result in Eq.(A.5) one can always take the ratio of say the measured mean square displacements (or velocities or accelerations) of the fuselage skin and the trim panel, average the results over the transmitting surface and estimate $|C^W|^2$ (and thus τ_t). Also by measuring the actual damping of the fuselage wall with trim installed, η_r' can be determined and basically all of the pertinent information required from the terms of the trim transfer matrix is obtained. This allows a fairly elementary approach to the use of any available experimental data or of any analyses that have focused on the vibration transmission (or shorting) problem.

Sound Absorption

In addition to the transmission and damping effects, the trim installation will be a sound absorbing system, that is, it will take energy from the cabin space. It is shown in [7] that this absorption capability is also describable from the terms of the trim transfer matrix. In fact, the loss factors for the cabin acoustic modes can be determined with the relation

$$\eta_n = \frac{\omega c_o}{\omega_n^2} \frac{\varepsilon_n}{V} \int_{\bar{x}} \xi(\bar{x})\phi_n^2(\bar{x})d\bar{x} \quad , \qquad (A.15)$$

where $\xi(\bar{x})$ is the conductance looking from the cabin into the sidewall treatment. For a case where ξ is independent of $\bar{x}$, we can use

$$\xi = \mathrm{Re}[\beta] \quad ,$$

where β is the admittance given by [7]

$$\beta = \rho c_o \left[\frac{-\omega^2 a_{21} Z_1 + i\omega a_{22}}{i\omega a_{11} Z_1 + a_{12}} \right] \quad . \qquad (A.16)$$

It is seen that the transfer matrix (A.1) describes the trim absorption, except for the presence of the term Z_1 which is the structural impedance. In [7], a simple model

$$Z_1 = \rho_o c_o - i\omega m \quad , \tag{A.17}$$

is recommended, and this is used in the present program.

Vibration Transmission to Trim

As stated previously, the mechanical vibration from fuselage skin to trim panel can become significant at high frequencies. According to the results found in Ref.[7] and summarized by Eqs. (A.5) and (A.6), the trim transmission coefficient τ_t is simply

$$\tau_t = |C^w|^2 = \frac{<w_2^2>}{<w_1^2>} \quad , \tag{A.18}$$

that is, it is the ratio of the mean square trim panel displacement upon the mean square skin displacement. As long as transmission through the insulation is dominant, $\tau_t = |a_{11}|^{-2}$; but once the mechanical vibration transmission is dominant, $<w_2^2>$ will be larger than that estimated with Eq.(A.6) and instead, $<w_2^2>/<w_1^2>$ must be a measurement or an analytical prediction for the mechanical vibration transmission. At high frequencies, a simple expression for this ratio can be derived using statistical energy analysis procedures. The transmission coefficient for the mechanical path is [20]:

$$\tau_t^m = \frac{m_t A_t n_t}{m A n_r} \cdot \frac{\eta_{21}}{\eta_{21} + \eta_t} \quad , \tag{A.19}$$

where m_t is the trim lining mass per unit area, A_t is the trim area and n_t the trim modal density. m, A, and n_r are the same quantities for the fuselage sidewall. η_t is the trim loss factor (in flexure) and η_{21} is a coupling loss factor for transmission from trim to skin.

For N point connections between skin (frames) and trim [20]:

$$\eta_{21} = \frac{4N}{\sqrt{3}A_t}\left(\frac{h_t c_t}{\omega}\right)\frac{(mhc_\ell)(m_t h_t c_t)}{(mhc_\ell + m_t h_t c_t)^2} \quad , \qquad (A.20)$$

where h_t and c_t are the trim lining's mass per unit area and dilatational (longitudinal) wavespeed; h and c_ℓ are the corresponding skin properties. For a line support, the coupling loss factor per unit length is [20]

$$\eta_{21} = \left(\frac{2}{3}\right)^{\frac{1}{4}} \frac{1}{A_t}\left(\frac{h_t c_t}{\omega}\right)^{\frac{1}{2}} \frac{(mh^{\frac{1}{2}}c_\ell^{\frac{1}{2}})(m_t h_t^{\frac{1}{2}} c_t^{\frac{1}{2}})}{(mh^{\frac{1}{2}}c_\ell^{\frac{1}{2}} + m_t h_t^{\frac{1}{2}} c_t^{\frac{1}{2}})^2} \quad . \qquad (A.21)$$

It is emphasized here that the finding in Ref.[7], namely Eq.(A.5), forms the theoretical basis and justification for this approach to trim transmission. Using these results, it can be stated that for any trim, the τ_t to be used in Eqs. (8), (16), (18) and (23) is given by

$$\tau_t = |a_{11}|^{-2} + \tau_t^m \quad . \qquad (A.22)$$

APPENDIX B

FUNDAMENTALS OF PROPELLER NOISE THEORY

APPENDIX B - PROPELLER NOISE

The goal here is to develop the basic equation used for propeller noise prediction in the ANOPP program. There is no attempt to discuss its mechanization, although appropriate references for further study are included. Consideration is limited to propellers with subsonic tip speeds and to the thickness and lifting noise components of the sound generation.

As stated earlier, there is always a problem determining just what level to begin a technical presentation when there are a number of different disciplines involved. In this particular case, since propeller noise is not an easy subject to understand, the authors have taken what might be considered the path of least resistance by utilizing a result by Goldstein that has been described as the fundamental equation of sound generation in the presence of solid boundaries [Eq.(3.6) of Ref.8], namely

$$
\begin{aligned}
\rho'(\bar{r},t) = {} & \frac{1}{c_o^2} \int_{-\infty}^{t^+} \int_{V_o(t_o)} T_{ij} \frac{\partial^2 G}{\partial y_i \partial y_j} \, dV_o dt_o \\
& + \frac{1}{c_o^2} \int_{-\infty}^{t^+} \int_{S_o(t_o)} -n_i (p-p_o) \frac{\partial G}{\partial y_i} \, dS_c dt_o \\
& + \frac{1}{c_o^2} \int_{-\infty}^{t^+} \int_{S_o(t_o)} n_i \rho_o V_i^s \frac{\partial G}{\partial t_o} \, dS_o dt_o
\end{aligned}
\qquad \text{(B.1)}
$$

In Eq.(B.1), $\rho'(\bar{r},t)$ is the fluctuating fluid density at the observer location $\bar{r}$ at time t. The equation applies to any region $V_o(t_o)$ which is bounded by surface $S_o(t_o)$ in arbitrary motion. $S_o(t_o)$ can be an inner bound as in the case of a propeller blade. There are three terms in (B.1). The first involves Lighthill's stress tensor T_{ij}. This term ultimately leads to sound of the quadrupole type being radiation emitted from the volume of fluid around the blade and is important only when the tip speeds are in the transonic region. The remaining two terms are the lifting and displacement noise components respectively. $p-p_o$ is the difference between the pressure on the blade and the ambient pressure, n_i is the ith component of the unit normal to the blade surface, V_i^s is the ith component of the blade surface velocity, and G is the free space Green's function.

$$G(\bar{r}_o,t_o)|\bar{r},t) = \frac{1}{4\pi R}\ \delta(t_o-t + R/c_o) \qquad \text{(B.2)}$$

Here $\bar{r}_o$ is the source location and R is the distance between source and receiver locations

$$R = |\bar{r}-\bar{r}_o| \doteq |\bar{x}-\bar{y}| \quad .$$

Note that the normal gradient is

$$\frac{\partial}{\partial n_o} \doteq n_i \frac{\partial}{\partial y_i}$$

where y_i is the ith source coordinate and a sum over the index i is implied. The normal surface velocity is

$$V_n = n_i V_i^s \doteq \hat{n}\cdot\bar{V}^s \quad ,$$

where $\hat{n}$ is the unit normal vector.

One reason for beginning with this result, is that it is developed carefully, unambiguously, and ingeniously by Goldstein [8]. A reader can easily wade through the algebra that leads to Eq.(B.1). The remainder of this appendix is concerned with the manipulation of this result to obtain the ANOPP equation, what shall be called here as the propeller noise formula.

To begin, it is noted that the relation between the fluid density fluctuation and the fluid pressure fluctuation, (neglecting heat conduction in the fluid) is simply

$$p' = c_o^2 \rho'$$

For convenience, the prime on the p is dropped on the left hand side, and on the right hand side, we replace the airfoil pressure $(p-p_O)$ by ℓ. Now p is understood to be the fluctuating pressure and it follows that Eq.(B.1) can be rewritten as

$$4\pi p(\bar{r},t) = \int_{-\infty}^{t^+} \int_{S_o(t_o)} -n_i \ell \frac{\partial}{\partial y_i} \left[\frac{\delta(t_o - t + R/c_o)}{R} \right] dS_o dt_o$$

$$+ \int_{-\infty}^{t^+} \int_{S_o(t_0)} n_i \rho_o V_i^s \frac{\partial}{\partial t_o} \left[\frac{\delta(t_o - t + R/c_o)}{R} \right] dS_o dt_o \qquad \text{(B.3)}$$

In the above R is independent of time.

Consider first the evaluation of

$$-n_i \frac{\partial}{\partial y_i} \left[\frac{\delta(t_o - t + R/c_o)}{R} \right] =$$

$$= -n_i \frac{\partial}{\partial y_i}\left(\frac{1}{R}\right)\delta(t_o - t + R/c_o) - \frac{n_i}{R}\frac{\partial}{\partial y_i}\left[\delta(t_o - t + R/c_o)\right]$$

Now

$$-n_i \frac{\partial}{\partial y_i}\left(\frac{1}{R}\right) = n_i \frac{1}{R^2}\frac{\partial R}{\partial y_i} = \frac{-n_i(x_i - y_i)}{R^3}$$

$$\doteq \frac{\hat{n}\cdot(\bar{r}-\bar{r}_o)}{R^3} = \frac{\hat{n}\cdot\hat{u}_r}{R^2}$$

where $\hat{u}_r$ is the so-called unit radiation vector

$$\hat{u}_r = \frac{\bar{r}-\bar{r}_o}{R} \quad .$$

Also

$$\frac{-n_i}{R}\frac{\partial}{\partial y_i}\delta(t_o - t + R/c_o) = \frac{-n_i}{R}\frac{\partial\delta(\tau)}{\partial\tau}\frac{\partial\tau}{\partial y_i}$$

where $\tau = t_o - t + R/c_o$

$$\frac{\partial\tau}{\partial y_i} = \frac{1}{c_o}\frac{\partial R}{\partial y_i} = \frac{-(x_i - y_i)}{c_o R} \doteq \frac{-\hat{u}_r}{c_o}$$

and

$$\frac{\partial\delta(\tau)}{\partial\tau} \doteq \frac{d\delta(\tau)}{d\tau}$$

Note that

$$\frac{\partial\delta(\tau)}{\partial t_o} = \frac{\partial\delta(\tau)}{\partial\tau}\frac{\partial\tau}{\partial t_o} = \frac{d\delta(\tau)}{d\tau} \quad .$$

This latter result follows because R is independent of t_o.

Following the general approach used in propeller noise prediction, it is now convenient to introduce a Lagrangian coordinate system (so-called $\bar{\eta}$ system [9,10]) that rides in the body and in which $S_o(t_o)$ remains fixed (see Figure B-1).

The velocity $\bar{V}$ and acceleration $\bar{a}$ of any point $\bar{\eta}$ in this coordinate system is

$$\bar{V} = \frac{\partial \bar{r}_o}{\partial t_o}(\bar{\eta},t_o)_{\bar{\eta}} = \text{fixed}$$

$$\bar{a} = \frac{\partial \bar{V}}{\partial t_o}(\bar{\eta},t_o)_{\bar{\eta}} = \text{fixed} \quad .$$

Since $S_o(t_o) = S_o$ is fixed in this system, i.e., S_o is a rigid surface; every point has velocity

$$\bar{V} = \bar{V}_o(t_o) + \bar{\omega}(t_o)\times\bar{\eta} \quad ,$$

where $\bar{V}_o$ is the velocity of the origin of the $\bar{\eta}$ system and $\bar{\omega}$ is the angular velocity of S_o(or the $\bar{\eta}$ system). Since $\bar{\eta}$ and $\bar{y}$ are Cartesian, the Jacobian of this transformation, i.e.,

$$(\bar{r}_o \text{or } \bar{y}) \rightarrow \bar{\eta}$$

is unity.

In the $\bar{\eta}$ system, the limits of integration of the surface integrals are independent of t_o and the order of integration in Eq.(B.3) can be reversed to yield

$$4\pi p(\bar{r},t) = \int_{S_o}\int_{-\infty}^{t^+} - \frac{\hat{n}\cdot\hat{u}_r\ell}{R^2}\,\delta(t_o-t + R/c_o)dt_o dS_o(\eta)$$
$$+ \frac{1}{c_o}\int_{S_o}\int_{-\infty}^{t^+}\left[\frac{\hat{n}\cdot\hat{u}_r\ell}{R} + \frac{\rho_o c_o \hat{n}\cdot\bar{V}^s}{R}\right]\frac{\partial}{\partial t_o}\,\delta(t_o-t + R/c_o)dt_o dS_o(\eta) \tag{B.4}$$

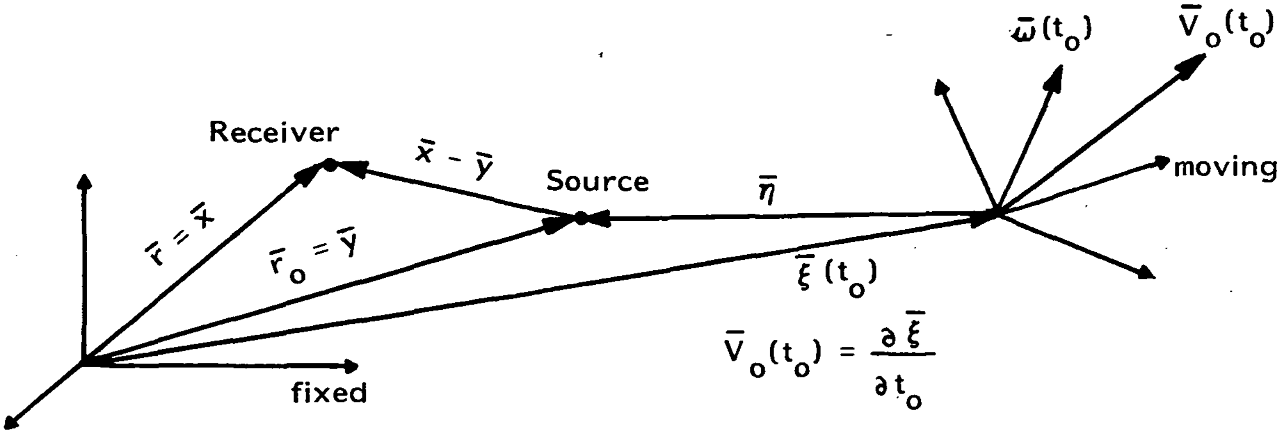

FIGURE B-1. LAGRANGIAN COORDINATE ($\bar{\eta}$) SYSTEM where now R is a function of time, i.e.,

$$\bar{y} \doteq \bar{r}_o = \bar{\xi} + \bar{\eta} = \bar{\eta} + \bar{\xi}(t_o) \doteq \bar{r}_o(t_o) \ ,$$

and

$$R = |\bar{r}-\bar{r}_o| = |\bar{x} - \bar{\eta} - \bar{\xi}(t_o)| \ .$$

To evaluate the integrals in (B.4) the following identities from generalized function theory are used [9]

$$\int_{-\infty}^{\infty} f(\tau)\delta[g(\tau)]\,d\tau = \sum_i \frac{f(\tau_e^i)}{\left|\frac{dg}{d\tau_e}(\tau_e^i)\right|} \ , \qquad \text{(B.5)}$$

where τ_e^i is the ith root of $g(\tau_e^i) = 0$.

Also

$$\int_{-\infty}^{\infty} f(\tau)\ \frac{\partial}{\partial\tau}\ \delta[g(\tau)]\,d\tau = -\int_{-\infty}^{\infty}\left[\frac{\partial}{\partial\tau}\left(\frac{\partial g}{\partial\tau}\ \frac{f(\tau)}{\left|\frac{\partial g}{\partial\tau}\right|^2}\right)\right]\delta[g(\tau)]\,d\tau \ . \qquad \text{(B.6)}$$

The first identity (B.5) is used on the first term in (B.4) to obtain

$$f(t_o) = \left.\frac{-\hat{n}\cdot\hat{u}_r\ell}{R^2}\right|_{t_o} \ ; \qquad g(t_o) \doteq t_o - t + R/c_o \ ,$$

and

$$\frac{\partial g}{\partial t_o} = 1 + \frac{1}{c_o}\frac{\partial R}{\partial t_o} = 1 + \frac{1}{c_o}\left(\frac{1}{2R}\right)(x_i-y_i)\left(\frac{-\partial y_i}{\partial t_o}\right)$$

$$= 1 - \frac{1}{c_oR}(x_i-y_i)V_i = 1 - \hat{u}_r\cdot\bar{M} = 1 - M_r \ .$$

Therefore,

$$\int_{-\infty}^{\infty} \frac{-\hat{n}\cdot\hat{u}_r\ell}{R^2}\,\delta(t_o-t + R/c_o)dt_o = \left[\frac{-\hat{n}\cdot\hat{u}_r\ell}{R^2|1-M_r|}\right]_{t_o=t_oe} , \qquad (B.7)$$

where $t_oe = t-R/c_o$.

The second identity (B.6) is used on the second term in (B.4) and then the first identity (B.5) is applied to further reduce the second term. Using

$$f(t_o) = \frac{1}{R}\left[\hat{n}\cdot\hat{u}_r\ell + \rho_o c_o \hat{n}\cdot\bar{V}^s\right] ,$$

gives

$$\int_{-\infty}^{\infty}\left[\frac{\hat{n}\cdot\hat{u}_r\ell + \rho_o c_o\;\hat{n}\cdot\bar{V}^s}{R}\right]\frac{\partial}{\partial t_o}\delta\left[t_o-t + R/c_o\right]dt_o$$

$$= -\int_{-\infty}^{\infty}\left\{\frac{\partial}{\partial t_o}\left[\frac{(1-M_r)}{|1-M_r|^2}\left(\frac{\hat{n}\cdot\hat{u}_r\ell + \rho_o c_o\hat{n}\cdot\bar{V}^s}{R}\right)\right]\right\}\delta(t_o-t + R/c_o)dt_o .$$

Since $1-M_r = |1-M_r|$ for $M_r<1$, the above

$$= -\int_{-\infty}^{\infty}\left\{\frac{\partial}{\partial t_o}\left[\frac{\hat{n}\cdot\hat{u}_r\ell + \rho_o c_o\hat{n}\cdot\bar{V}^s}{R|1-M_r|}\right]\right\}\delta(t_o-t + R/c_o)dt_o .$$

Now using (B.5), setting

$$f(t_o) = \frac{\partial}{\partial t_o}\left[\frac{\hat{n}\cdot\hat{u}_r\ell + \rho_o c_o\hat{n}\cdot\bar{V}^s}{R|1-M_r|}\right] ,$$

gives the above as

$$= -\frac{1}{|1-M_r|}\frac{\partial}{\partial t_o}\left[\frac{\hat{n}\cdot\hat{u}_r\ell + \rho_o c_o \hat{n}\cdot\bar{V}^s}{R|1-M_r|}\right]_{t_o = t-R/c_o} \quad . \qquad (B.8)$$

Substituting (B.7) and (B.8) into (B.4) gives, after changing the sign so that the normal points out of the blade,

$$4\pi p(r,t) = \frac{1}{c_o}\int_{S_o}\left\{\frac{1}{|1-M_r|}\frac{\partial}{\partial t_o}\left[\frac{\rho_o c_o V_n + \ell\hat{u}_r\cdot\hat{n}}{R|1-M_r|}\right]\right\}\underset{t-R/c_o}{dS_o(\eta)}$$

$$+\int_{S_o}\left[\frac{\ell\hat{u}_r\cdot\hat{n}}{R^2|1-M_r|}\right]_{t-R/c_o} dS_o(\eta) \quad . \qquad (B.9)$$

Eq.(B.9) can be written in an alternative form which is faster to execute on a computer and more accurate [12]. First, the acoustic pressure is separated into loading, $p_L(r,t)$ and thickness $p_T(r,t)$ contributions, such that

$$p(r,t) = p_L(r,t) + p_T(r,t)$$

Then the two components can be written in the forms

$$4\pi p_T(r,t) = \int_{S_o}\left[\frac{\rho_o V_n\,(R\dot{M}_i\hat{u}_r\cdot\hat{n} + c_o M_r - c_o M^2}{R^2(1-M_r)^3}\right]_{t-R/c_o} dS_o(\eta) \qquad (B.10)$$

and

$$4\pi p_L(r,t) = \frac{1}{c_o}\int_{S_o}\left[\frac{\dot{\ell}\hat{u}_r\cdot\hat{n}}{R(1-M_r)^2}\right]_{t-R/c_o} dS_o(\eta)$$

$$+ \int_{S_o}\left[\frac{\ell\hat{u}_r\cdot\hat{n} - \ell M_i}{R^2(1-M_r)^2}\right]_{t-R/c_o} dS_o(\eta)$$

$$+ \frac{1}{c_o}\int_{S_o}\left[\frac{\ell\hat{u}_r\cdot\hat{n}(R\dot{M}_i\hat{u}_r\cdot\hat{n} + c_oM_r - c_oM^2)}{R^2(1-M_r)^3}\right]_{t-R/c_o} dS_o(\eta) \qquad (B.11)$$

Mach number terms M_i and M^2 are given by

$$M_i = V_i/c_o \quad \text{and} \quad M^2 = V_iV_i/c_o{}^2$$

where $V_i = \frac{\partial}{\partial t_o}(\hat{u}_r\cdot\hat{n})$. Furthermore, the dot on M_i and ℓ denotes the rate of variation of these parameters with respect to time t_o.

Equations (B.10) and (B.11) have been coded at NASA Langley for use in ANOPP. The reader should consult references such as [11] and [12] for details concerning the mechanization of these results. Also, an alternative derivation of the present results is provided by Farassat in References [10] and [12].

APPENDIX C

CABIN ACOUSTIC MODES

APPENDIX C - CABIN ACOUSTIC MODES

The acoustic modal characteristics of the cabin are defined by the mode shapes $\phi_n(\xi)$, ξ being an interior point, resonance frequencies ω_n, and the mode normalization given by the constant ε_n. In the present case, consideration must be given to the determination of these quantities for the case of a cylinder with a floor partition defined by the angle θ_o as shown in Figure C-1. In the ideal complete cylinder the modal properties can be determined in closed form by an analytical solution of the wave equation, subject to the appropriate boundary conditions. This is possible because the wave equation is separable in cylindrical coordinates and the boundary conditions can be expressed in these coordinates. When the floor is present, it is no longer possible to derive the mode shapes analytically since the boundary conditions are irregular. Thus it is necessary to resort to numerical methods. There are two possibilities, either finite differences or finite elements. Since in the present case, the modal characteristics in the axial direction are known, a two-dimensional problem remains, and the finite difference technique, which is the simpler of the two, is chosen. First, the two-dimensional problem is solved. Then the axial modal information is factored in. Next the normalization of the data is defined.

Finite Difference in Two Dimensions

In the cavity (cabin), the Helmholtz equation applies. In the two-dimensional problem, using central differences, it is found that for the grid of Figure C-2, the pressure P obeys the relation

$$4\,P_{m,n}-P_{m+1,n}-P_{m-1,n}-P_{m,n+1}-P_{m,n-1} = k^2h^2P_{m,n} \quad , \qquad (C.1)$$

where h is the grid spacing, and $k = \omega/c_o$.

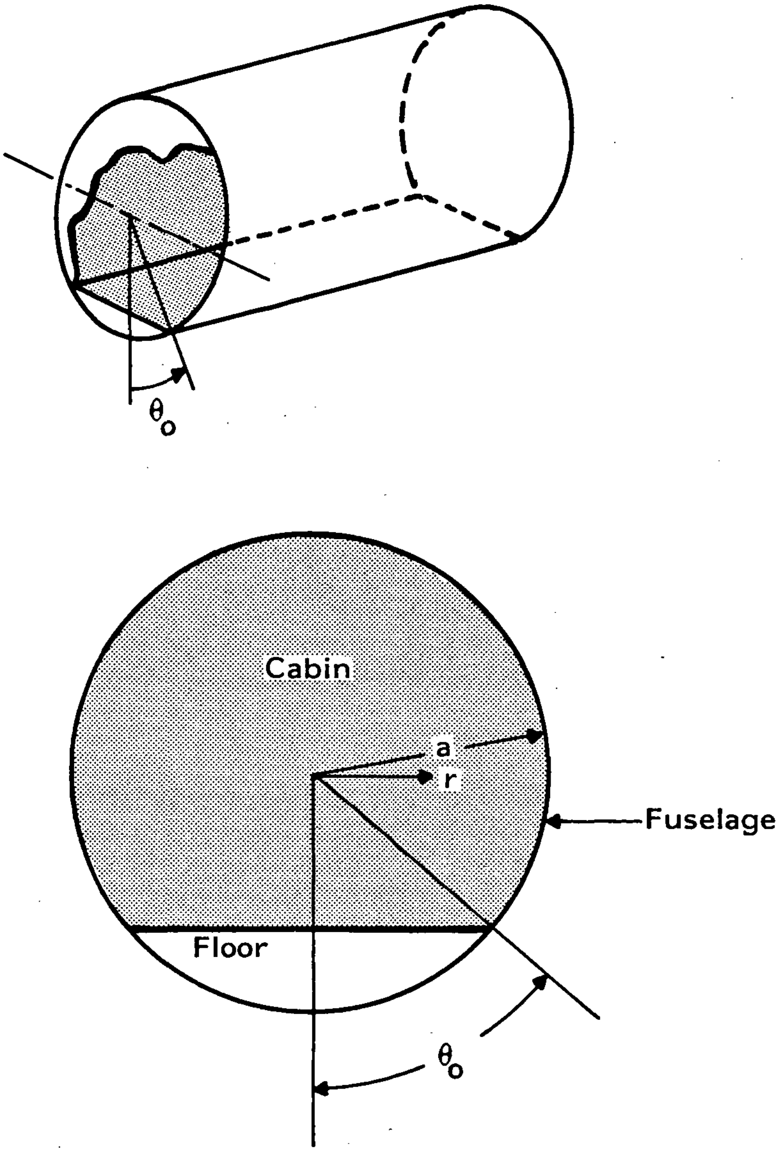

FIGURE C-1. CABIN ACOUSTIC SPACE

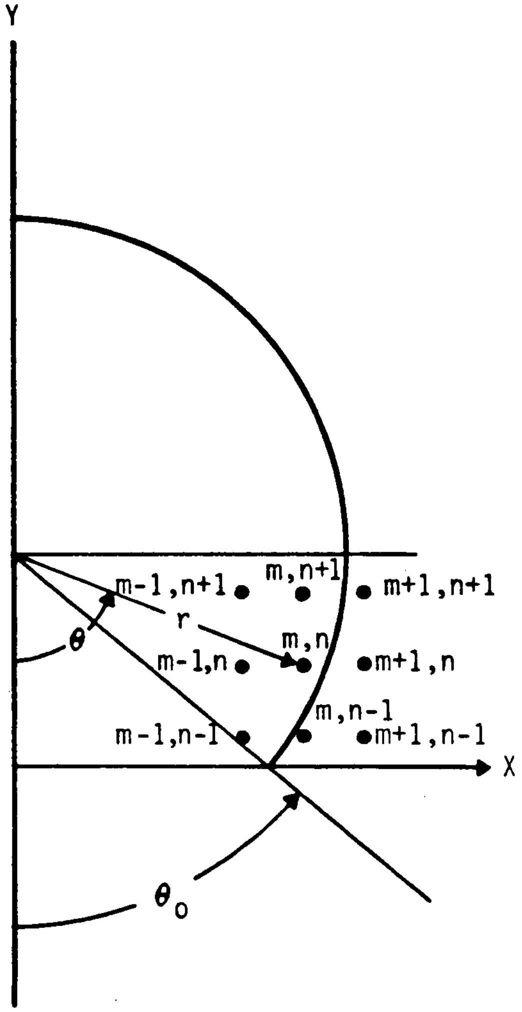

(m,n) = (NX,NY)

FIGURE C-2. FINITE DIFFERENCE GRID NOMENCLATURE

Boundary Conditions

The boundary condition is that the outward normal gradient is zero (the wall admittance β is assumed to be sufficiently small to allow this assumption). Thus, referring to Figure C-2, in the region $\theta_o<\theta<2\pi-\theta_o$:

$$(P_{m,n+1}-P_{m,n-1})\cos\theta_{mn} = (P_{m+1,n}-P_{m-1,n})\sin\theta_{mn} \quad . \qquad (C.2)$$

If $-\theta_o<\theta<\theta_o$, the boundary condition is obtained from Eq.(C.2) by simply setting $\theta_{mn} = 0$ whenever $\theta_{mn}< \theta_o$.

Solution

Let the column vector $\bar{P}_I \equiv \{P_I\}_{n_j x 1}$ be the pressure at interior and boundary points. Also let $\bar{P}_E \equiv \{P_E\}_{n_e x 1}$ be the pressure at the exterior points, adjacent to boundary points only. Using the recurrence relationship for all interior and boundary points, i.e., Eq.(C.1), gives (in matrix notation, with $\lambda = k^2h^2$)

$$R_I\bar{P}_I + R_E\bar{P}_E = \lambda\bar{P}_I \quad , \qquad (C.3)$$

where R_I has dimensions $n_j x n_j$ and R_E has dimensions $n_j x n_e$, where n_j is the number of interior and boundary points and n_e is the number of exterior points. The matrices R_I and R_E will be different for symmetric and antisymmetric modes.

The boundary conditions (Eq.(C.2)) give (n_e-2) equations. The tangential gradient is assumed zero at two boundary points close to $\theta = \pi/4$ and $3\pi/4$, giving n_e equations. When combined, these take the form

$$B_I\bar{P}_I + B_E\bar{P}_E = 0 \quad , \qquad (C.4)$$

where B_I has dimensions $n_e x n_j$ and B_e has dimensions $n_e x n_e$.

Since the matrix B_E is non-singular

$$\bar{P}_E = -B_E^{-1} B_I \bar{P}_I \quad . \tag{C.5}$$

Substituting this gives

$$[R_I - R_E B_E^{-1} B_I] \, \bar{P}_I = \lambda \bar{P}_I \, . \tag{C.6}$$

The eigenvalues and eigenvectors are calculated for symmetric and antisymmetric modes, separately. The modes are then combined, and ranked in ascending order of frequency and the first 20 modes only are used. The vector $\bar{P}_I$ corresponding to λ_i is the mode shape $\{\phi_i(j)\}$, where i is the 2-D mode counter, and j defines the position in the fuselage cross section. The nodes, n_j, represent only half the cylinder (i.e., $X \geq 0$). The values of the eigenvectors (on the boundary) will differ for symmetric and antisymmetric modes for $X < 0$. For symmetric modes, $\phi_i(j) = \phi_i(X,Y)$,

$$\phi_i(X,Y) = \phi_i(-X,Y) \quad .$$

For antisymmetric modes,

$$\phi_i(X,Y) = -\phi_i(-X,Y) \quad .$$

Each mode must therefore be identified as symmetric or antisymmetric when the boundary values of the eigenvectors are used. Apart from the boundary values of the eigenvectors, there is no need to distinguish between symmetric and antisymmetric modes in the cylinder response program. In addition, it should be noted that the first symmetric mode represents uniform translation with zero frequency.

The eigenvalues, λ_i, are used to calculate the resonance frequencies for the (three dimensional) cabin with

$$f_n = f_{qi} = \frac{c_o}{2\pi}\left[\left(\frac{q\pi}{L}\right)^2 + \frac{\lambda_i}{h^2}\right]^{\frac{1}{2}} \quad , \qquad (C.7)$$

where h is the grid spacing (=Ga), and L and a are the cylinder length and radius respectively. The frequencies output by the program are

$$f_i = \frac{c_o}{2\pi G}\sqrt{\lambda_i} \quad , \qquad (C.8)$$

i.e., the frequencies for q = 0 modes and a = 1 meter.

Normalization

The acoustic modes ϕ_n for the three dimensional cabin are

$$\phi_n(\xi)=\phi_n(X,Y,z)=\phi_{qi}(X,Y,z)=\cos\frac{q\pi z}{L}\phi_i(X,Y)=\cos\frac{q\pi z}{L}\phi_i(j) \ , \qquad (C.9)$$

where $\phi_i(X,Y)$ is the eigenvector for the two-dimensional mode ranked i (i = 0,1,2,...) as calculated with the finite difference technique; i.e., $\phi_i(X,Y)$ is a finite dimension column vector, which contains the values of ϕ_i at all coordinate positions j within and on the boundary of the cabin space. The normalization of the modes is arbitrary. The maximum value achieved at any coordinate positon has been chosen to be unity and the other values adjusted to retain the computed ratios from point-to-point. The normalization is carried into the transmission prediction with the parameter ε_n. In the case where the floor is present the integral required to determine ε_n is

$$\int_V \phi_{qi}^2(\bar{\xi})d\bar{v} = \frac{L}{2}\,\varepsilon_q \sum_{j=1}^{n_j} \phi_i^2(j)h^2C(j) \quad ,$$

where j counts over all interior locations. $C(j) = 1$ for boundary points and centerline locations, $C(j) = 2$ for interior points. Also $\varepsilon_q = 2$ for $q = 0$; 1 for $q > 0$. The generalized mass for mode i as defined in the finite difference program with unit radius is

$$\Phi_G(i) = \sum_{j=1}^{n_j} \phi_i^2(j) G^2 C(j) \quad . \qquad \text{(C.10)}$$

The volume enclosed is

$$V = a^2 L \left[\pi - \theta_o + \cos\theta_o \sin\theta_o\right] \quad .$$

Thus

$$\varepsilon_n = \varepsilon_{qi} = \frac{2\left[\pi - \theta_o + \cos\theta_o \sin\theta_o\right]}{\Phi_G(i)\varepsilon_q} \quad . \qquad \text{(C.11)}$$

Sample Results

Figure C-3 shows examples of the finite difference calculation for a case where the floor θ_o is 56.6°. The first twenty modes are shown and are ranked according to the λ_i. The resonance frequencies are for a = 1 meter. The 1 meter results given in Figure C.3 are simply the f_i in Eq.(C.8). The resonance frequencies for arbitrary radius a (in meters) is obtained from Eq.(C.7). Eq.(C.7) can also be written in the form

$$f_n = f_{qi} = \frac{c_o}{2\pi}\left[\left(\frac{q\pi}{L}\right)^2 + \left(\frac{2\pi f_i}{c_o a}\right)^2\right]^{1/2} , \qquad \text{(C.12)}$$

where f_i is the 1 meter result. Note that for $q = 0$,

$$f_{0i} = \frac{f_i}{a} \quad .$$

Table C-1 gives the computed generalized masses, $\Phi_G(i)$ for the 1 meter (unit) radius.

MODE 0. SYMMETRIC
FREQ. = 0.00

```
  1.0  1.0  1.0
  1.0  1.0  1.0  1.0  1.0
  1.0  1.0  1.0  1.0  1.0  1.0
  1.0  1.0  1.0  1.0  1.0  1.0
  1.0  1.0  1.0  1.0  1.0  1.0  1.0
  1.0  1.0  1.0  1.0  1.0  1.0  1.0
  1.0  1.0  1.0  1.0  1.0  1.0  1.0
  1.0  1.0  1.0  1.0  1.0  1.0  1.0
  1.0  1.0  1.0  1.0  1.0  1.0  1.0
  1.0  1.0  1.0  1.0  1.0  1.0  1.0
  1.0  1.0  1.0  1.0  1.0  1.0
```

MODE 1. ANTISYMMETRIC
FREQ. = 99.5

```
  -.0   .2   .3
  -.0   .2   .3   .5   .6
   .0   .2   .4   .5   .7   .8
   .0   .2   .4   .6   .7   .8
   .0   .2   .5   .6   .8   .9   .9
   .0   .2   .5   .7   .8   .9  1.0
  -.0   .3   .5   .7   .9   .9  1.0
  -.0   .3   .5   .7   .9  1.0  1.0
  -.0   .3   .5   .7   .9  1.0  1.0
  -.0   .3   .5   .7   .9  1.0  1.0
  -.0   .3   .5   .7   .9   .9
```

MODE 2. SYMMETRIC
FREQ. = 120.4

```
  1.0  1.0   .9
  1.0   .9   .9   .8   .7
   .8   .8   .8   .7   .6   .5
   .7   .6   .6   .5   .4   .3
   .4   .4   .4   .3   .3   .2   .1
   .2   .2   .1   .1   .0  -.0  -.1
  -.1  -.1  -.1  -.1  -.2  -.2  -.2
  -.3  -.3  -.3  -.4  -.4  -.4  -.4
  -.5  -.5  -.5  -.5  -.5  -.5  -.5
  -.6  -.6  -.6  -.6  -.6  -.6  -.6
  -.7  -.7  -.7  -.7  -.7  -.7
```

FIGURE C-3. ACOUSTIC MODES FOR A CASE WHERE $\theta_o = 56.6°$, q = 0, a = 1 meter

MODE 3. ANTISYMMETRIC
FREQ. = 175.9

```
-.0   .3   .6
-.0   .4   .7   .9  1.0
 .0   .4   .7   .9  1.0  1.0
 .0   .3   .6   .8   .9   .8
-.0   .2   .5   .6   .7   .6   .6
-.0   .1   .3   .3   .4   .3   .3
 .0   .0   .0   .0   .0   .0  -.0
 .0  -.1  -.2  -.3  -.3  -.3  -.3
-.0  -.2  -.4  -.5  -.6  -.6  -.6
 .0  -.2  -.5  -.7  -.8  -.8  -.8
 .0  -.3  -.5  -.7  -.8  -.9
```

MODE 4. SYMMETRIC
FREQ. = 187.9

```
 .6   .6   .4
 .6   .5   .3   .1  -.2
 .5   .4   .2  -.1  -.4  -.6
 .5   .4   .1  -.2  -.5  -.7
 .4   .3   .1  -.3  -.6  -.9 -1.0
 .5   .4   .1  -.3  -.6  -.9 -1.0
 .6   .5   .2  -.2  -.6  -.9 -1.0
 .7   .6   .3  -.1  -.5  -.7  -.8
 .8   .7   .5   .1  -.3  -.6  -.7
1.0   .9   .6   .2  -.2  -.4  -.5
1.0   .9   .6   .2  -.1  -.3
```

MODE 5. SYMMETRIC
FREQ. = 220.4

```
1.0   .9   .7
 .9   .8   .6   .3   .0
 .5   .5   .3   .1  -.1  -.3
 .1   .1  -.0  -.2  -.3  -.4
-.3  -.3  -.3  -.4  -.4  -.4  -.4
-.6  -.5  -.5  -.4  -.4  -.3  -.3
-.6  -.6  -.5  -.3  -.2  -.1  -.0
-.5  -.5  -.3  -.1   .1   .3   .3
-.3  -.3  -.1   .2   .5   .6   .6
-.2  -.1   .1   .4   .7   .8   .8
-.1  -.0   .2   .5   .8   .9
```

FIGURE C-3. CONTINUED

MODE 6. ANTISYMMETRIC

FRE. = 253.2

.0	-.5	-.9				
.0	-.5	-.9	-.9	-.8		
-.0	-.5	-.8	-.8	-.5	-.2	
-.0	-.3	-.5	-.4	-.1	.2	
-.0	-.2	-.2	-.1	.3	.6	.8
.0	-.1	-.1	.2	.5	.8	1.0
.0	-.1	-.0	.2	.5	.8	.9
.0	-.1	-.1	-.0	.3	.5	.7
.0	-.2	-.4	-.3	-.1	.1	.2
.0	-.3	-.5	-.6	-.5	-.3	-.2
-.0	-.4	-.6	-.7	-.6	-.6	

MODE 7. SYMMETRIC

FREQ. = 259.2

-.2	-.1	.1				
-.3	-.1	.2	.5	.9		
-.4	-.2	.1	.6	.9	1.0	
-.6	-.5	-.1	.4	.7	.8	
-.8	-.6	-.3	.1	.5	.6	.5
-.8	-.7	-.4	-.1	.1	.2	.2
-.6	-.5	-.4	-.3	-.1	-.1	-.1
-.1	-.1	-.2	-.2	-.3	-.3	-.3
.4	.3	.2	-.0	-.3	-.4	-.4
.8	.7	.5	.1	-.2	-.4	-.4
1.0	.9	.6	.2	-.1	-.3	

MODE 8. ANTISYMMETRIC

FREQ.= 289.7

-.0	.3	.5				
.0	.3	.5	.5	.5		
.0	.2	.3	.4	.4	.3	
.0	-.0	-.0	.0	.1	.1	
.0	-.3	-.4	-.3	-.1	.0	.1
-.0	-.5	-.7	-.6	-.3	.0	.2
-.0	-.6	-.8	-.7	-.2	.2	.4
-.0	-.6	-.8	-.6	-.0	.5	.7
-.0	-.5	-.7	-.4	.2	.7	.9
-.0	-.5	-.6	-.2	.4	.9	1.0
-.0	-.4	-.5	-.2	.4	.8	

FIGURE C-3. CONTINUED

MODE 9. SYMMETRIC
FREQ. = 300.2

```
 1.0    .8    .4
  .8    .6    .2   -.3   -.6
  .3    .2   -.1   -.5   -.7   -.6
 -.1   -.2   -.4   -.5   -.5   -.3
 -.3   -.3   -.3   -.3   -.2    .1    .4
 -.2   -.2   -.2   -.0    .2    .5    .7
  .0    .0    .1    .2    .4    .6    .7
  .2    .2    .1    .1    .2    .4    .5
  .3    .2    .1   -.1   -.1   -.1    .1
  .3    .2   -.1   -.3   -.5   -.5   -.4
  .3    .2   -.1   -.5   -.7   -.7
```

MODE 10. ANTISYMMETRIC
FREQ. = 324.6

```
 -.0   -.6   -.9
  .0   -.6   -.8   -.4    .2
  .0   -.5   -.5   -.1    .6   1.0
  .0   -.4   -.4    .1    .7   1.0
 -.0   -.3   -.3    .0    .5    .8    .7
  .0   -.3   -.4   -.2    .1    .3    .3
  .0   -.2   -.4   -.4   -.3   -.2   -.3
  .0   -.1   -.2   -.3   -.4   -.5   -.6
 -.0    .1    .2    .1   -.2   -.4   -.5
 -.0    .3    .5    .5    .2   -.0   -.2
 -.0    .4    .7    .6    .4    .2
```

MODE 11. SYMMETRIC
FREQ. = 343.7

```
 -.2   -.3   -.6
  .0   -.1   -.5   -.7   -.8
  .6    .4   -.1   -.5   -.6   -.4
 1.0    .8    .3   -.1   -.2    .1
  .9    .7    .3    .1    .1    .4    .6
  .3    .2   -.0   -.1    .1    .4    .6
 -.4   -.4   -.5   -.5   -.2    .2    .4
 -.5   -.6   -.7   -.6   -.3    .0    .2
 -.1   -.2   -.3   -.4   -.2   -.0    .1
  .6    .5    .3    .0    .0    .1    .1
 1.0    .8    .5    .2    .1    .1
```

FIGURE C-3. CONTINUED

MODE 12. ANTISYMMETRIC
FREQ. = 356.9

-.0	-.7	-1.0				
-.0	-.6	-.9	-.6	-.3		
.0	-.3	-.3	-.1	.1	.3	
.0	.1	.3	.4	.4	.3	
-.0	.4	.6	.6	.4	.0	-.3
-.0	.4	.6	.5	.1	-.4	-.7
-.0	.2	.2	.1	-.2	-.6	-.8
-.0	-.1	-.2	-.2	-.2	-.4	-.5
-.0	-.4	-.5	-.2	.1	.2	.1
-.0	-.5	-.6	-.1	.5	.8	.8
.0	-.5	-.6	-.1	.6	1.0	

MODE 13. SYMMETRIC
FREQ. = 366.1

-.7	-.5	-.1				
-.5	-.3	.2	.5	.7		
-.2	-.0	.3	.5	.5	.3	
.1	.1	.1	.2	.1	-.1	
.2	.1	-.1	-.3	-.3	-.3	-.3
.3	.1	-.3	-.5	-.5	-.2	-.0
.4	.2	-.3	-.5	-.2	.2	.5
.5	.3	-.2	-.4	-.0	.6	.9
.6	.3	-.2	-.4	-.0	.7	1.0
.5	.2	-.3	-.6	-.3	.3	.6
.5	.2	-.4	-.7	-.5	-.1	

MODE 14. SYMMETRIC
FREQ. = 381.0

1.0	.7	.0				
.7	.4	-.2	-.6	-.4		
.2	-.1	-.5	-.6	-.1	.4	
-.1	-.2	-.5	-.4	.2	.7	
.1	-.1	-.3	-.2	.3	.9	1.0
.5	.3	-.1	-.2	.1	.5	.5
.7	.4	-.0	-.4	-.4	-.2	-.2
.5	.3	-.1	-.4	-.5	-.5	-.5
.2	.1	-.1	-.2	-.2	-.2	-.3
-.2	-.2	-.1	.1	.4	.5	.3
-.4	-.3	-.1	.3	.7	.8	

FIGURE C-3. CONTINUED

MODE 15. ANTISYMMETRIC
FREQ. = 393.3

```
  .0   -.5   -.6
  .0   -.5   -.4    .3    .9
  .0   -.4   -.2    .4   1.0    .9
  .0   -.4   -.3    .2    .5    .2
 -.0   -.3   -.4   -.2   -.1   -.4   -.7
 -.0   -.2   -.2   -.2   -.2   -.5   -.6
 -.0    .0    .1    .2    .1   -.1   -.2
 -.0    .2    .3    .4    .4    .3    .3
 -.0    .1    .2    .2    .3    .3    .3
 -.0   -.1   -.2   -.2   -.2   -.1   -.0
 -.0   -.2   -.3   -.4   -.4   -.4
```

MODE 16. SYMMETRIC
FREQ. = 418.4

```
  .5    .5    .4
  .1    .2    .2   -.1   -.3
 -.5   -.4   -.1   -.1   -.4   -.4
 -.7   -.5    .0    .2   -.0   -.2
 -.4   -.1    .4    .6    .3   -.2   -.4
 -.1    .1    .6    .7    .3   -.2   -.5
 -.1   -.0    .2    .3    .1   -.3   -.4
 -.2   -.2   -.3   -.3   -.2   -.1   -.1
  .1   -.1   -.5   -.5   -.1    .3    .4
  .7    .3   -.3   -.5    .0    .6    .7
 1.0    .6   -.2   -.4    .1    .6
```

MODE 17. ANTISYMMETRIC
FREQ. = 424.0

```
  .0   -.7   -.9
  .0   -.5   -.6   -.2    .1
  .0   -.0    .1    .2    .2    .1
  .0    .4    .6    .5    .2   -.1
 -.0    .4    .5    .2   -.2   -.4   -.4
 -.0    .2    .1   -.3   -.4   -.3   -.1
 -.0   -.0   -.3   -.5   -.4    .2    .5
 -.0    .0   -.2   -.4   -.1    .6   1.0
 -.0    .3    .1   -.2   -.1    .5    .9
 -.0    .6    .5   -.1   -.5   -.2    .2
 -.0    .7    .6   -.1   -.7   -.7
```

FIGURE C-3. CONTINUED

MODE 18. SYMMETRIC
FREQ. = 434.1

```
  -.5   -.1    .8
  -.6   -.1    .8   1.0    .6
  -.8   -.4    .3    .5   -.0   -.5
  -.6   -.4   -.1   -.2   -.5   -.7
   .2    .1   -.0   -.3   -.4   -.2    .1
   .7    .6    .2   -.1   -.0    .4    .7
   .4    .3    .1   -.1    .1    .5    .7
  -.3   -.3   -.3   -.3   -.2   -.0    .2
  -.6   -.4   -.2   -.1   -.3   -.5   -.4
  -.3   -.0    .4    .4    .0   -.4   -.5
  -.0    .3    .7    .8    .3   -.0
```

MODE 19. ANTISYMMETRIC
FREQ. = 447.9

```
  -.0    .5    .5
  -.0    .4    .3   -.1   -.1
  -.0    .1   -.1   -.3   -.1    .3
   .0    .0   -.3   -.5   -.1    .5
   .0    .2   -.1   -.5   -.1    .7   1.0
   .0    .6    .3   -.4   -.4    .3    .6
   .0    .9    .6   -.4   -.7   -.2    .1
   .0    .9    .6   -.3   -.7   -.2    .1
   .0    .6    .3   -.4   -.3    .3    .6
   .0    .2   -.1   -.5   -.1    .7    .9
   .0    .1   -.3   -.6   -.1    .5
```

FIGURE C-3. CONCLUDED

TABLE C-1. EXAMPLE PROGRAM OUTPUT

Phase III Test Article

Angle subtended by floor edge with vertical, θ_o = 56.6 degrees

```
MODE     FREQUENCY            GEN.MASS

   0        0.0      SYMM  2.59631
   1       99.501    ANTI  1.03531
   2      120.374    SYMM   .72535
   3      175.889    ANTI   .68099
   4      187.927    SYMM   .72400
   5      220.381    SYMM   .49815
   6      253.162    ANTI   .54585
   7      259.176    SYMM   .50751
   8      289.674    ANTI   .51521
   9      300.184    SYMM   .36571
  10      324.597    ANTI   .42606
  11      343.723    SYMM   .45440
  12      356.949    ANTI   .46005
  13      366.051    SYMM   .36319
  14      381.030    SYMM   .39841
  15      393.310    ANTI   .28994
  16      418.374    SYMM   .34805
  17      424.029    ANTI   .37055
  18      434.105    SYMM   .40244
  19      447.887    ANTI   .45490
```

APPENDIX D

FUSELAGE STRUCTURAL MODEL: CYLINDER WITH INTEGRAL FLOOR

APPENDIX D - FUSELAGE STRUCTURAL MODEL

The fuselage modal characteristics are defined by the eigenvectors $\psi^r(\bar{x})$, resonance frequencies ω_r, and the mode normalization given by the constant M_r (the modal mass). In the present model, these quantities are computed for a ring-stringer stiffened cylinder with a floor partition that is structurally an integral part of the fuselage.

The basis of the structural model is an analysis of the free vibrations of a circular cylindrical shell with a longitudinal interior plate (Fig.D-1) by Peterson and Boyd [13,14]. A review of their analytical approach is presented in this appendix and then the generalization of their results to enable calculations for the ring-stringer stiffened shell is considered.

Displacement Functions

The displacement functions are assumed to be finite series. For the shell:

$$\begin{aligned} u_s &= \sum_{M=0}^{M^*} \sum_{n=0}^{n^*} U^s_{Mn} X_{uM}(x) \psi_{un}(\theta) \\ v_s &= \sum_{M=0}^{M^*} \sum_{n=0}^{n^*} V^s_{Mn} X_{vM}(x) \psi_{vn}(\theta) \qquad \text{(D.1)} \\ w_s &= \sum_{M=0}^{M^*} \sum_{n=0}^{n^*} W^s_{Mn} X_{wM}(x) \psi_{wn}(\theta) \; . \end{aligned}$$

The plate functions u_p, v_p, w_p are similarly expanded.

The longitudinal functions $X(x)$ are the same for the plate and the shell. These functions are expressed in terms of a single function $\phi_M(x)$, in the following manner:

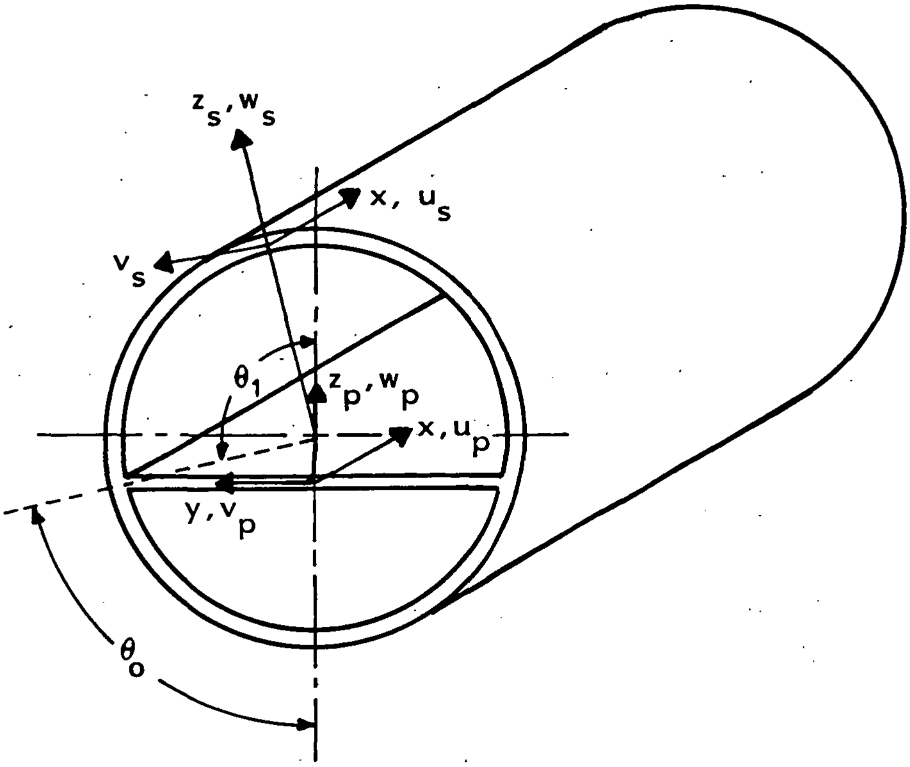

FIGURE D-1. CIRCULAR CYLINDRICAL SHELL WITH A LONGITUDINAL PARTITION

$$X_{uM} = \phi'_M(x)$$
$$X_{vM} = \phi_M(x) \qquad (D.2)$$
$$X_{wM} = \phi_M(x) \quad .$$

The functions $\phi_M(x)$ are the mode shapes of a uniform beam.

The boundary conditions used in this model are those of a supported beam, so $\phi_M(x) = \sin M\pi x/L$. Note here that the shell axial coordinate is x. In the cylindrical coordinate system used in the body of this report, the axial coordinate is z. No confusion should result from this temporary change in nomenclature.

The circumferential functions for the symmetric modes of the shell are

$$\psi_{un} = \cos n\theta$$
$$\psi_{vn} = \sin n\theta$$
$$\psi_{wn} = \cos n\theta \quad .$$

For the antisymmetric modes, (D.3)

$$\psi_{un} = \sin n\theta$$
$$\psi_{vn} = -\cos n\theta$$
$$\psi_{wn} = \sin n\theta \quad .$$

A similar set is used for the symmetric and antisymmetric modes of the plate (floor).

Constraint Equations

The floor partition can be taken to be fixed or pinned (hinged) along the line of attachment to the shell. For a rigid attachment, the shell and plate displacements obey the following relations

$$
\begin{aligned}
u_s &= u_p \\
w_s \sin\theta_1 + v_s \cos\theta_1 &= v_p \\
w_s \cos\theta_1 - v_s \sin\theta_1 &= w_p \\
\frac{v_s}{r} - \frac{1}{r}\frac{\partial w_s}{\partial\theta} + \frac{\partial w_p}{\partial y} &= 0 \quad .
\end{aligned}
\tag{D.4}
$$

In the case of a hinged connection the last equation is dropped.

Equations of Motion

Peterson [13] used Hamilton's principle to derive the equations of motion. He assumed that the cylinder was of uniform thickness t and allowed for different modulii E_x and E_θ, but no stiffeners. Following [13], the displacement functions are written in the matrix form

$$
\begin{Bmatrix} u_s \\ v_s \\ w_s \end{Bmatrix} = [N_s]\,\{q_s\} \quad , \tag{D.5}
$$

where $[N_s]$ is a matrix of size 3 x 3M*n* and $\{q\}$ is a vector of the generalized coordinates of the shell given by

$$
\{q_s\} = \begin{Bmatrix} \bar{u}_s \\ \bar{v}_s \\ \bar{w}_s \end{Bmatrix} \quad , \tag{D.6}
$$

where

$$
\{\bar{u}_s\} = \begin{Bmatrix} U_{oo} \\ U_{o1} \\ \cdot \\ \cdot \\ \cdot \\ U_{on*} \\ U_{1n*} \\ \cdot \\ \cdot \\ \cdot \\ U_{M*n*} \end{Bmatrix}, \{\bar{v}_s\} = \begin{Bmatrix} V_{oo} \\ V_{o1} \\ \cdot \\ \cdot \\ \cdot \\ V_{on*} \\ V_{1n*} \\ \cdot \\ \cdot \\ \cdot \\ V_{M*n*} \end{Bmatrix}, \{\bar{w}_s\} = \begin{Bmatrix} W_{oo} \\ W_{o1} \\ \cdot \\ \cdot \\ \cdot \\ W_{on*} \\ W_{1n*} \\ \cdot \\ \cdot \\ \cdot \\ W_{M*n*} \end{Bmatrix} \quad . \tag{D.7}
$$

The displacements of the plate are expressed in the matrix form

$$\begin{Bmatrix} u_p \\ v_p \\ w_p \end{Bmatrix} = [N_p]\ \{q_p\} \ , \qquad \text{(D.8)}$$

where the elements of $\{q_p\}$ are the generalized coordinates of the plate, arranged in the same manner as the elements of $\{q_s\}$. For either the shell or plate the strain energy can be expressed as

$$U = \frac{1}{2} \int_S \{\sigma\}^T \{\varepsilon\} dS \ , \qquad \text{(D.9)}$$

where $\{\sigma\}$ is a vector of stress resultants and $\{\varepsilon\}$ is a vector of strains and curvatures for the plate or shell.

For a linearly elastic material,

$$\{\sigma\} = [D]\ \{\varepsilon\} \ , \qquad \text{(D.10)}$$

where $[D]$ is a matrix of elastic constants. The strain-displacement relations, obtained from Love's shell theory and classical plate theory, have the form

$$\{\varepsilon\} = [G]\ \{\tilde{u}\}, \text{ where } \{\tilde{u}\} = \begin{Bmatrix} u \\ v \\ w \end{Bmatrix} \ . \qquad \text{(D.11)}$$

Substituting Eqs.(D.10) and (D.11) into (D.9), and using Eq. (D.5) or (D.8) leads to

$$U = \frac{1}{2} \int_S ([G]\ [N]\ \{q\})^T\ [D]\ [G]\ [N]\ \{q\}\ dS \ . \qquad \text{(D.12)}$$

For either the shell or the plate the kinetic energy is (in terms of the generalized coordinates)

$$U = \frac{1}{2} \{q\}^T[K]\{q\} \ , \qquad \text{(D.13)}$$

where

$$[K] = \int_S \Big[[G][N]\Big]^T [D][G][N]\ dS \ . \qquad \text{(D.14)}$$

Writing the strain energies for the shell and plate as

$$U_s = \frac{1}{2}\{q_s\}^T[K_s]\{q_s\} \text{ and } U_p = \frac{1}{2}\{q_p\}^T[K_p]\{q_p\} \quad ,$$

gives the total strain energy:

$$U = U_s + U_p = \frac{1}{2}\begin{Bmatrix} q_s \\ q_p \end{Bmatrix}^T \begin{bmatrix} K_s & 0 \\ 0 & K_p \end{bmatrix} \begin{Bmatrix} q_s \\ q_p \end{Bmatrix} = \frac{1}{2}\{q\}^T[K^*]\{q\} \quad . \qquad (D.15)$$

The kinetic energy of the plate or shell is

$$T = \frac{1}{2}\int_S \rho\{\dot{\bar{u}}\}^T\{\dot{\bar{u}}\}\, dS.$$

In terms of the generalized coordinates

$$T = \frac{1}{2}\int_S \rho\{\dot{q}\}^T[N]^T[N]\{\dot{q}\}\, dS \quad .$$

The mass matrix is defined as

$$M = \int_S \rho[N]^T\, [N]\, dS \quad ,$$

giving for either shell or plate

$$T = \frac{1}{2}\{\dot{q}\}^T[M]\{\dot{q}\} \quad .$$

The total kinetic energy for the system is the sum of the kinetic energies of the shell and plate, $T = T_s + T_p$, yielding

$$T = \frac{1}{2}\begin{Bmatrix} \dot{q}_s \\ \dot{q}_p \end{Bmatrix}^T \begin{bmatrix} M_s & 0 \\ 0 & M_p \end{bmatrix} \begin{Bmatrix} \dot{q}_s \\ \dot{q}_p \end{Bmatrix} = \frac{1}{2}\{\dot{q}\}^T[M^*]\{\dot{q}\} \ ,$$

where

$$\{q\} = \begin{Bmatrix} q_s \\ q_p \end{Bmatrix} \quad ,$$

is the combined vector of all the generalized coordinates of the shell and plate.

The components of the coordinate vector {q} are not independent because the constraint equations must be introduced to insure displacement compatibility at the interface between the plate and shell. The equations expressing this compatibility can be written in terms of the generalized coordinates in the following matrix form:

$$[C]\{q\} = \{0\} \quad . \tag{D.17}$$

Applying Hamilton's Principle and adjoining the constraint equations by introducing a vector of Lagrange multipliers in the standard way leads to the equations of motion and constraint for the system.

If $\{q\}$ is partitioned into a set of independent coordinates $\{q_1\}$ and dependent coordinates $\{q_2\}$, the constraint equations can be manipulated and the dependent coordinates and Lagrange multipliers can be algebraically eliminated. The equations of motion then take the form:

$$[M]\{\ddot{q}_1\} + [K]\{q_1\} = \{0\} \quad , \tag{D.18}$$

in which

$$[M] = [E]^T[M^*][E], \; [K] = [E]^T[K^*][E] \quad , \tag{D.19}$$

where

$$[E] = \left[\begin{array}{c} I \\ \hline [C_2]^{-1}[C_1] \end{array}\right] \quad , \tag{D.20}$$

and C_1 and C_2 are obtained from the partitioned constraint equations

$$\left[C_1 \vdots C_2\right]\begin{Bmatrix} q_1 \\ q_2 \end{Bmatrix} = \{0\} \quad . \tag{D.21}$$

The eigenvalue problem is obtained by letting $\{q_1\}$ vary harmonically with time to yield finally

$$[K]\{q_1\} = \omega^2[M]\{q_1\} \quad . \tag{D.22}$$

Now, the primary concern in this appendix is to modify the Peterson results to enable calculations for a stiffened shell. From Eqs. (D.10) and (D.11),

$$\{\sigma_s\} = [D]\{\varepsilon_s\} = [D][G]\{\tilde{u}\} \quad .$$

Peterson's results for the above (Appendix A of Ref.[13]) can be written in the modified form

$$\begin{Bmatrix} N_x \\ N_y \\ N_{xy} \\ M_x \\ M_y \\ M_{xy} \end{Bmatrix} = \begin{bmatrix} k_{xs}\frac{\partial}{\partial x} & \frac{1}{r}\nu_x k_\theta \frac{\partial}{\partial \theta} & \frac{1}{r}\nu_x k_\theta \\ \nu_\theta k_x \frac{\partial}{\partial x} & \frac{1}{r} k_{\theta R}\frac{\partial}{\partial \theta} & \frac{1}{r} k_{\theta R} \\ \frac{1}{r}G_{x\theta}t\frac{\partial}{\partial \theta} & G_{x\theta}t\frac{\partial}{\partial x} & 0 \\ 0 & \nu_x D_\theta \frac{1}{r^2}\frac{\partial}{\partial \theta}\ {}^{*} & -D_{xs}\frac{\partial^2}{\partial x^2} - \nu_x D_\theta \frac{1}{r^2}\frac{\partial^2}{\partial \theta^2} \\ 0 & D_\theta \frac{1}{r^2}\frac{\partial}{\partial \theta}\ {}^{*} & -\nu_\theta D_x \frac{\partial^2}{\partial x^2} - \frac{1}{r^2}D_{\theta R}\frac{\partial^2}{\partial \theta^2} \\ 0 & G_{x\theta}\frac{t^3}{12}\frac{1}{r}\frac{\partial}{\partial x}\ {}^{*} & -G_{x\theta}\cdot\frac{t^3}{12}\cdot\frac{2}{r}\frac{\partial^2}{\partial x \partial \theta} \end{bmatrix} \begin{Bmatrix} u_s \\ v_s \\ w_s \end{Bmatrix} \qquad (D.23)$$

In Eq.(D.23), Peterson's k_x, k_θ, D_x, and D_θ have been replaced at various points in the matrix by the augmented terms

$$\begin{aligned} k_{xs} &= k_x + \left(\frac{EA}{d}\right) \text{stringer} \\ k_{\theta R} &= k_\theta + \left(\frac{EA}{\ell}\right) \text{ring} \\ D_{xs} &= D_x + \left(\frac{EI}{d}\right) \text{stringer} \\ D_{\theta R} &= D_\theta + \left(\frac{EI}{\ell}\right) \text{ring} \quad . \end{aligned} \qquad (D.24)$$

The result may be compared to Eqs. (25)-(27) on Page 10 of Mikulas and McElman [15]. If the assumption is made that the stiffeners used by Mikulas and McElman are symmetric about the skin (i.e., $\bar{z}_s$ and $\bar{z}_r$ are zero), the equations are very similar except that the terms with the asterisks do not appear.

The strain energy term is obtained from Eq.(D.12). The result of concern is $[G]^T[D][G]$ and is given by

$$\begin{bmatrix}
\left[k_{xs}\frac{\partial^2}{\partial x^2}+\frac{1}{r^2}G_{x\theta}t\frac{\partial^2}{\partial\theta^2}\right] & \left[\frac{1}{r}\nu_x k_\theta\frac{\partial^2}{\partial x\partial\theta}+\frac{1}{r}G_{x\theta}t\frac{\partial^2}{\partial x\partial\theta}\right] & \left[\frac{1}{r^2}\nu_x k_\theta\frac{\partial}{\partial\theta}\right] \\
\left[\frac{1}{r}\nu_\theta k_x\frac{\partial^2}{\partial x\partial\theta}+\frac{1}{r}G_{x\theta}t\frac{\partial^2}{\partial x\partial\theta}\right] & \left[\begin{aligned}&\frac{1}{r^2}k_{\theta R}\frac{\partial^2}{\partial\theta^2}+G_{x\theta}t\frac{\partial^2}{\partial x^2}\\ &+D_\theta\frac{1}{r^4}\frac{\partial^2}{\partial\theta^2}+G_{x\theta}\frac{t^3}{12}\frac{1}{r^2}\frac{\partial^2}{\partial x^2}\end{aligned}\right] & \left[\begin{aligned}&\frac{1}{r^2}k_{\partial R}\frac{\partial}{\partial\theta}-\frac{1}{r^2}\nu_\theta D_x\frac{\partial^3}{\partial x^2\partial\theta}\\ &-\frac{1}{r^4}D_{\theta R}\frac{\partial^3}{\partial\theta^3}-G_{x\theta}\frac{t^3}{12}\frac{2}{r^2}\frac{\partial^3}{\partial x^2\partial\theta}\end{aligned}\right] \\
\left[\frac{1}{r}\nu_\theta k_x\frac{\partial}{\partial x}\right] & \left[\begin{aligned}&\frac{1}{r}k_{\theta R}\frac{\partial}{\partial\theta}-\nu_x D_\theta\frac{1}{r^2}\frac{\partial^3}{\partial\theta\partial x^2}\\ &-\frac{1}{r^4}D_\theta\frac{\partial^3}{\partial\theta^3}-\frac{2}{r^2}G_{x\theta}\frac{t^3}{12}\frac{\partial^2}{\partial x^2\partial\theta}\end{aligned}\right] & \left[\begin{aligned}&\frac{1}{r^2}k_{\theta R}+D_{xs}\frac{\partial^4}{\partial x^4}+\nu_x D_\theta\frac{1}{r^2}\frac{\partial^2}{\partial x^2\partial\theta^2}\\ &+\frac{1}{r^2}\nu_\theta D_x\frac{\partial^4}{\partial x^2\partial\theta^2}+\frac{1}{r^4}D_{\theta R}\frac{\partial^4}{\partial\theta^4}\\ &+\frac{4}{r^2}G_{x\theta}\frac{t^3}{12}\frac{\partial^4}{\partial x^2\partial\theta^2}\end{aligned}\right]
\end{bmatrix} \tag{D.25}$$

The equations of motion that result for the shell when the matrix (D.25) is used are almost identical to those of Mikulas [15], p. 8, or Leissa [16], p. 191. The differences are due to assumptions made in the analyses, but the important main diagonal terms are very similar in form.

To incorporate the effects of the stiffeners in the Peterson analysis, the properties of the stiffeners are "smeared-out", i.e., averaged over the shell surface as done in Ref.[15]. An equivalent skin thickness, t, is defined by

$$t = t_s + \frac{A_s}{d} + \frac{A_R}{\ell} \quad ,$$

where t_s is the actual skin thickness, A_s and A_R are the stringer and ring frame cross-sectional areas, and d and ℓ are the stringer and ring spacings. Using this thickness, the skin stiffnesses are computed from

$$k_x = k_\theta = \frac{Et}{1-\nu^2} \quad ,$$

and the skin rigidities with

$$D_x = D_\theta = \frac{Et^3}{12(1-\nu^2)}.$$

In (D.25), k_{xs} and $k_{\theta R}$ revert back to k_x and k_θ (as originally used by Peterson) but are computed with the equivalent skin thickness. D_{xs} and $D_{\theta R}$ revert back to D_x and D_θ everywhere except in the third diagonal term and are also computed using the equivalent thickness as above. In the third diagonal term D_{xs} and $D_{\theta R}$ are computed from the results in (D.24) where D_x and D_θ are computed for the actual skin thickness.

When these modifications are incorporated, it can be seen that reasonable approximations are found for the first two diagonal terms and for the off-diagonal terms but the skin stiffnesses will be somewhat higher than they would have been had k_{xs} and $k_{\theta R}$ been used (i.e., the results in (D.24)).

The Mode Shapes (Eigenvectors)

The eigenvectors for the fuselage model are the displacements u, v, and w for each eigenvalue, ω_r. The w component is the desired mode shape $\psi^r(\bar{x})$. This mode shape encompasses both the plate and shell normal displacements. The maximum normal displacement computed on either plate or shell is assigned the value of 1.0, and all other values of u, v, and w at other positions are divided by that maximum value for normalization purposes.

The mode shapes for the symmetric modes of the shell are

$$\psi_s^r(z,\theta) = \sin\frac{M\pi z}{L}\sum_{n=0}^{n^*} C_{Mn}^{sr}(-1)^n\cos n\theta\ , \qquad (D.26)$$

and for antisymmetric modes

$$\psi_s^r(z,\theta) = -\sin\frac{M\pi z}{L}\sum_{n=1}^{n^*} C_{Mn}^{sr}(-1)^n\sin n\theta\ . \qquad (D.27)$$

In these two equations, z is again the axial coordinate and θ is measured from the bottom of the cylinder. The C_{Mn}^{sr} are the generalized coordinates for the shell (the same as the W_{Mn} of Eq.(D.7)).

The symmetric modes of the floor are

$$\psi_p^r(z,x) = \sin\frac{M\pi z}{L}\sum_{n=0}^{n^*} C_{Mn}^{pr}\cos\frac{n\pi x}{L_p}\ , \qquad (D.28)$$

and the antisymmetric modes are

$$\psi_p^r(z,x) = \sin\frac{M\pi z}{L}\sum_{n=0}^{n^*} C_{Mn}^{pr}\sin\frac{n\pi x}{L_p}\ . \qquad (D.29)$$

Again, z is the axial coordinate measured from the forward end of the cylinder and x is the distance measured horizontally in the floor plane from the centerline of the fuselage to the position of concern on the floor. L_p is the width of the floor and is given by

$$L_p = 2a\sin\theta_0\ ,$$

where θ_0 is the floor angle as shown in Fig. 1. The C_{Mn}^{pr} are the generalized coordinates for the floor plate. Note that $\psi^r(\bar{x})$ is the combined set for cylinder and floor, that is,

$$\psi^r(\bar{x}) = \left\{\psi_s^r(z,\theta),\ \ \psi_p^r(z,x)\right\}\ . \qquad (D.30)$$

Generalized Mass

The generalized mass must include all energy in both the cylinder and floor and therefore is defined by

$$
\begin{aligned}
M_r = {} & \frac{L}{2}\int_{\theta=0}^{2\pi} (u_s^{r^2} + v_s^{r^2} + w_s^{r^2})\, m_s a d\theta \\
& + \frac{L}{2}\int_{0}^{Lp} (u_p^{r^2} + v_p^{r^2} + w_p^{r^2})\, m_p dx \quad ,
\end{aligned}
\tag{D.31}
$$

where m_s and m_p are the masses per unit of area of shell and plate respectively, a is the cylinder radius, and L is the cylinder length. Note that there are two components of the modal mass, one for the shell and one for the plate. If a particular mode r is, say, predominately a floor mode, M_r will be dominated by the second term and the shell contribution will then be small. For such a mode, the floor can be seen to restrain the motion induced by fuselage sidewall excitation.

Sample Output

Modes are ranked according to the occurrence of their resonance frequencies and the values of the generalized coordinates C_{Mn}^{sr} and C_{Mn}^{pr} for each mode are output. For each value of r, there is a single value of M that defines the axial mode shape, and a sequence of n's that defines the circumferential mode shape. Table D-1 gives the results for the first 32 modes of the 1.83m (72 in.) long cylinder used in the present validation study. The values of n given in the table are those that contribute most to the determination of the mode shape. Ohly 5 terms are retained for the shell and 3 for the floor. Fig.D-2 shows an example of a typical mode shape, in particular, for the first mode of Table D-1. It is apparent from the figure and also from the computed generized mass, that the mode shown is basically a floor mode.

TABLE D-1. EXAMPLE PROGRAM OUTPUT

Phase III Test Article: 1.803m (71 in.) long cylinder,
stiffened 0.0008m (0.032in) skin, 0.508m (20 in.) radius with floor at 56.6°

```
MODE   FREQ   MODE       SHELL            PLATE          GENERALIZED MASS (KG)
 NU   (HZ)    TYPE   M  N   CMN      M  N   CMN      TOTAL    SHELL W  PLATE W

   1  188.52  SYMM   1  2 -.06640   1  0  .41496   1.13889   .02830  1.10253
                     1  3 -.03362   1  2  .33940
                     1  4  .02042   1  1  .23432
                     1  1  .01776
                     1  5 -.00589

   2  208.24  SYMM   1  2 -.07694   1  1 1.42371   1.12644   .05670  1.05950
                     1  4  .06646   1  2 -.34033
                     1  5 -.03793   1  0 -.30912
                     1  3 -.02065
                     1  1 -.01360

   3  217.88  SYMM   2  4  .01270   2  0  .44544   1.06241   .00143  1.06071
                     2  2 -.01001   2  2  .41198
                     2  5 -.00550   2  1  .14239
                     2  1  .00391
                     2  3 -.00293

   4  231.01  SYMM   2  4  .04328   2  1 1.08434   1.05432   .01444  1.03897
                     2  5 -.03088   2  3  .20954
                     2  2 -.01367   2  2 -.13739
                     2  8 -.00803
                     2  7  .00740

   5  293.25  SYMM   3  4  .00824   3  0  .46520   1.05532   .00050  1.05476
                     3  5 -.00455   3  2  .43756
                     3  2 -.00386   3  1  .10293
                     3  1  .00195
                     3  7  .00119

   6  301.93  SYMM   1  2  .60434   1  2  .34208   3.35573  2.32876   .47468
                     1  3  .39210   1  1  .24271
                     1  5 -.02343   1  3  .11650
                     1  4  .01026
                     1  6  .00956

   7  303.67  SYMM   3  4  .03058   3  1 1.00245   1.04019   .00869  1.03105
                     3  5 -.02783   3  3  .19801
                     3  8 -.00764   3  2 -.08872
                     3  2 -.00758
                     3  7  .00698

   8  318.73  ANTI   1  2 -.69794   1  1 -.71809   5.33569  2.87324  1.56559
                     1  3  .33122   1  2 -.37744
                     1  1 -.17597   1  3 -.13196
                     1  4 -.10995
                     1  5  .03684
```

```
STIFFENED .032 IN CYLINDER, 20 IN RADIUS, WITH FLOOR AT 56.6 DEGREES

MODE  FREQ    MODE      SHELL             PLATE            GENERALIZED MASS (KG)
 NO   (HZ)    TYPE   M  N  CMN         M  N  CMN         TOTAL     SHELL W   PLATE W

  9  346.71   ANTI   1  3  .65759      1  2 -.37430     3.07613  2.38329    .30019
                     1  2  .29630      1  1 -.10529
                     1  1  .08228      1  3 -.02409
                     1  4  .06592
                     1  5 -.02470

 10  434.31   SYMM   4  4  .00568      4  0  .47682     1.05268   .00025   1.05241
                     4  5 -.00383      4  2  .45133
                     4  2 -.00218      4  1  .08093
                     4  1  .00130
                     4  7  .00106

 11  441.78   SYMM   4  5 -.02558      4  1  .96440     1.03311   .00632   1.02654
                     4  4  .02362      4  3  .19308
                     4  8 -.00753      4  2 -.06599
                     4  7  .00695
                     4  2 -.00602

 12  470.53   ANTI   2  3  .42411      2  2 -.48203     2.27504   .82788   1.34321
                     2  2 -.05284      2  1 -.46964
                     2  4 -.03870      2  3 -.24148
                     2  5 -.01810
                     2  6  .01552

 13  502.23   SYMM   1  1 -.76763      1  2  .66675     6.31376  2.76903    .76399
                     1  4 -.12362      1  0 -.17384
                     1  3 -.11395      1  4  .05223
                     1  6  .01293
                     1  0  .01078

 14  528.78   ANTI   1  4 -.66794      1  1 1.12932     3.71841  2.70485    .23627
                     1  1  .31690      1  2-1.02632
                     1  2 -.22781      1  3  .92727
                     1  5  .05974
                     1  7 -.02769

 15  555.05   SYMM   1  4  .61552      1  3 -.26052     3.02626  2.55327    .18097
                     1  3  .37347      1  2 -.09653
                     1  2 -.18507      1  1 -.08745
                     1  1 -.09309
                     1  5  .07360

 16  558.43   ANTI   2  3  .30944      2  1 1.00231     1.65729   .48102   1.10579
                     2  2  .10406      2  3  .96170
                     2  1  .02332      2  2 -.46528
                     2  6  .01193
                     2  7 -.00791
```

```
STIFFENED .032 IN CYLINDER, 20 IN RADIUS, WITH FLOOR AT 56.6 DEGREES

MODE  FREQ    MODE      SHELL              PLATE          GENERALIZED MASS (KG)
 NO   (HZ)    TYPE    M  N  CMN         M  N  CMN       TOTAL     SHELL W  PLATE W

 17  560.65   ANTI    1  1 -.25827      1  3  .55091    2.00966    .54454  1.11528
                      1  4  .19682      1  1  .53220
                      1  3  .11259      1  2  .14949
                      1  2 -.05185
                      1  5  .02207

 18  572.86   ANTI    3  3 -.08551      3  1  .55890    1.22949    .04255  1.18227
                      3  4  .03125      3  3  .46354
                      3  2  .02289      3  2  .21649
                      3  5  .01994
                      3  6 -.01569

 19  591.88   SYMM    2  3  .42559      2  2  .06831    1.73996   1.52659   .00197
                      2  2  .28611      2  3 -.05649
                      2  4  .27539      2  0 -.02208
                      2  5  .03191
                      2  6 -.02568

 20  607.50   ANTI    2  4  .44272      2  2  .84374    2.88669   1.78872   .88336
                      2  3  .32362      2  4  .25752
                      2  2  .29967      2  3 -.05258
                      2  5  .06404
                      2  6 -.05875

 21  626.01   ANTI    3  3 -.29317      3  2 1.58856    1.95333    .66669  1.23632
                      3  4  .20494      3  3 -.54749
                      3  6 -.09539      3  4  .44915
                      3  5  .08096
                      3  2  .04894

 22  632.02   ANTI    1  1  .22426      1  2  .64039    1.99704    .51331  1.07277
                      1  2 -.13579      1  4  .23344
                      1  3  .12769      1  3  .20029
                      1  5  .12610
                      1  4  .09665

 23  636.15   SYMM    5  4  .00462      5  0  .48042    1.05173    .00018  1.05154
                      5  5 -.00363      5  2  .45601
                      5  2 -.00161      5  1  .07378
                      5  1  .00102
                      5  7  .00100

 24  641.20   SYMM    5  5 -.02553      5  1  .95366    1.03218    .00591  1.02608
                      5  4  .02158      5  3  .19080
                      5  8 -.00763      5  2 -.05895
                      5  7  .00715
                      5  2 -.00591
```

```
STIFFENED .032 IN CYLINDER, 20 IN RADIUS, WITH FLOOR AT 56.6 DEGREES

MODE  FREQ    MODE      SHELL             PLATE          GENERALIZED MASS (KG)
 NO   (HZ)    TYPE    M  N  CMN        M  N  CMN       TOTAL     SHELL W   PLATE W

 25  648.70   SYMM    2  4  .54137     2  3 -.31842   3.12167   2.22892    .58061
                      2  2 -.45147     2  2 -.31722
                      2  5  .01850     2  0  .11216
                      2  1  .01384
                      2  6 -.00425

 26  663.30   ANTI    4  3 -.03615     4  1  .60174   1.17010    .00997   1.15917
                      4  4  .01914     4  3  .53040
                      4  5  .01472     4  2  .13228
                      4  6 -.01272
                      4  2  .01226

 27  716.23   ANTI    4  4  .11594     4  2 1.12205   1.33482    .16827   1.15854
                      4  3 -.11451     4  4  .34731
                      4  6 -.07550     4  3 -.19925
                      4  5  .05392
                      4  7  .03384

 28  717.33   ANTI    2  2 -.42010     2  2  .55423   2.32071   1.11855    .98835
                      2  3  .16269     2  4  .29992
                      2  4 -.15887     2  3  .25016
                      2  5  .11998
                      2  6 -.07240

 29  738.44   ANTI    1  4 -.59228     1  2  .81512   3.63204   1.85287    .93833
                      1  3  .14987     1  4  .50058
                      1  1 -.12843     1  3 -.13113
                      1  6 -.09905
                      1  5 -.07457

 30  761.91   SYMM    3  4 -.63950     3  3  .31731   2.90922   2.41279    .31644
                      3  3 -.35980     3  2  .15446
                      3  5 -.00670     3  0 -.05975
                      3  2  .00615
                      3  1 -.00485

 31  779.76   ANTI    3  3 -.60810     3  2 -.25398   2.59160   2.12986    .26505
                      3  4 -.29025     3  4 -.16348
                      3  5 -.10698     3  3 -.16054
                      3  2 -.08652
                      3  6  .04237

 32  811.04   ANTI    2  4  .44856     2  2 -.33993   2.10595   1.69469    .20392
                      2  5  .28040     2  4 -.28072
                      2  2 -.25218     2  3  .05882
                      2  1 -.14779
                      2  3 -.09074
```

MODE NUMBER 1
FREQUENCY = 188.51
SYMMETRIC MODE
M = 1

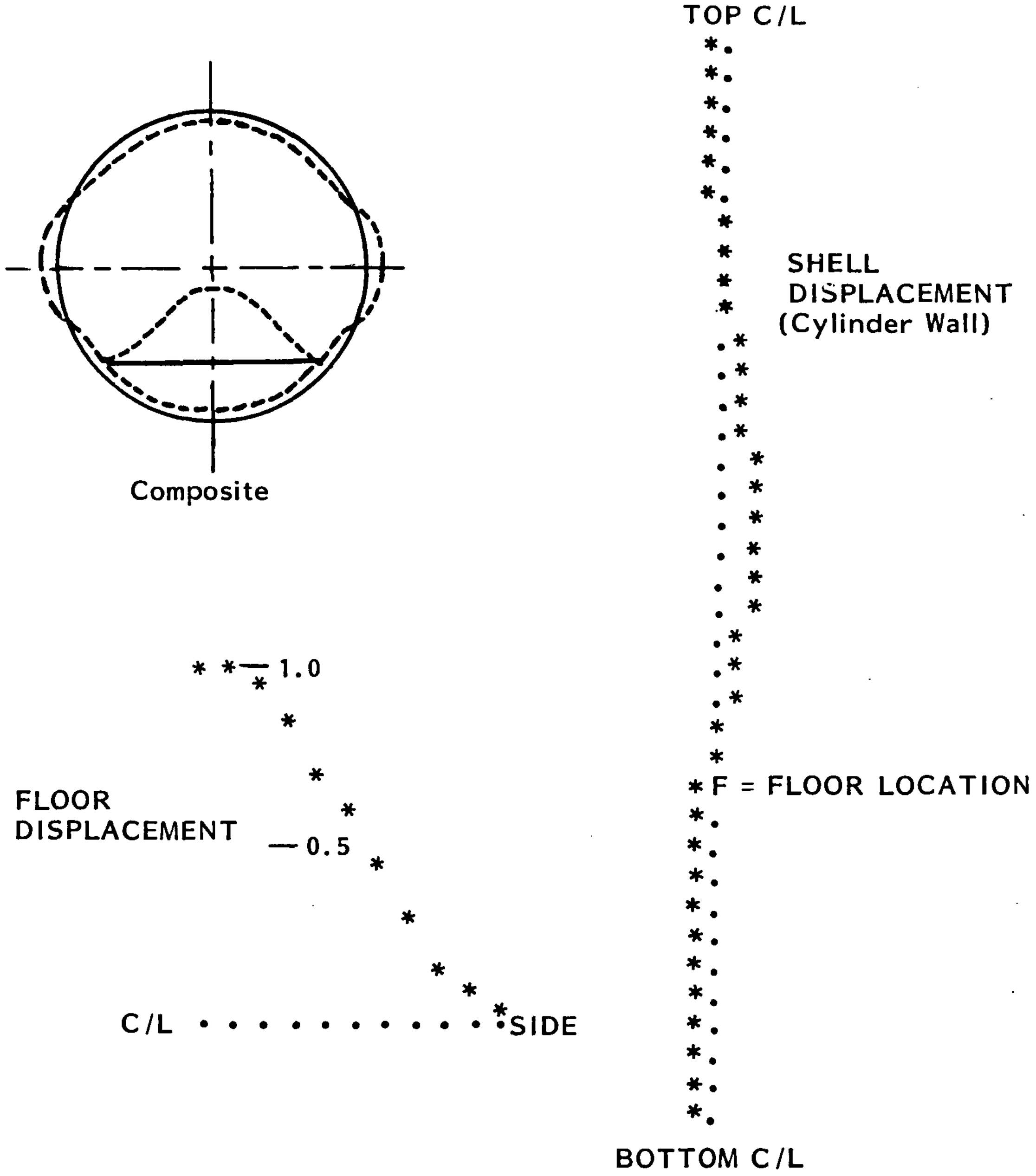

FIGURE D-2. EXAMPLE SHELL MODE (Z DEPENDENCY SUPPRESSED)

Fig.D-3 shows another mode, the sixth mode of Table D-1. It is found to be basically a shell mode.

MODE NUMBER 6
FREQUENCY = 301.93
SYMMETRIC MODE
M = 1

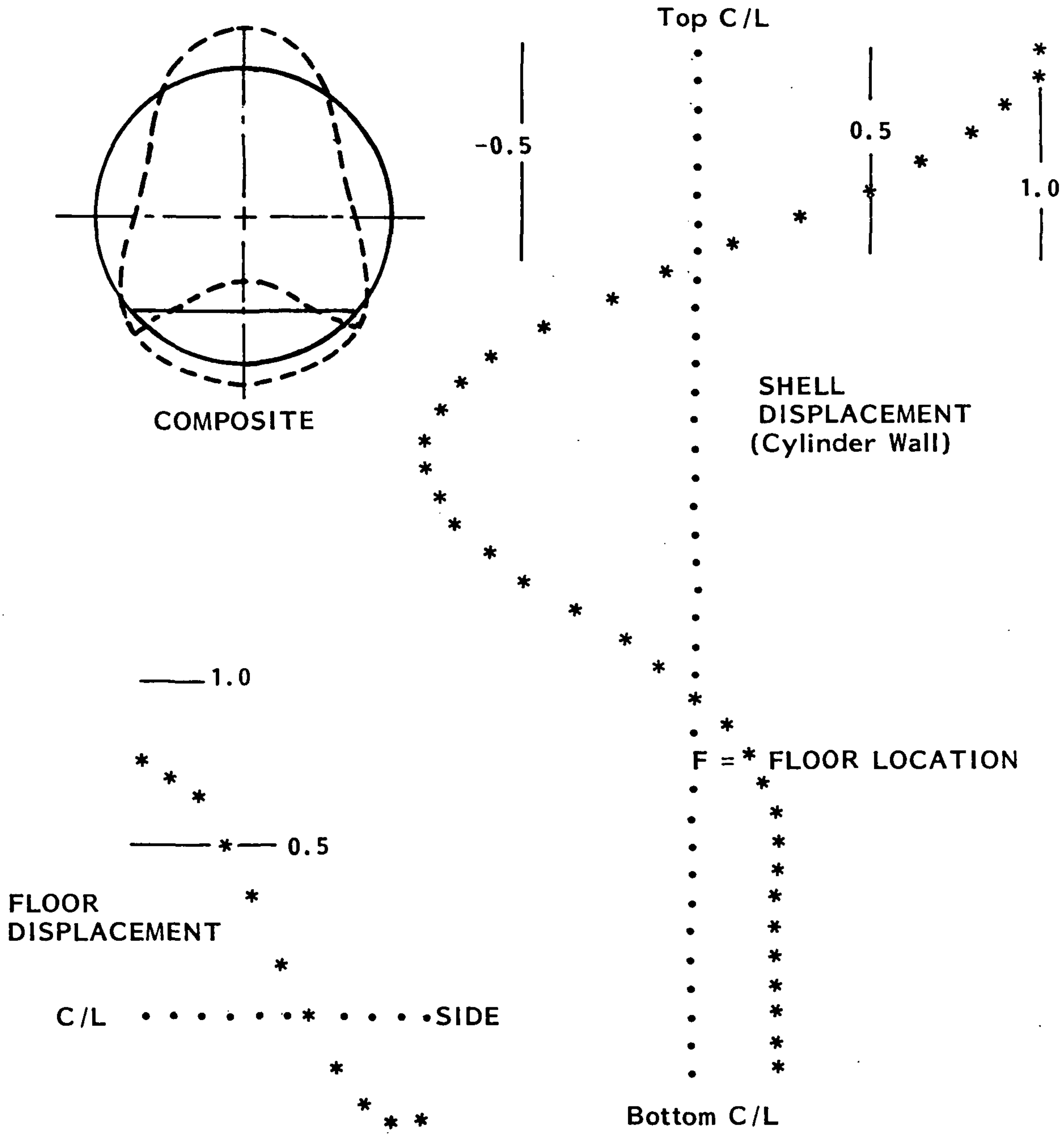

FIGURE D-3. A SECOND EXAMPLE MODE

APPENDIX E

MODEL VALIDATION STUDIES

APPENDIX E - VALIDATION STUDIES

The models of Section 3 are based on fairly precise solutions of the sound transmission problems. Nevertheless, the models will have limited prediction accuracy due to errors inherent in the input data that is used to describe the various physical systems involved, i.e., exterior field, fuselage structure, cabin acoustic space, sidewall trim, etc. The primary goal of the present modeling effort has been to minimize these errors through elaborate, though limited, system models. Although the overall quality that has been achieved is not predictable, it is measurable, and a test has been devised for that purpose.

Test Hardware

The test configuration is very similar to that represented in Figure 1. The actual test rig and hardware are shown in Figures E-1 through E-3. As seen in Figure E-1, the fuselage and the propeller are located downstream of a nozzle that supplies air to simulate airplane forward velocity. The fuselage model itself is a cylinder 1.83m (72 in.) long and 1.02m (40 in.) in diameter. The skin is 0.00081m (0.032 in.) thick and is stiffened by eighteen (18) stringers spaced on 20° centers. The stringers are 90° angles having dimensions of approximately 0.00953 x 0.0112 x 0.00051m (3/8 x 7/16 x 0.020 in.). They are riveted to the inside of the skin and pass through cut-outs in eight (8) internal ring frames that are spaced along the cylinder every 0.2m (8 in.) The frames are aluminum channels with dimensions of approximately 0.017 x 0.038 x 0.00081m (5/8 x 1-1/2 x 0.032 in.).

The cylinder has a structurally integral floor consisting of a 0.00081m (0.032 in.) plate stiffened by floor supports of the same thickness spaced every 0.2m (8 in.). The supports extend

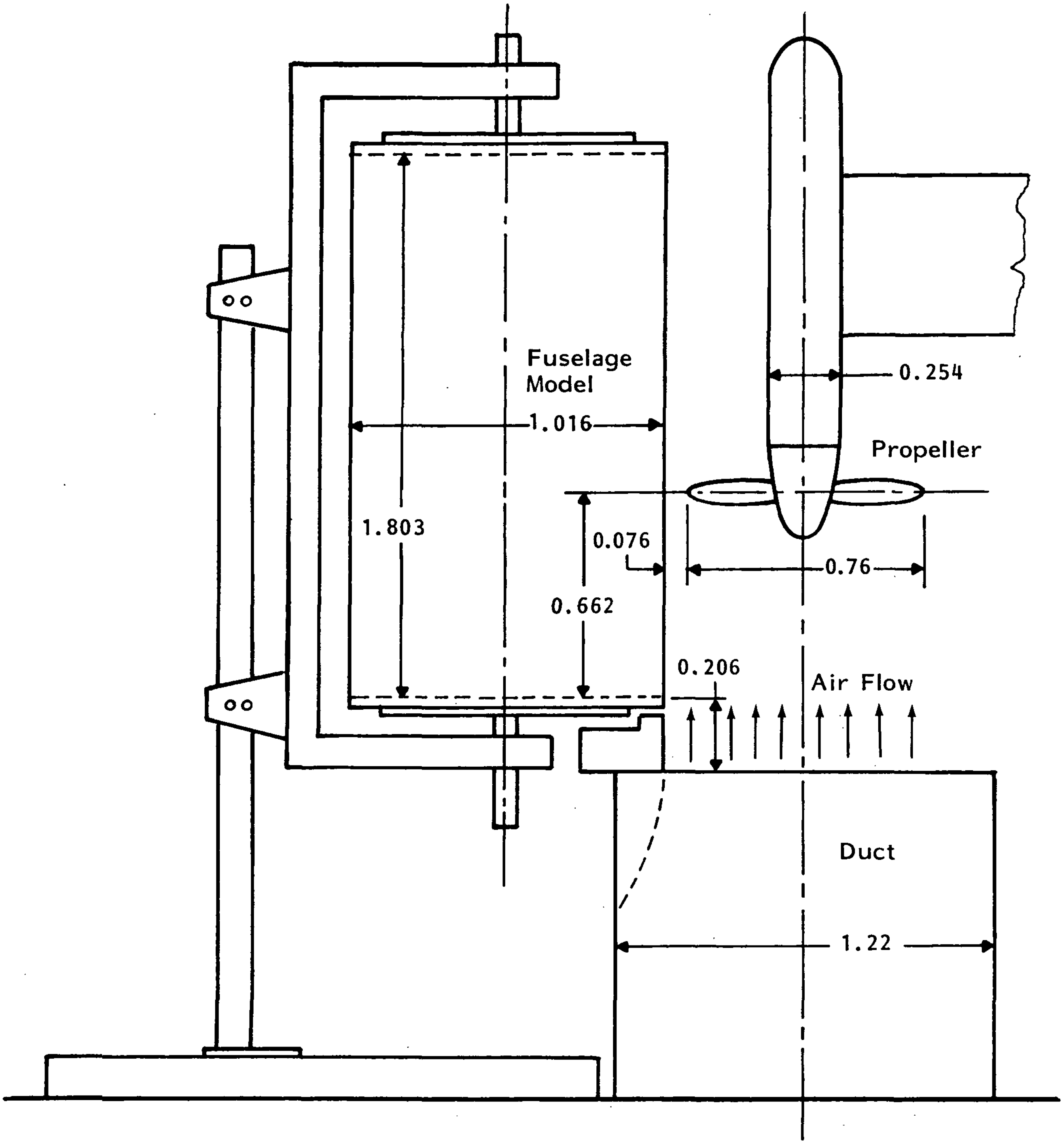

FIGURE E-1. MODEL TEST FACILITY
(Dimensions in meters)

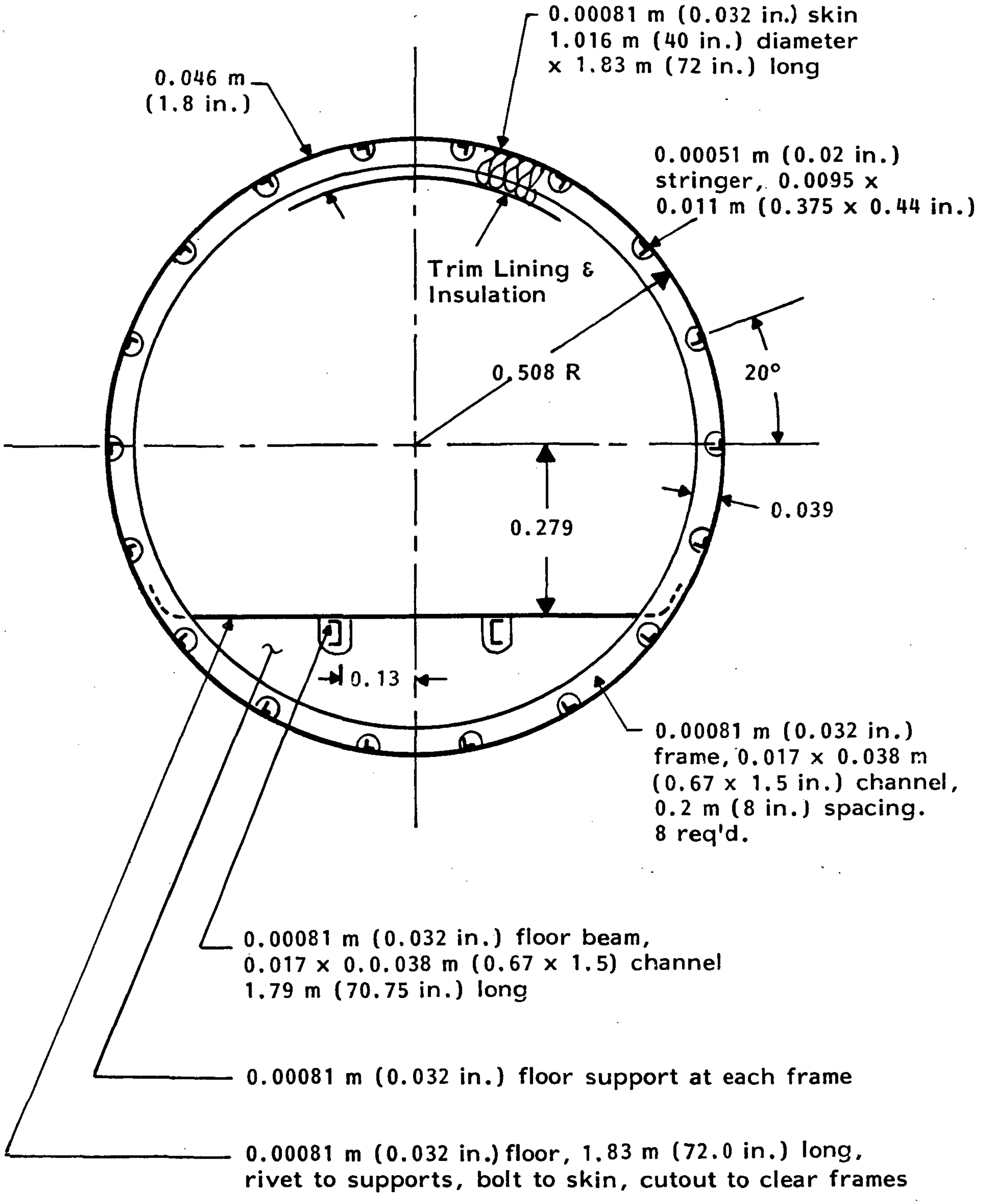

FIGURE E-2. FUSELAGE MODEL

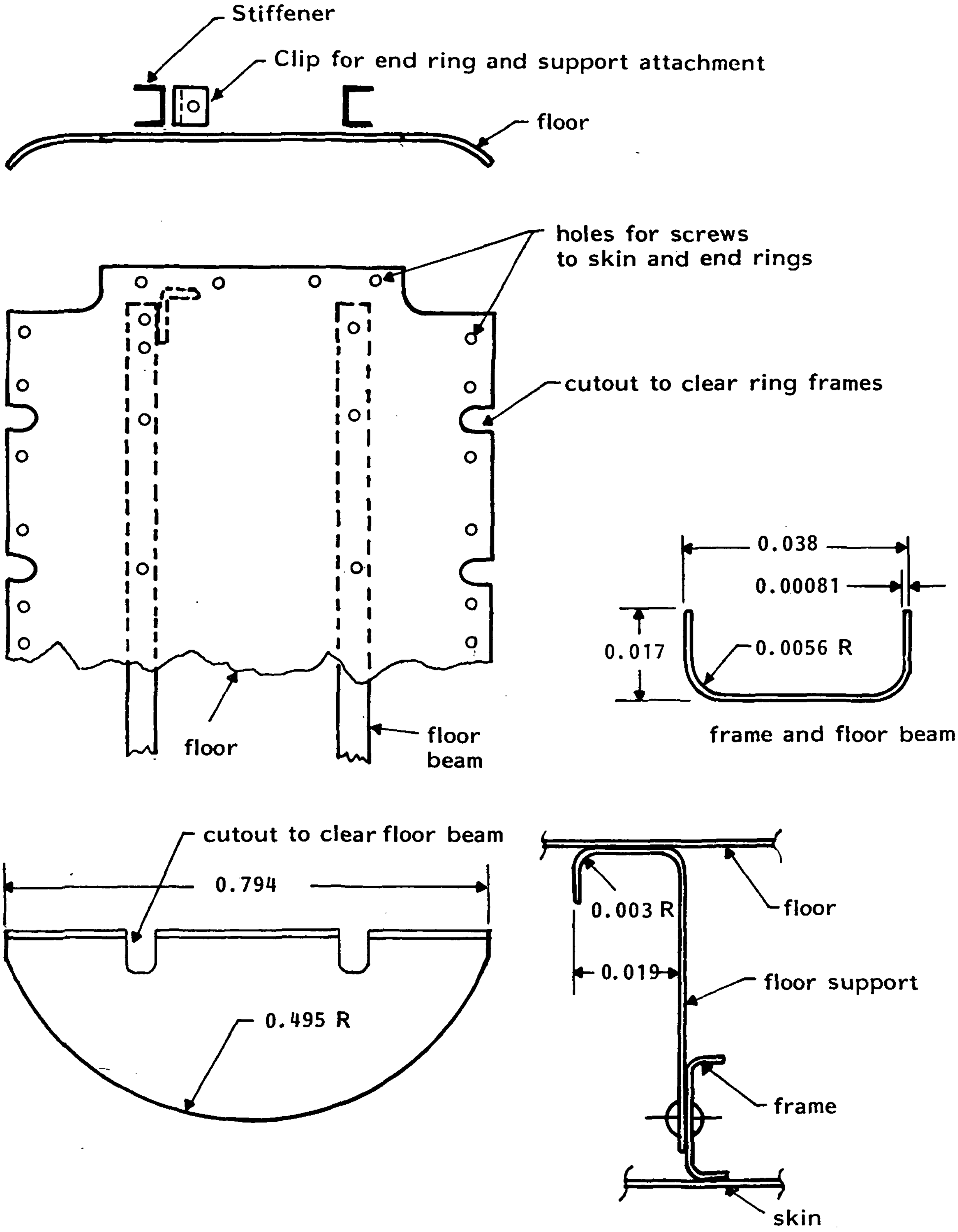

FIGURE E-3. FLOOR ASSEMBLY
(Dimensions in meters)

downward from the floor to the bottom of the cylinder. There are also two floor beams (channels of the same dimensions as the cylinder ring frames) that run longitudinally, each located approximately 0.13m (5.1 in.) from the center of the floor. The width of the floor is 0.85m (33.4 in.) leading to a floor angle θ_o of 56.6 degrees (see Fig.D.1). The outer edge of the floor is bolted to the cylinder wall. The cylinder is closed by 0.013m (1/2 in.) thick end caps that are used to support the cylinder in the NASA Langley propeller test facility. The entire fuselage assembly is constructed of 2024-T3 aluminum.

Propeller

The propeller is a three-bladed, 0.3 scale Hartzell for a Twin Otter aircraft with a diameter of 0.76m (30 in.). It is driven by a 30 kw (40 horsepower) variable speed electric motor capable of turning it up to 8000 rpm. The propeller blades are Series 16 airfoils. The geometry of the blades is specified in the input data to the ANOPP Propeller Noise Prediction program.

The data used to define the particular propeller used in the present test are proprietary and thus are not included here. In the present circumstance the angle-of-attack and local chord are specified as a function of radial location. Airfoil coordinates are specified for several locations and then interpolated as required with a cubic spline to fix these variables at all locations on the blade.

Figure E-4 shows the grid coordinates used for the calculations required in the present test. There are 160 points on the upper quarter of the cylinder. In the present test rig, each position on the grid, i.e., (k,ℓ) lying in the fuselage surface, has coordinates defined by the equivalence relation

$$(k,\ell) \leftrightarrow (x_1^\ell,\ x_2^\ell,\ x_3^k) \quad ,$$

where (in meters):

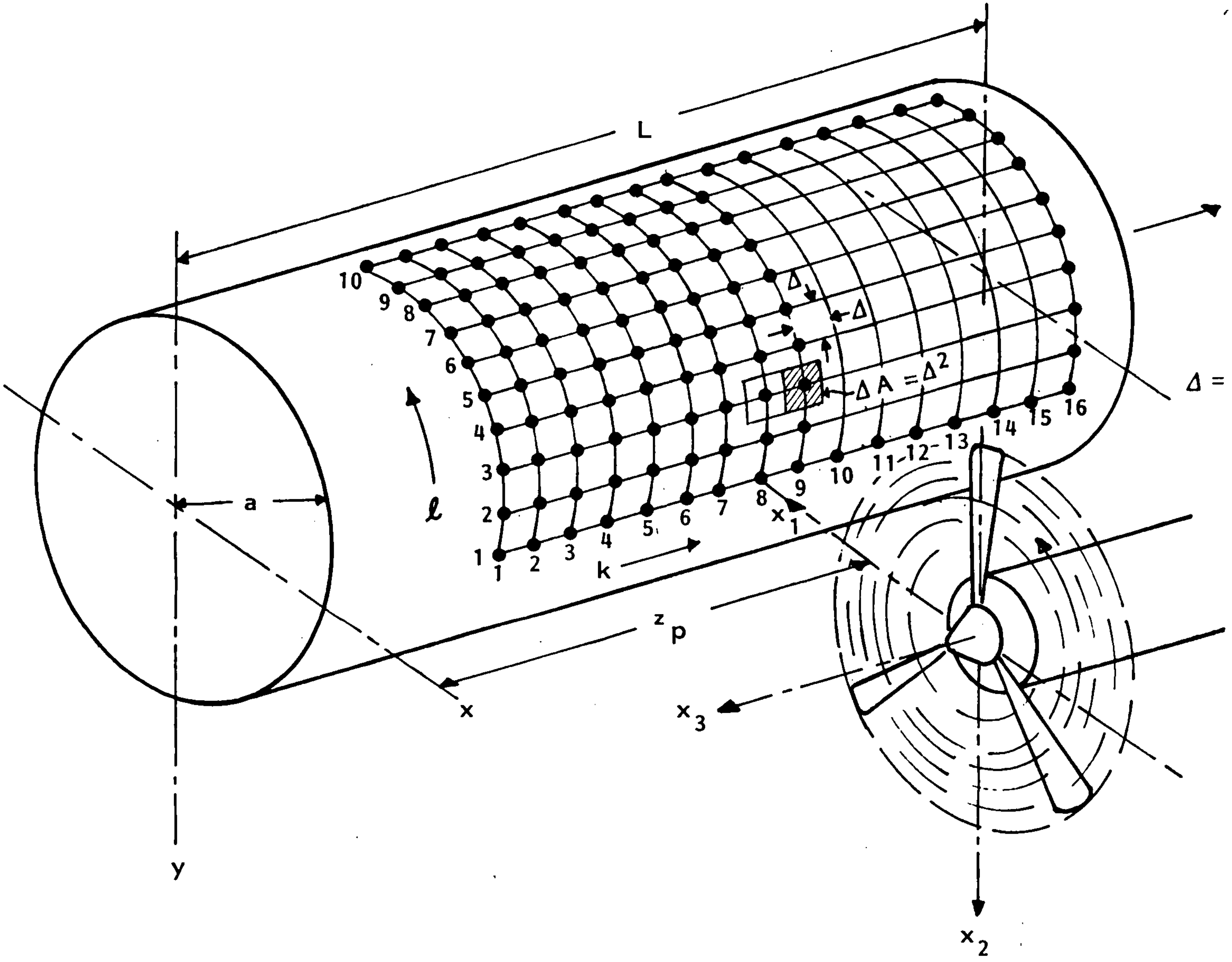

FIGURE E-4. GRID USED FOR PROPELLER NOISE PREDICTIONS

$$x_1^\ell = 0.457 + 0.508\,\{1-\cos[(\ell-1)\cdot\pi/18]\}$$

$$x_2^\ell = -0.508\,\sin[(\ell-1)\cdot\pi/18]$$

and

$$x_3^k = 0.622 - 0.089\,(k-1) \quad .$$

This grid covers all of the upper quarter surface of the cylinder forward of the propeller and a somewhat greater amount behind it. Because of the lengthy calculations involved in the ANOPP program, the data for the lower quarter of the cylinder seen by the propeller are obtained from the data for the top quarter with the relation (imagining an identical grid below the centerline)

$$p(x_1^\ell, x_2^\ell, x_3^k, t) = p(x_1^\ell, -x_2^\ell, x_3^k, t-\tau_{k\ell}) \quad ,$$

where $\tau_{k\ell}$ is a time delay given in milliseconds by the result

$$\tau_{k\ell} = \frac{333.33}{N}\,\alpha_{k\ell} \quad .$$

N is the propeller rpm and $\alpha_{k\ell}$ is in degrees and is given by the result

$$\alpha_{k\ell} = \tan^{-1}[|x_2^\ell|/x_1^\ell] \quad .$$

The propeller harmonic amplitudes at corresponding points above and below the centerline are given by

$$\bar{A}_H^{k\ell}\Big|_{\text{bottom}} = \bar{A}_H^{k\ell}\Big|_{\text{top}} \quad ,$$

and the corresponding phases (in degrees) are related by

$$\phi_H^{k\ell}\Big|_{\text{bottom}} = \phi_H^{k\ell}\Big|_{\text{top}} + \frac{\tau_{k\ell}}{T_1} \times H \times 360° \quad ,$$

where $T_1 = BPF^{-1}$ is in milliseconds and H is the harmonic index. This can also be written as

$$\phi_H^{k\ell}\Big|_{\text{bottom}} = \phi_H^{k\ell}\Big|_{\text{top}} + 2BH\alpha_{k\ell}$$

where B is the number of propeller blades.

Conversion to the coordinate system used in Figures 1 and 2 in the body of this report is with the relations

$$z_k = z_p - x_3^k \quad ,$$

and (using $\phi = \pi/2$ in Fig.2)

$$\theta_\ell = \frac{\pi}{2} + \tan^{-1}\left\{\frac{-x_2^\ell}{r_p - x_1^\ell}\right\} = \phi_p + (\ell-1)\,\frac{\pi}{18} \quad .$$

The coordinates of the grid point (k,ℓ) are given by the equivalence statement

$$(k,\ell) \leftrightarrow (a,\theta_\ell,z_k)$$

In the present test, $r_p = 0.965$m (38 in.) and $z_p = 0.662$m (25.5 in.). The resulting grid has spacing Δ of approximately 0.089m (3.5 in.). This spacing is sufficiently close to assure a relatively smooth change in phase for each propeller harmonic from grid point-to-point.

Test Description

The test program discussed in this appendix was conducted at NASA Langley Research Center by NASA personnel. The main test involved the transmission of propeller noise into the interior of the model cylinder. For this test the cylinder and propeller were mounted in an anechoic chamber in the configuration shown in Figure E-1. Additional tests were performed in a reverberation chamber to measure the noise reduction associated with a reverberant sound field. Also, decay measurements were made on the acoustic field in the cylinder and the structural vibration of the cylinder to determine empirical loss factors.

The interior of the cylinder was treated with fiber glass blankets with a density of 9.61 kg/m^3 (0.6 lb/ft^3). The blankets were applied in layers which were nominally 1.3 cm (0.5 inch) thick, four layers with a total nominal thickness of 5.1 cm (2 inch) being applied to the curved surfaces and one layer to the end plates. One face of each layer had a vinyl facing with a thickness of 0.005 (0.002 inch); the total surface density of one layer plus facing was 0.22 kg/m^2 (0.045 lb/ft^2). On the curved surface, three of the fiberglass layers were placed between the frames and the fourth layer covered the frame caps. The inner surface of the fiberglass treatment on the curved walls was covered with a trim septum consisting of a sheet of epoxy/fiberglass NEMA G-10 (0.079 cm or 0.031 inch thick) from floor to floor, and a sheet of vinyl (of the same thickness) over the upper 120° of the cylinder. The installation is shown diagrammatically in Figure E-5. The trim was hard-mounted to the floor and attached to the frames by nine soft-mounted screws. The total weight of the trim septum was 6.58 kg (14.51 lb).

During the propeller noise test, sound levels inside the cylinder were measured using an array of eleven microphones which could be located at any selected station along the cylinder and could be rotated about the cylinder axis. Measurements were made at a total of 196 locations, consisting of 49 locations at each of four axial stations. The stations were chosen so that the interior of the cylinder was divided into four segments of equal volume. Figure E-6 shows the microphone locations on the rotating array. The array was positioned at angular locations = 0°, ± 51.5° and ±103°. The radial positions of the microphones were chosen such that all microphones were associated with approximately equal cross-sectional areas. The sound levels measured at the different microphone locations were averaged on an energy basis to obtain space-average sound pressure levels for each measurement axial station and for the cylinder as a whole.

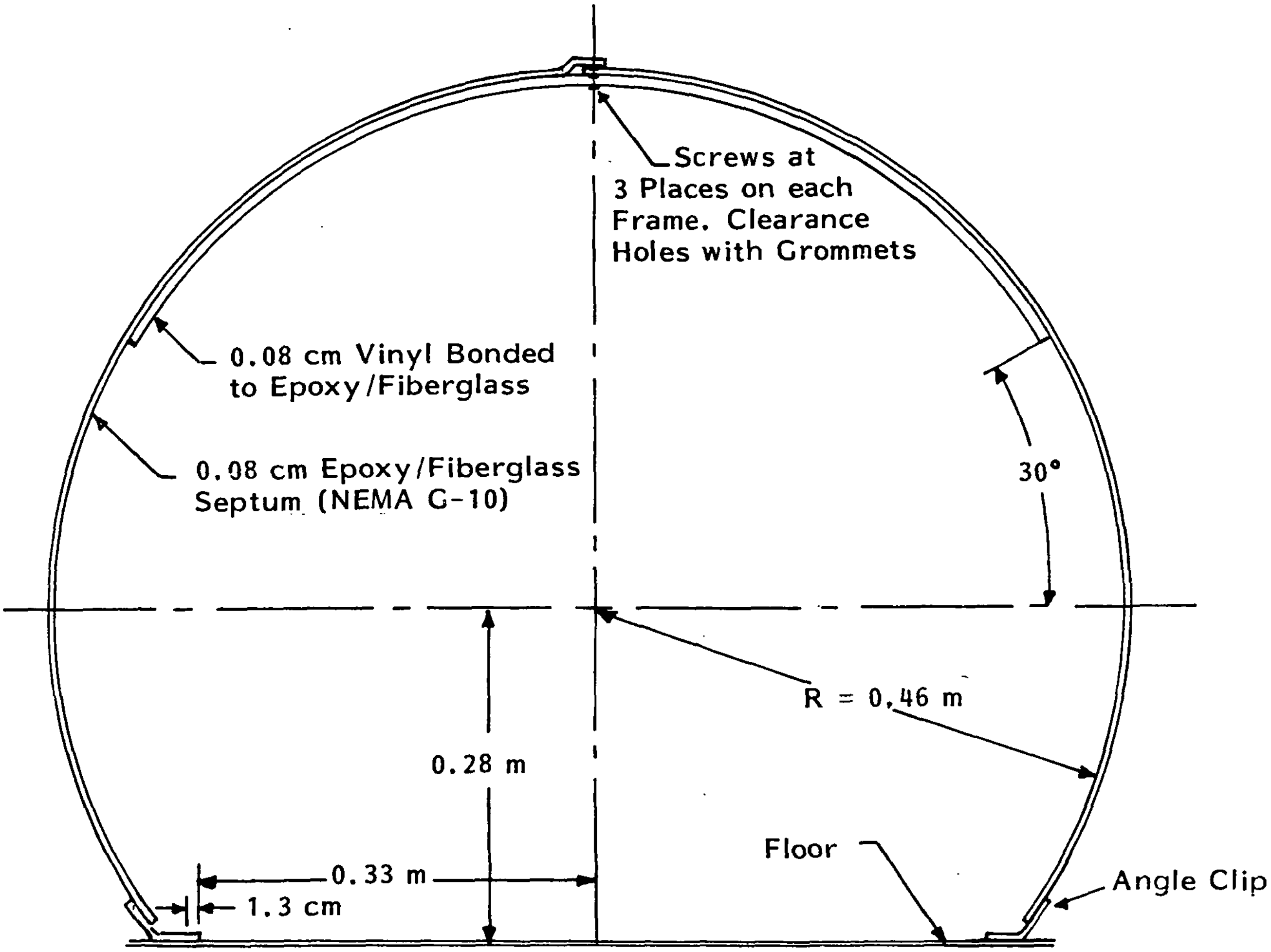

FIGURE E-5. CROSS-SECTION OF TEST CYLINDER SHOWING TRIM

Mic	r/R
1,9	.250
2,10	.433
3,11	.559
4	.661
5	.750
6	.829
7	.901
8	.968

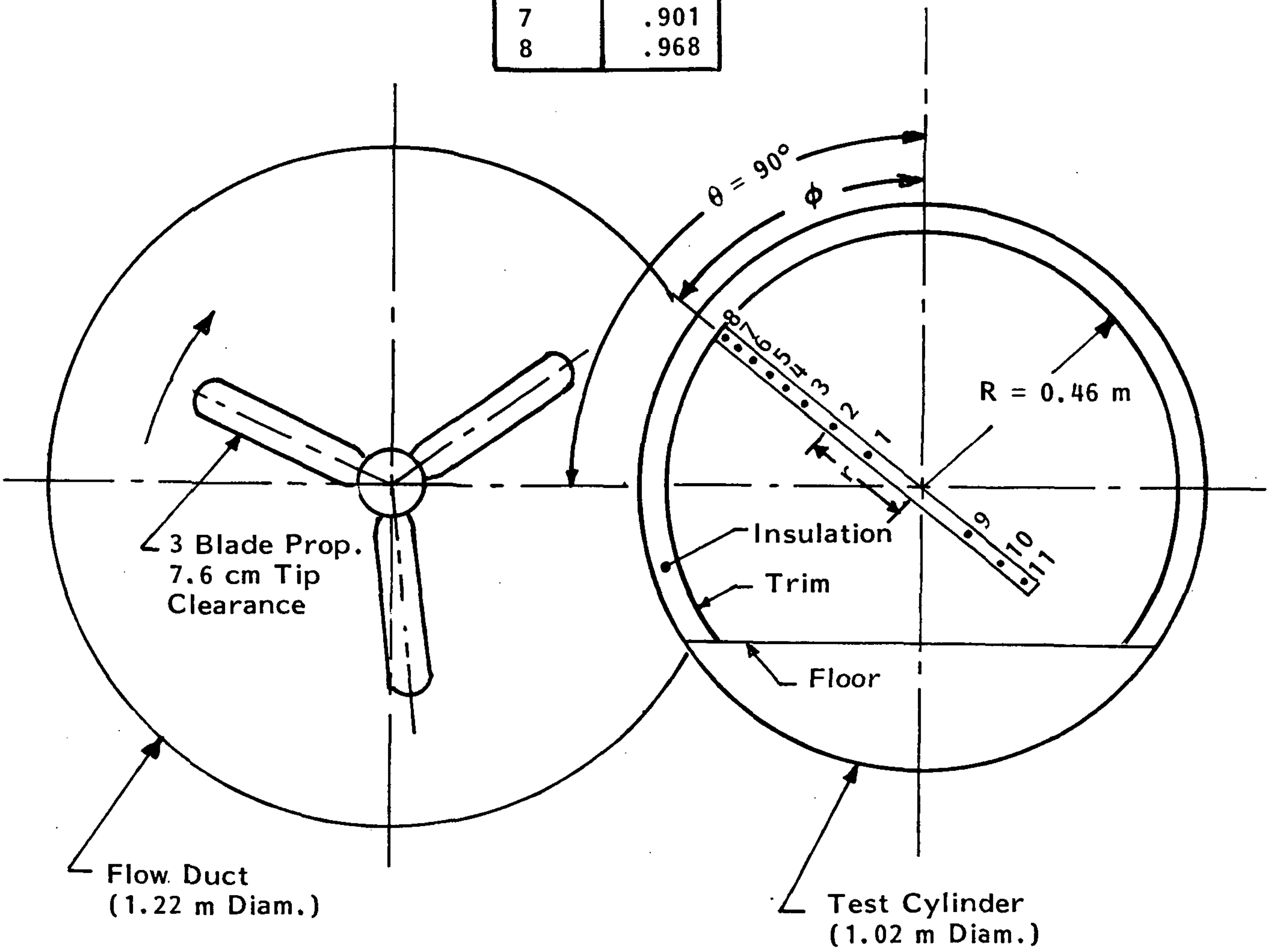

FIGURE E-6. MICROPHONE LOCATIONS IN TEST CYLINDER

Measurements were made by NASA at several test conditions, but results for only one condition are considered in this appendix. The airflow speed into the propeller was 23.8 m/s (78 ft/sec) and the propeller rotational speed was 4000 rpm. The resulting fundamental, or first harmonic, of the blade passage frequency is 200 Hz.

In the case of the noise reduction tests for reverberant excitation, sound levels were measured at only two axial stations, one at the mid-point of the cylinder and the other at the one-sixth point. Symmetry was then assumed about the mid-point of the cylinder length in order to calculate space-average sound pressure levels.

The bulk of the data reduction was performed in terms of one-third octave band spectra. However, a small amount of narrowband analysis was performed in order to obtain a better understanding of the data.

Measured Interior Sound Levels

Typical narrowband sound pressure level spectra measured at two locations in the cylinder are shown in Figure E-7. The two selected locations are close to the plane of rotation of the propeller ($x_3/D = 0.015$ where D is the propeller diameter), microphone #1 being near to the center of the cylinder and #8 near to the periphery (as shown in Figure E-6). Figure E-7 shows that the contributions associated with the three lowest-order harmonics are easily identified but that contributions from higher-order harmonics may be difficult to identify. This masking of the discrete frequency components by the broadband signal limits the upper frequency bound on the useful propeller noise data, particularly when, as in the present case, much of the data presentation is in terms of one-third octave band spectra.

Station 1.1 cm aft of Propeller Plane, ϕ = 103°

(a) Microphone 1, r = 11.6 cm

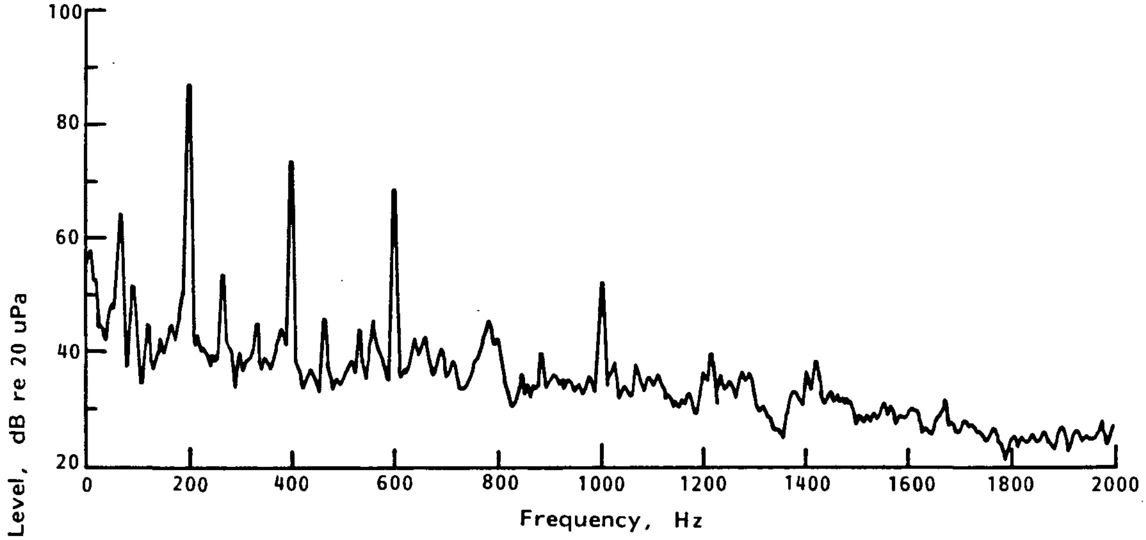

(b) Microphone 8, r = 44.7 cm

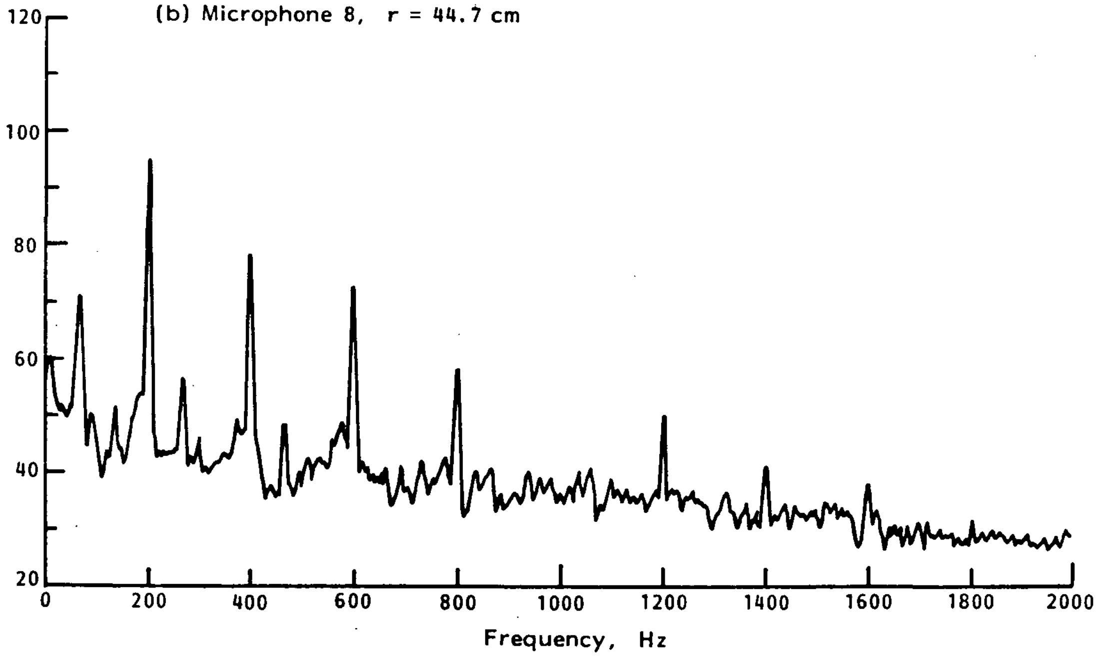

FIGURE E-7. TYPICAL NARROWBAND SPECTRA OF INTERIOR SOUND PRESSURE LEVELS

Average one-third octave band sound pressure level spectra are shown in Figure E-8 for each of the four axial stations of the microphone array. Little variation in sound pressure level is observed from station to station. The space-average spectrum for the cylinder as a whole is plotted in Figure E-9, which also contains the range of measured sound pressure levels. The space-average values are compared in Figure E-10 with associated 95% confidence limits. Because of the large number of samples, the 95% confidence intervals are small.

The spectra show distinct peaks in the frequency bands centered at 200, 400 and 630 Hz, the sound levels in these bands being controlled by the contributions from the first, second and third harmonics of the blade passage frequency. At higher frequencies, the broadband contributions become important, as indicated in Figure E-7, and the one-third octave band spectra are relatively smooth. The harmonic components may be significantly lower in level than are the corresponding one-third octave band levels.

Propeller Noise Field

The analytical model to predict sound levels in the cylinder uses, as data input, a description of the propeller noise field (in terms of pressure amplitude and phase) computed for free-field conditions using the NASA ANOPP computer program. The blocked pressures are then calculated within the present analytical model using the relationship given in Eq.(43).

During the test program at NASA, sound pressure levels were measured at several free-field locations surrounding the model propeller, and at other locations on a rigid-wall cylinder placed close to the propeller. A brief comparison of the measured and predicted sound levels has been performed to get an indication of the accuracy with which the predictions fit the

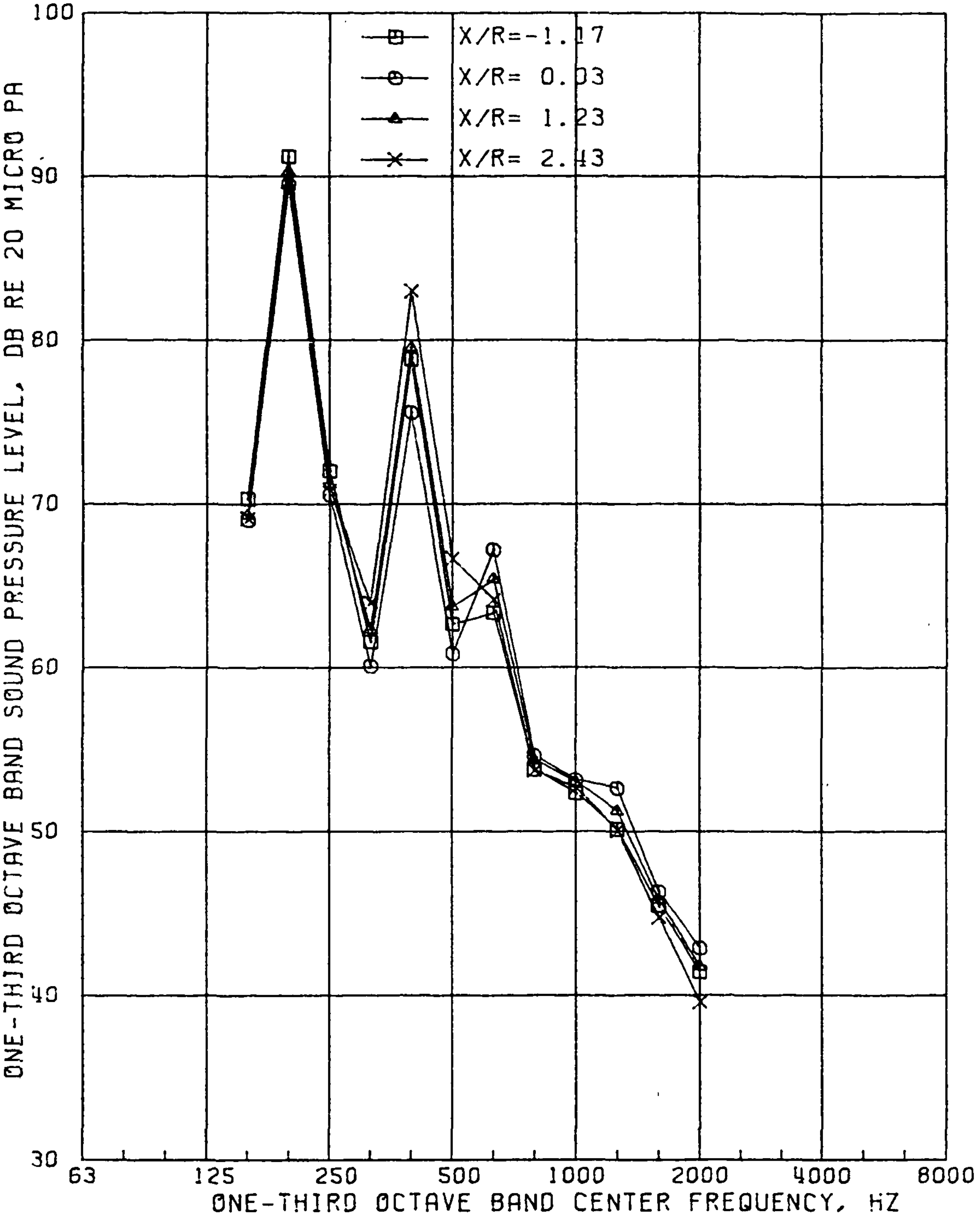

FIGURE E-8. AVERAGE SOUND PRESSURE SPECTRA IN CYLINDER AT DIFFERENT MEASUREMENT STATIONS (PROPELLER NOISE EXCITATION)

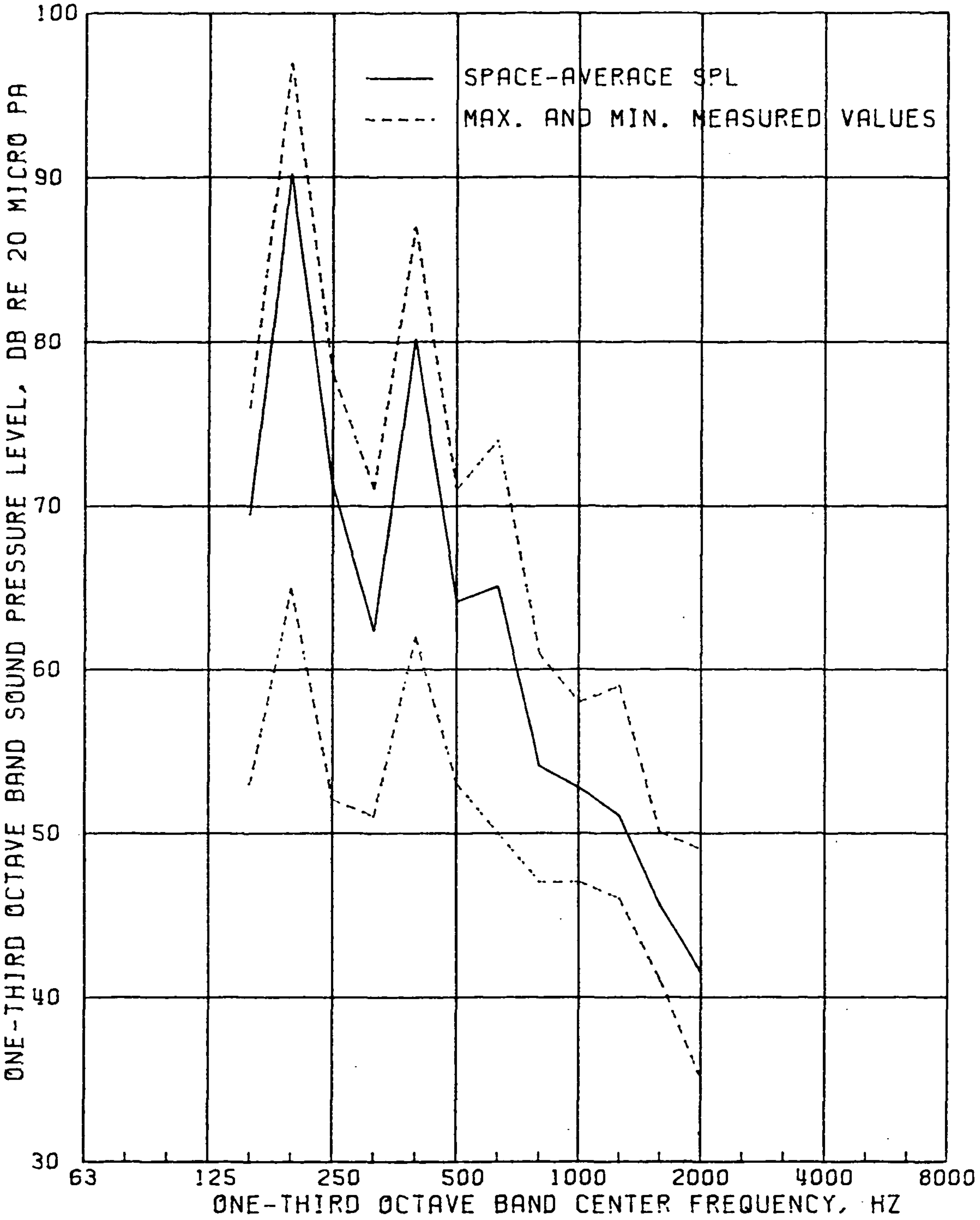

FIGURE E-9. SPACE-AVERAGE AND RANGE OF VALUES FOR PROPELLER-INDUCED SOUND LEVELS INSIDE TEST CYLINDER

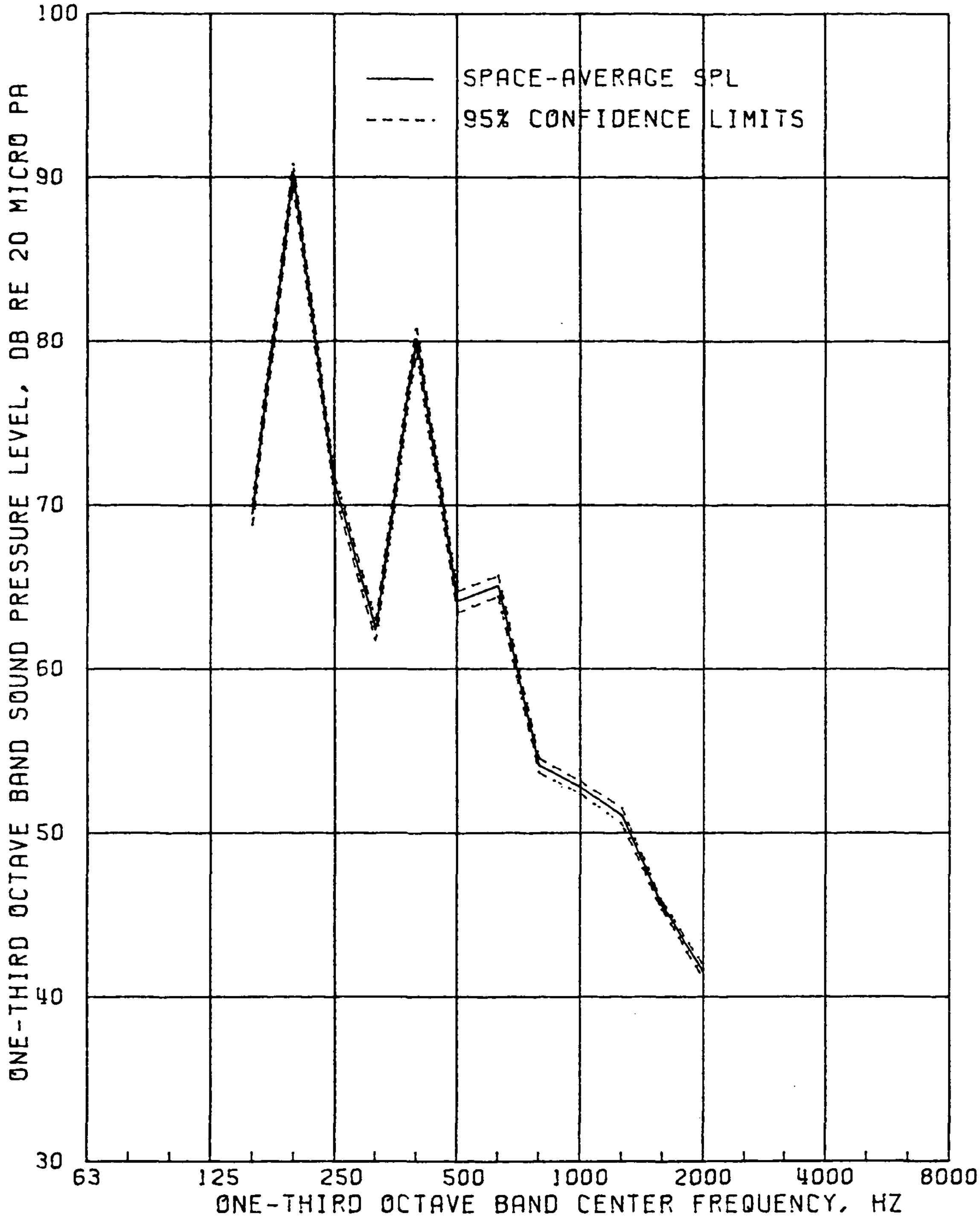

FIGURE E-10. SPACE-AVERAGE AND 95% CONFIDENCE LIMITS FOR PROPELLER-INDUCED SOUND LEVELS INSIDE TEST CYLINDER test environment. This comparison was made for axial locations associated with grid line $\ell = 1$ shown in Figure E-4. The comparison was restricted to pressure level, because no phase data were available from the test program.

The comparison of measured and predicted free-field pressure levels is shown in Figure E-11. In this case both the measurements and the predictions were performed by NASA personnel. The agreement is generally good except at large distances from the plane of rotation where the pressure levels are relatively low and could be affected by broadband flow noise.

Figure E-12 contains the corresponding comparison for the pressure field on a rigid cylinder (i.e., the blocked pressure). The test data were obtained directly from NASA measurements and the predictions from the application of Eq.(43) to the output of ANOPP. The equation provides an empirical relationship for calculating the effect of pressure reflections at the surface of the cylinder. In general the predicted levels are higher than the measured values, the differences being 0 to 5 dB at locations in the neighborhood of the plane of rotation where the pressure levels are highest.

Acoustic Loss Factors

Acoustic reverberation decay measurements were made inside the test cylinder using pink noise and sinusoidal excitations. Acoustic absorption coefficients were computed from the reverberation time T_R using the relationship

$$\alpha = \frac{17.6\pi V}{c_o S T_R}$$

where S and V are, respectively, the surface area and volume of

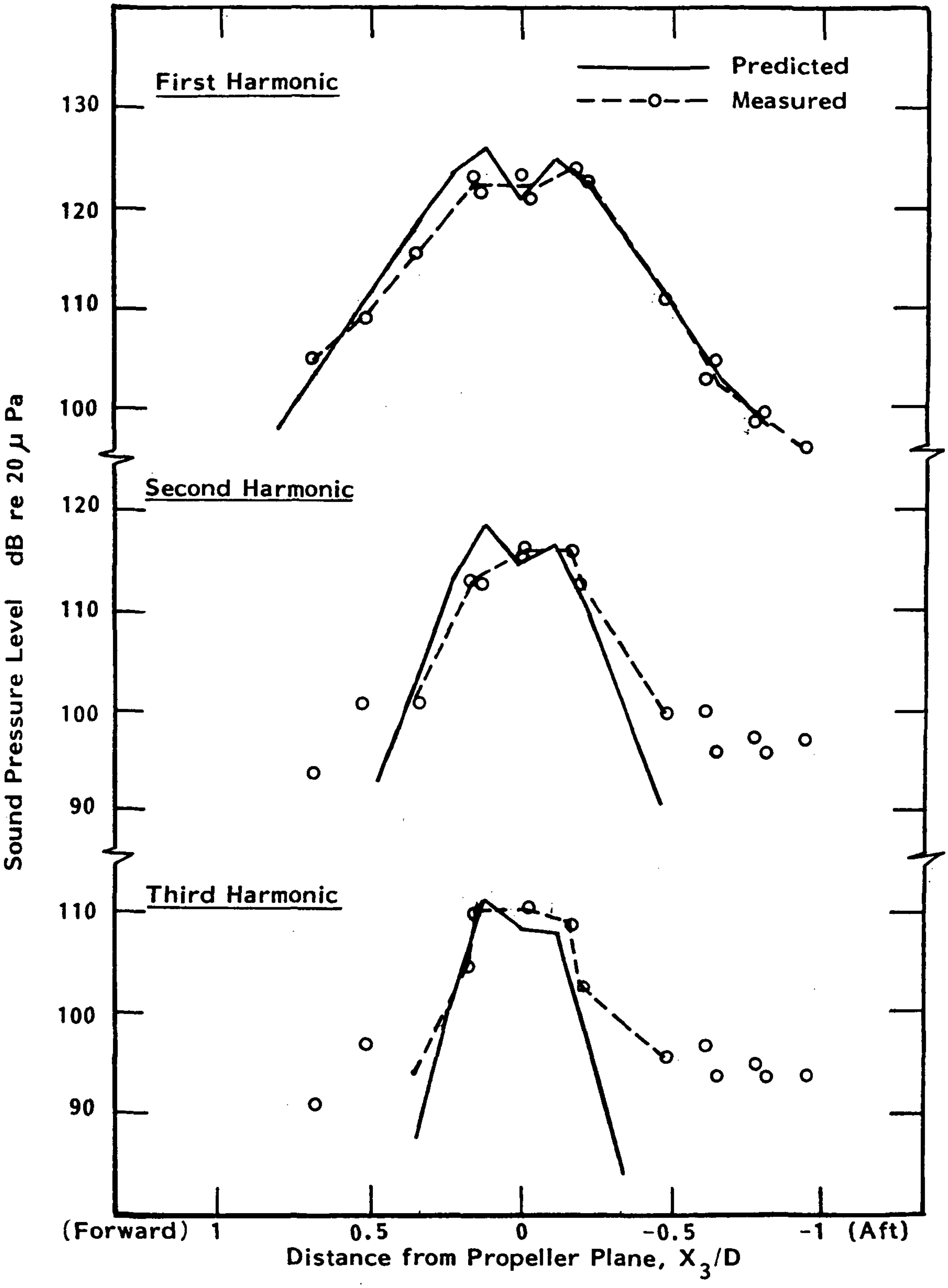

FIGURE E-11. MEASURED AND PREDICTED FREE-FIELD SOUND LEVELS FOR TEST PROPELLER

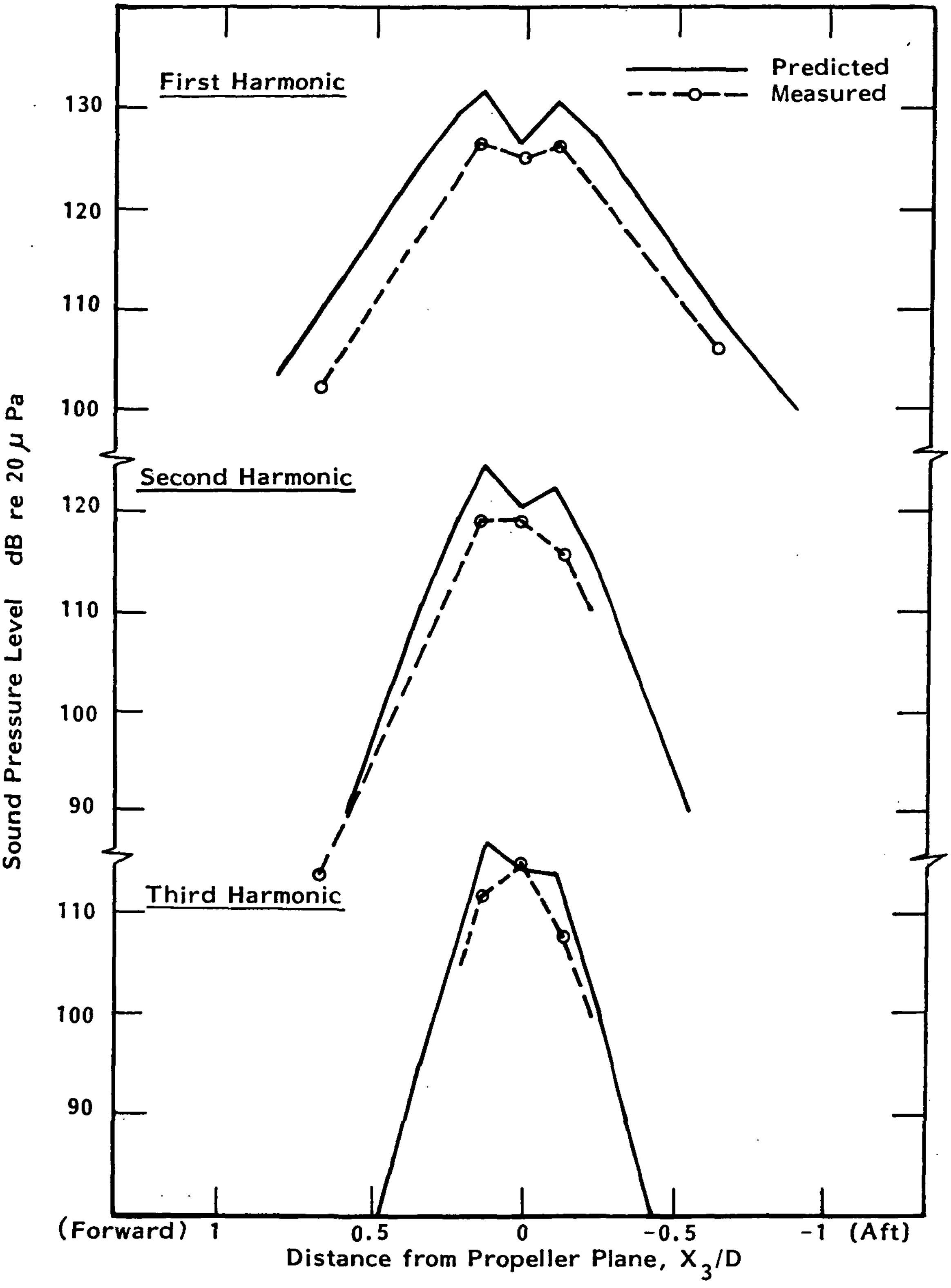

FIGURE E-12. MEASURED AND PREDICTED BLOCKED SOUND LEVELS INDUCED BY PROPELLER ON TEST CYLINDER the interior of the cylinder. Values of α, averaged over approximate one-third octave bands, are given in Figure E-13.

The acoustic loss factor η_n was computed from the equation

$$\eta_n = \frac{c_o S\alpha}{4\omega V}$$

Resulting values for the acoustic loss factor are plotted in Figure E-14.

Also contained in Figure E-14 are band-average values of the acoustic loss factor calculated using the analytical model outlined in Appendix A. It is necessary in this analytical model to assign a value to the structural loss factor η_T of the trim septum. A value of 0.5 was assumed in [7] for the trim loss factor, on the basis of the best fit with test data then available. The same value was assumed initially for the present analysis. At frequencies above 500 Hz, the measured data are scattered about the predicted spectrum, but at lower frequencies the predicted values are significantly higher than the measurements.

When the trim structural loss factor was increased by a factor of 2 to a value of 1.0, the calculated acoustic loss factor decreased in the 250 Hz band (which contains a predicted resonance frequency of the trim) but the change at other frequencies was small or negligible. The disagreement between measurements and predictions in the lower frequency range was not affected to any significant extent.

Structural Loss Factor

The damping of the cylinder structure was determined experimentally from vibration decay measurements using sinusoidal

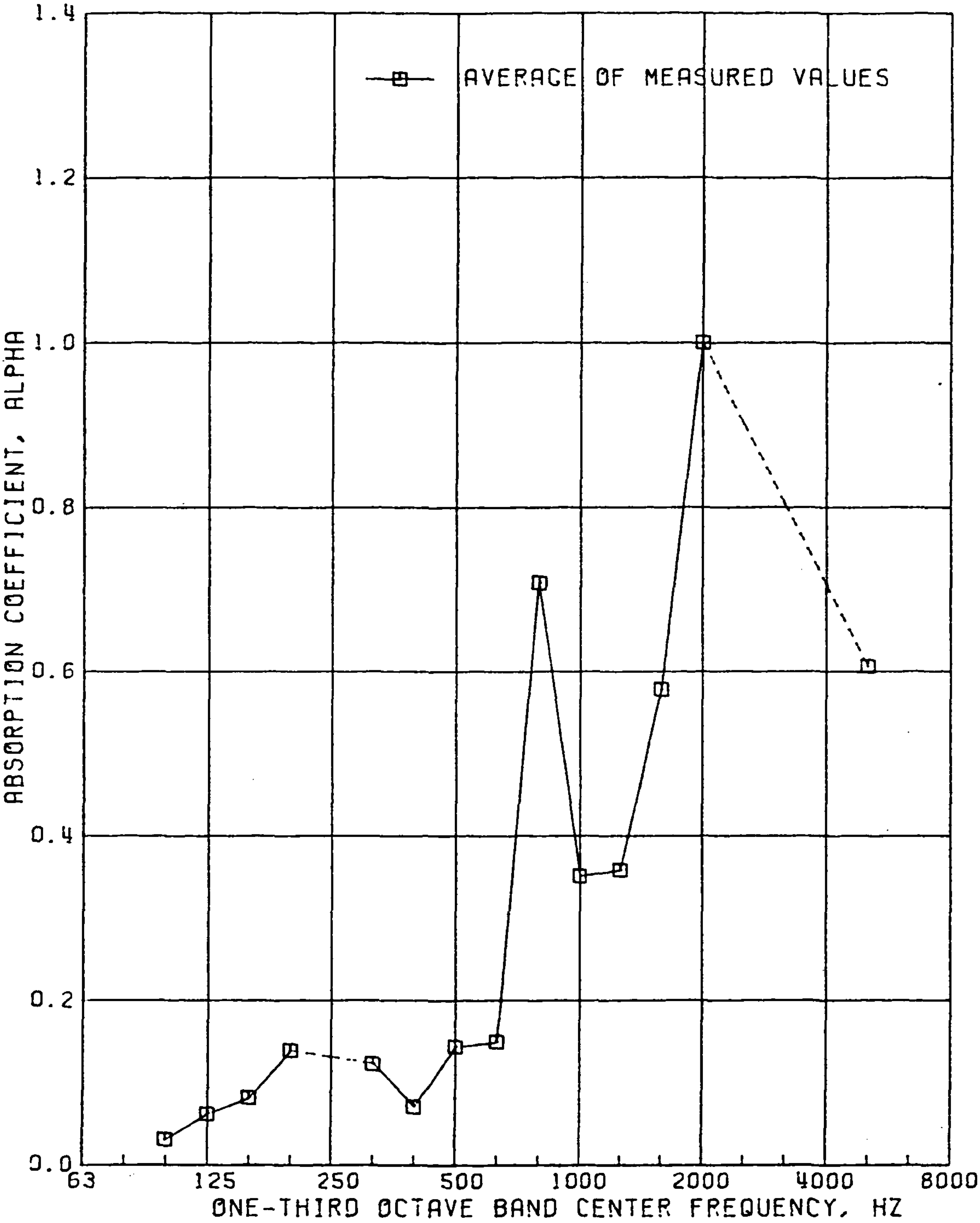

FIGURE E-13. MEASURED ACOUSTIC ABSORPTION COEFFICIENTS IN TEST CYLINDER

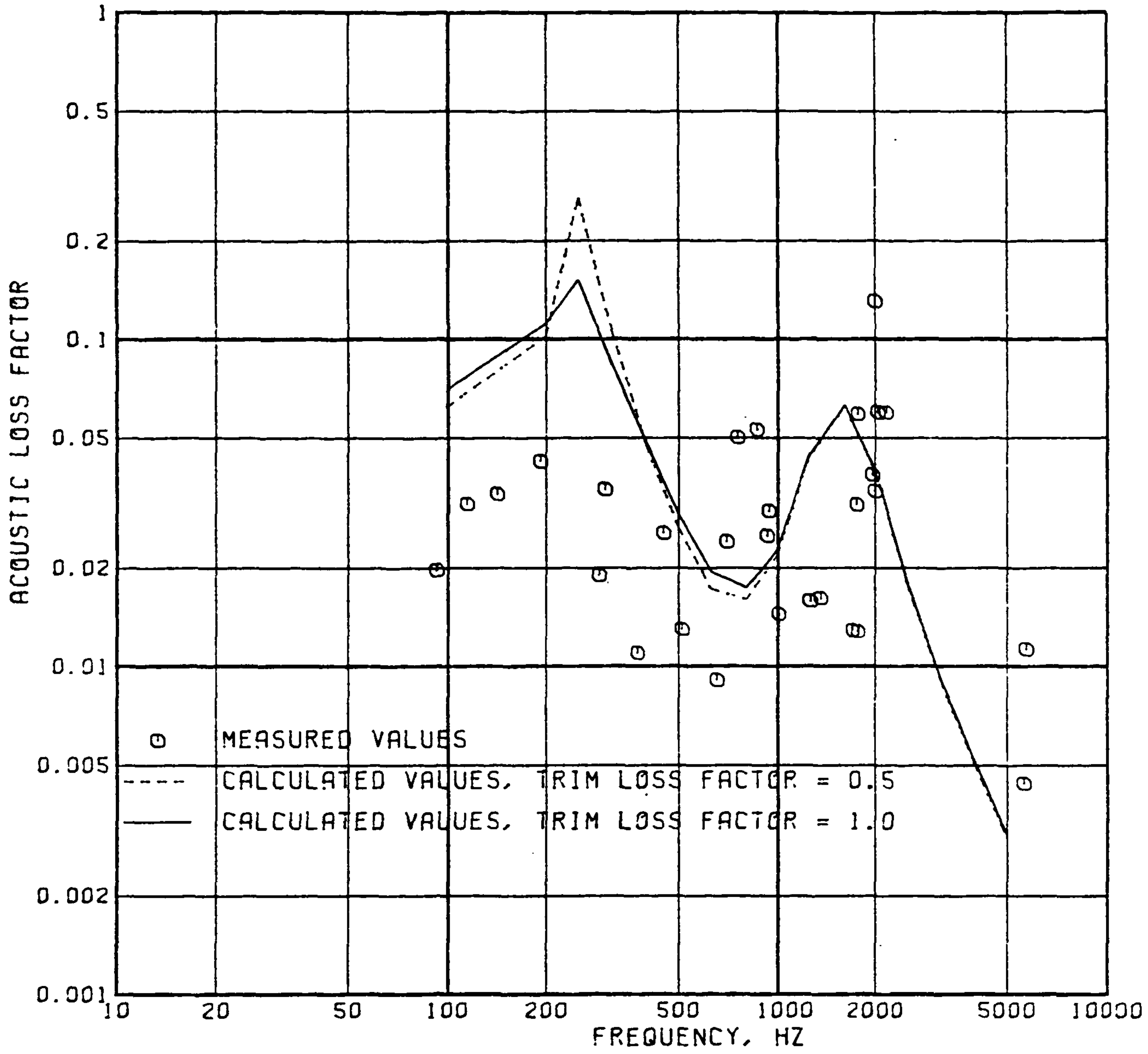

FIGURE E-14. MEASURED AND PREDICTED ACOUSTIC LOSS FACTORS FOR INTERIOR OF TEST CYLINDER (5.1 CM FIBERGLASS PLUS TRIM) excitation. The resulting empirical values are plotted in Figure E.15, where they are compared with band-average values predicted on the basis of the analytical model given in Appendix A. The analytical model includes the influence of the sidewall trim and requires, as an input, an assigned value for the trim structural loss factor η_T. The two calculated loss factor spectra in Figure E-15 assumed trim loss factors of 0.5 and 1.0.

The comparison of measured and predicted values shows good agreement at frequencies above 400 Hz, but the single experimental data point at lower frequencies is an order of magnitude smaller than the corresponding predicted values. For diagnostic purposes, an alternative analytical representation was constructed whereby the structural loss factor was arbitrarily limited to a maximum value of 0.15 in the frequency band below 400 Hz.

Predicted Interior Sound Levels

The model scale experiments discussed in the preceding sections of this appendix were performed in order to obtain data for comparison with sound levels predicted using the analytical model described in this report. The predictions were made using a computer program based on the analytical model outlined in this report.

Initially, the interior sound levels were calculated without placing any restraints on the structural loss factor for the cylinder and with an assumed structural loss factor for the trim of $\eta_T = 0.5$. Space-average sound pressure levels were computed for the five lowest-order harmonics of the propeller blade passage frequency. These levels are compared in Figures E-16 with the range of measured values and the associated space-average levels, and in Figure E-17 with the average and 95% confidence limits. The predicted sound levels refer to discrete

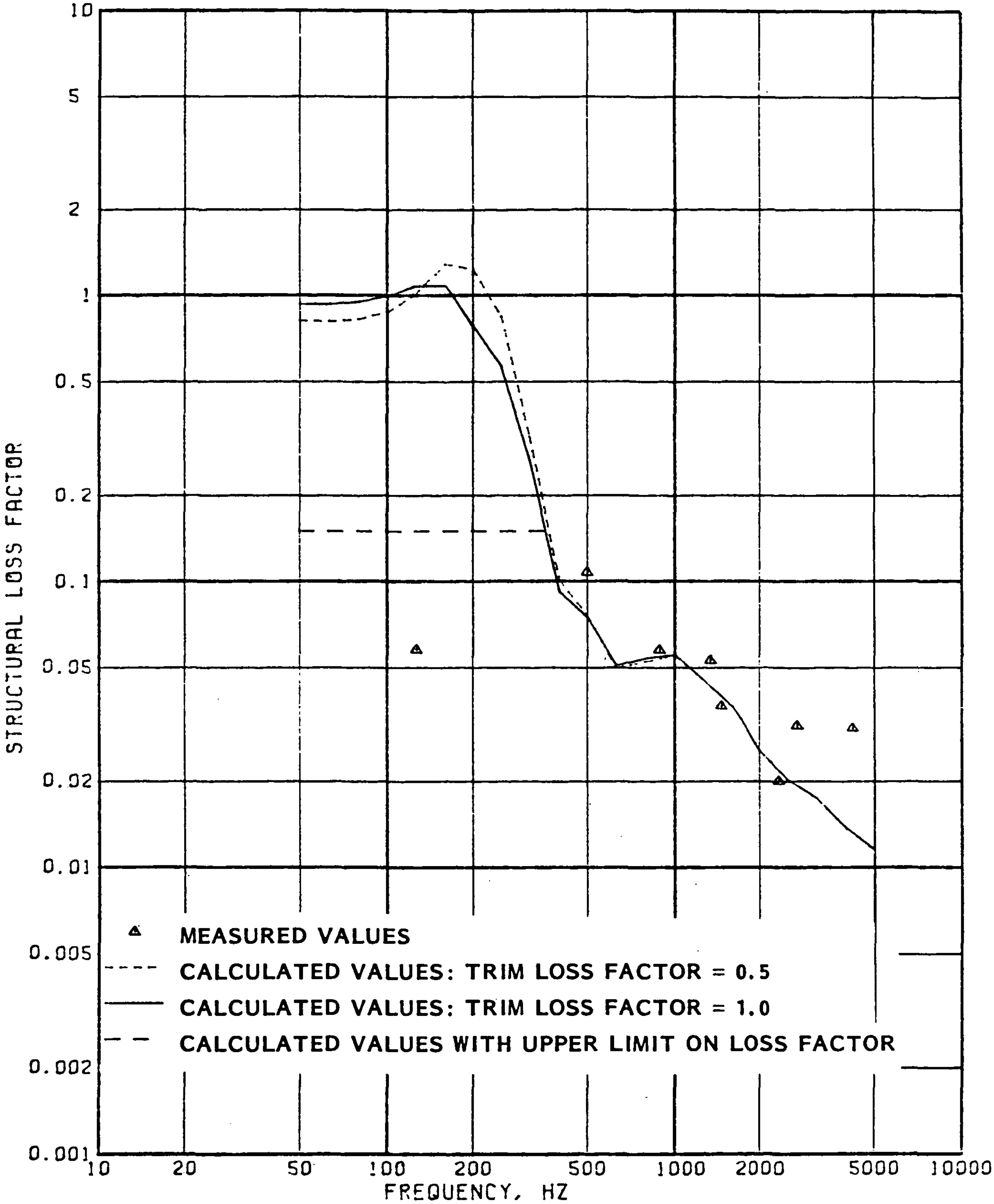

FIGURE E-15. MEASURED AND PREDICTED TOTAL STRUCTURAL LOSS FACTORS FOR TEST CYLINDER

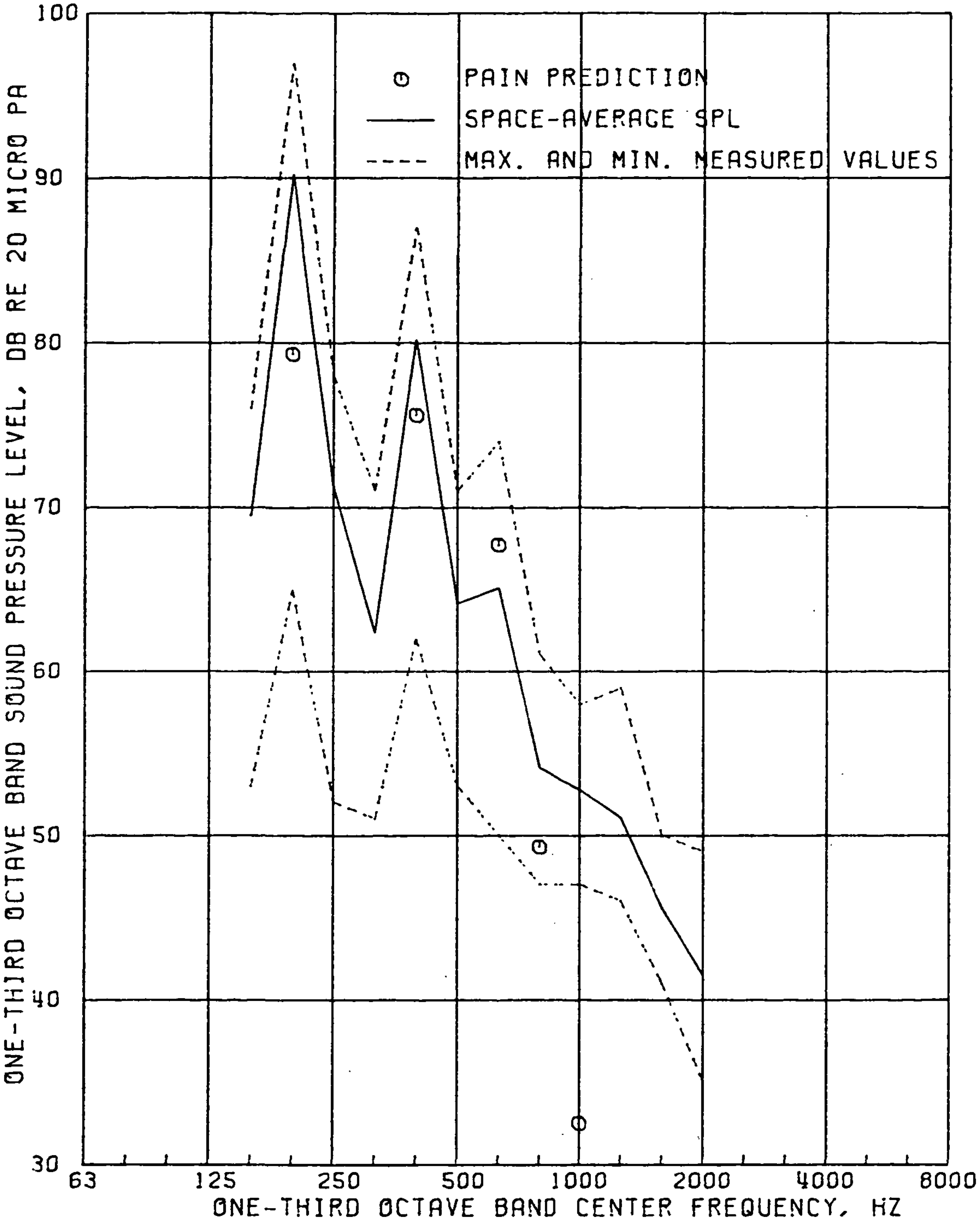

FIGURE E-16. COMPARISON OF PREDICTED AND MEASURED SOUND LEVELS IN CYLINDER INDUCED BY PROPELLER (MEAN AND RANGE OF VALUES)

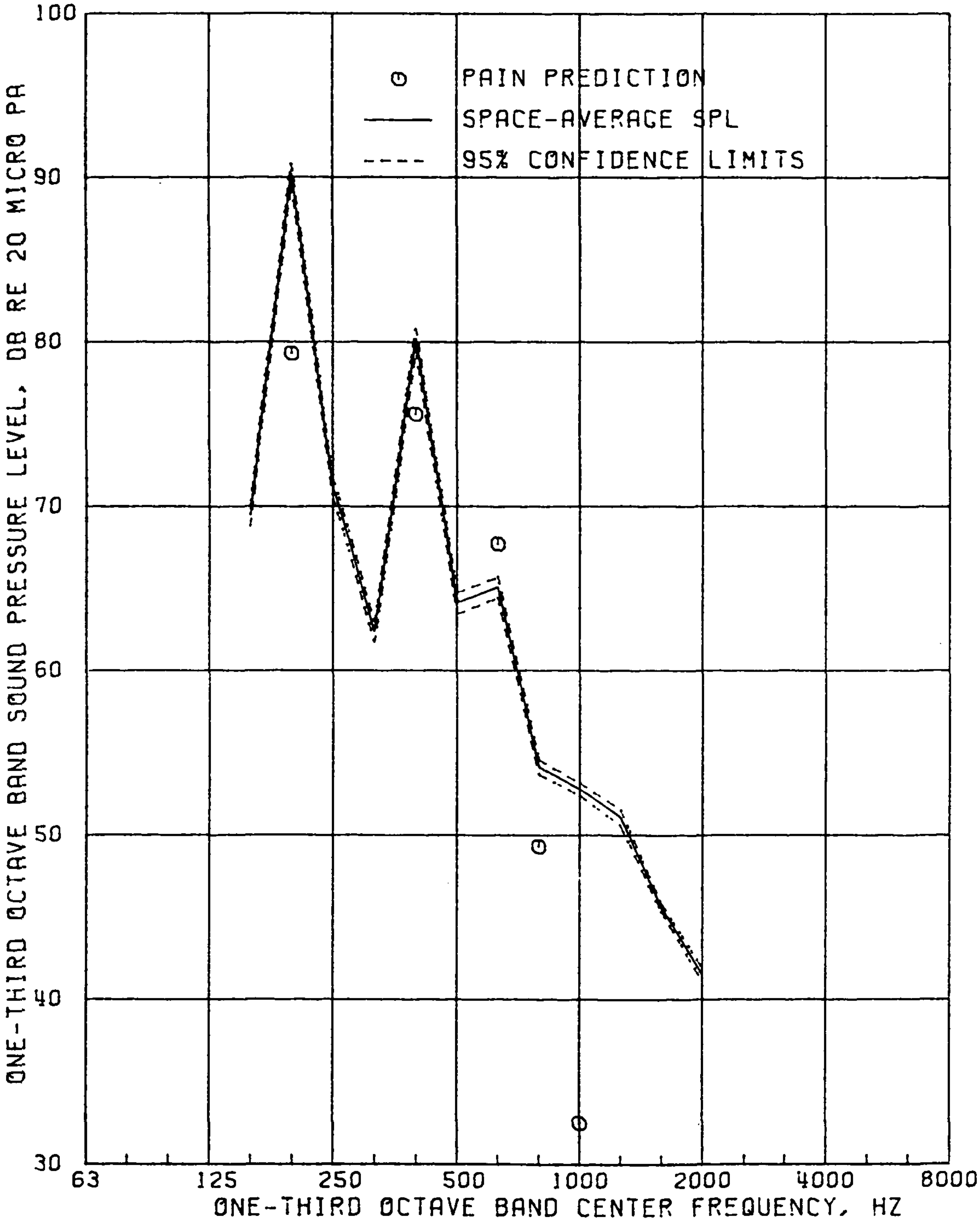

FIGURE E-17. COMPARISON OF PREDICTED AND MEASURED SOUND LEVELS IN CYLINDER INDUCED BY PROPELLER (MEAN AND 95% CONFIDENCE LIMITS) frequencies whereas the measured levels are associated with one-third octave bands. However the harmonic frequencies of 200, 400, 600, 800 and 1000 Hz are centered within the corresponding one-third octave bands so that there should be no filter cut-off problems.

The comparisons show that the predicted levels are generally lower than the corresponding measured one-third octave band space-average levels. The largest difference occurs in the highest order harmonic considered (1000 Hz) where the measured levels may be dominated by broadband noise rather than the discrete frequency component associated with the propeller blade passage sound.

A small number of parametric studies have been performed in order to assess the sensitivity of the analytical model to various factors. These studies were limited to considerations of the changes in trim and cylinder structural loss factors discussed previously. In summary, the trim structural loss factor was assigned a value of 1.0 and the cylinder structural loss factor was limited to a maximum value of 0.15. The resulting predicted interior sound levels are shown in Figure E-18. The effect of the changes of the loss factors was small except for the first harmonic at 200 Hz. The predicted level at this frequency now lies within 2 dB of the measured one-third octave band space-average value, instead of being 10 dB lower as shown in Figure E-17 for the initial calculations.

Further diagnostic analysis is highly desirable, particularly with respect to the model for the sidewall treatment, but such analysis was not possible in the present study.

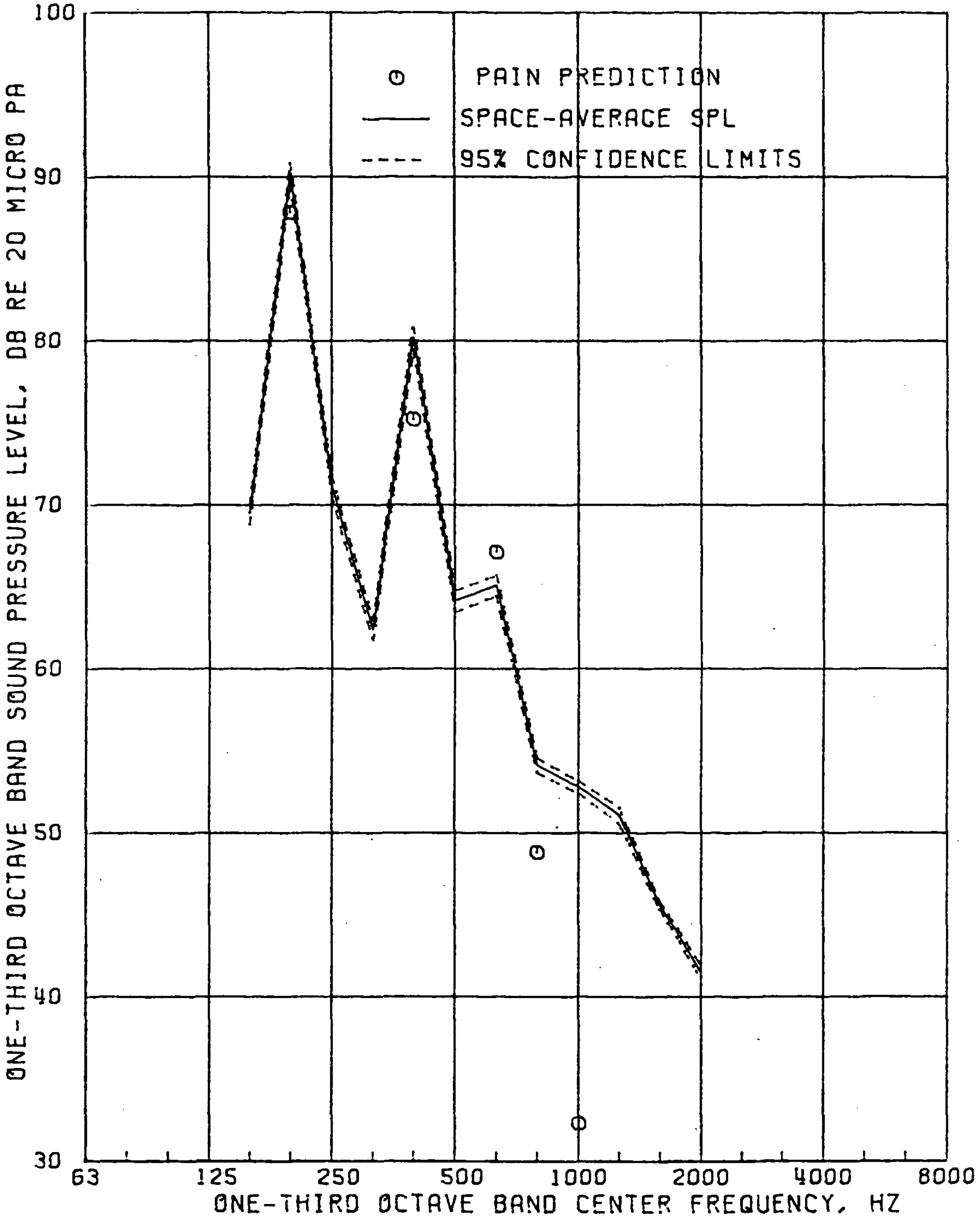

FIGURE E-18. COMPARISON OF PREDICTED AND MEASURED SOUND LEVELS IN CYLINDER INDUCED BY PROPELLER (TRIM LOSS FACTOR = 1.0, TOTAL STRUCTURAL LOSS FACTOR LIMITED TO 0.15 MAXIMUM)

Noise Reduction

In addition to predicting the transmission of propeller noise into an airplane fuselage, the analytical model also contains a capability for calculating the noise reduction associated with a reverberant incident sound field. This capability has been the subject of validation studies in earlier phases of the development of the analytical model [3,7]. Additional comparisons are discussed here.

Interior sound pressure levels were measured at two axial stations inside the cylinder, and average noise reductions computed for the two stations. The resulting noise reduction spectra are plotted in Figures E-19 and E-20. At frequencies of 160 Hz and above the two average spectra have similar values, as was the case in Figure E-8 for propeller noise excitation. There are, however, large differences in noise reductions for the two stations at frequencies of 80 and 100 Hz.

Space-average noise reductions for the cylinder as a whole were computed assuming that the sound field in the cylinder was symmetrical about the mid-point of the cylinder length. The space-average spectrum is shown in Figure E-21 with the range of measured values and in Figure E-22 with 95% confidence limits.

Figures E-21 and E-22 also contain the space-average noise reductions which were computed. It was assumed for these calculations that the trim structural loss factor was $\eta_T = 1.0$ and the structural loss factor η_r' was limited to a maximum value of 0.15. In addition, allowance was made for noise transmission through the end plates; the method used was the same as that in [7] and it was applied to the four lowest frequency bands, 80 to 160 Hz. Without this modification the analytical model would predict significantly higher noise reductions at low frequencies.

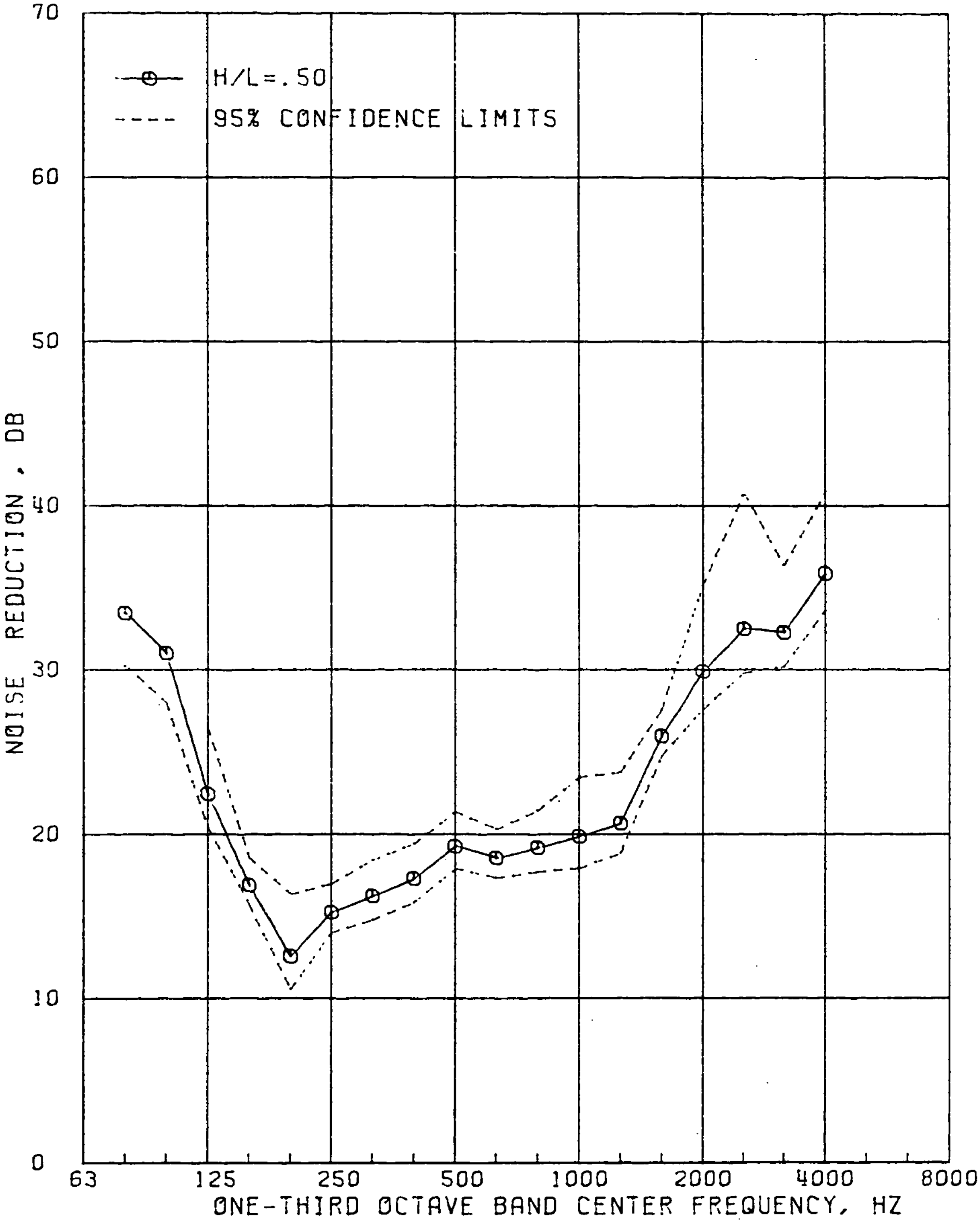

FIGURE E-19. AVERAGE NOISE REDUCTION MEASURED AT STATION AT 50% OF CYLINDER LENGTH

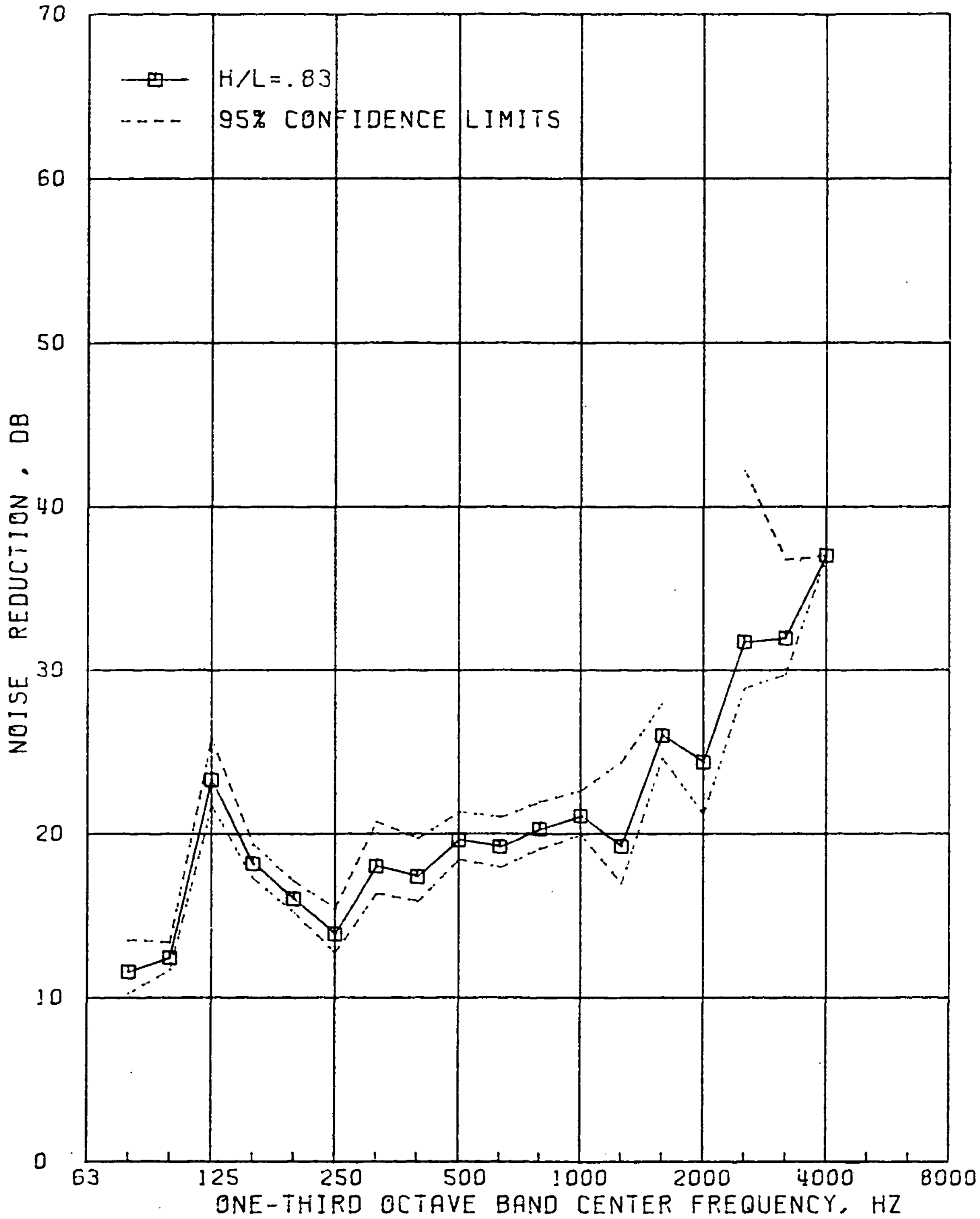

FIGURE E-20. AVERAGE NOISE REDUCTION MEASURED AT STATION AT 83% OF CYLINDER LENGTH

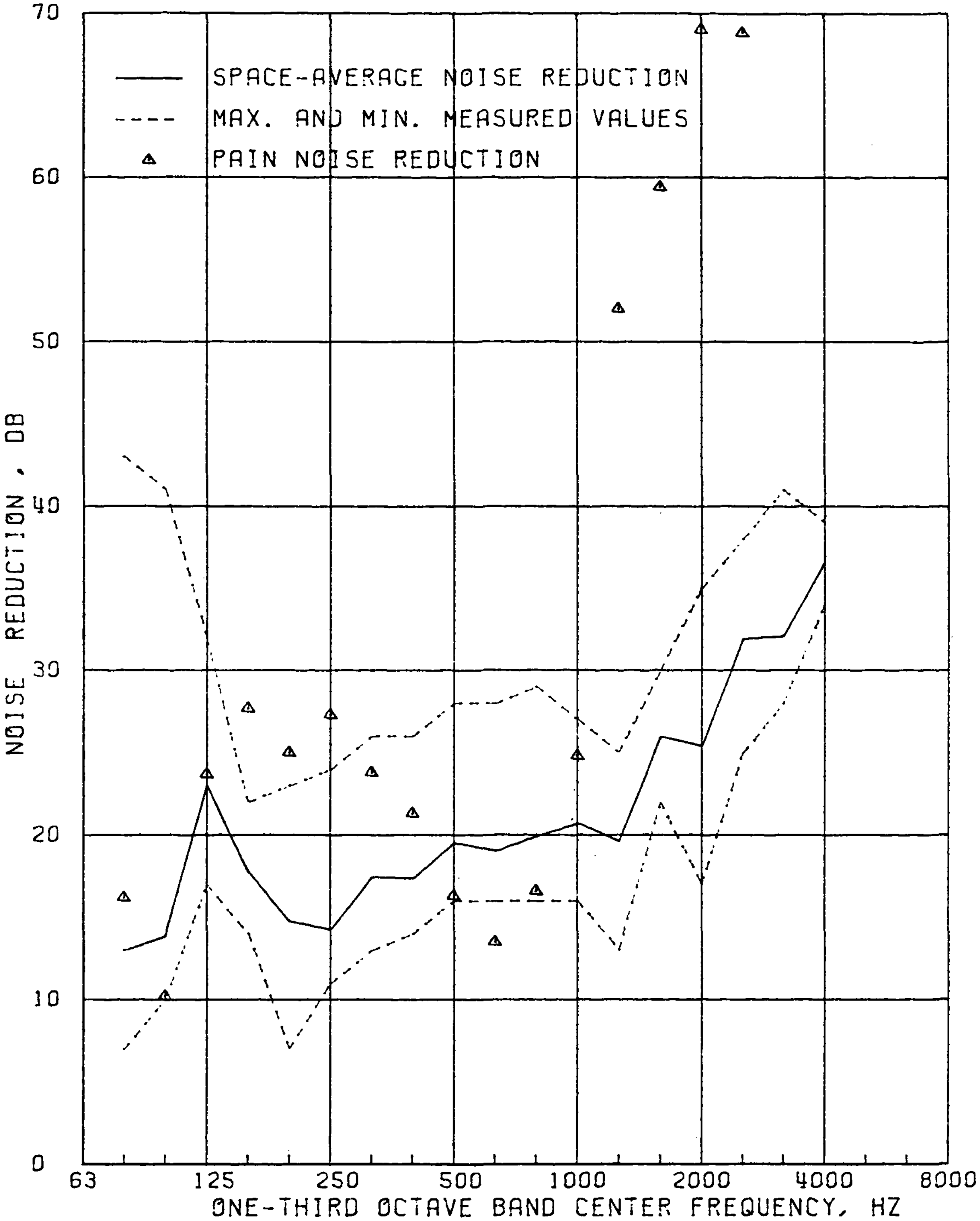

FIGURE E-21. COMPARISON OF MEASURED AND PREDICTED SPACE-AVERAGE NOISE REDUCTION FOR TEST CYLINDER (AVERAGE AND RANGE OF VALUES, TRIM LOSS FACTOR = 1.0. TOTAL STRUCTURAL LOSS FACTOR LIMITED TO 0.15 MAXIMUM)

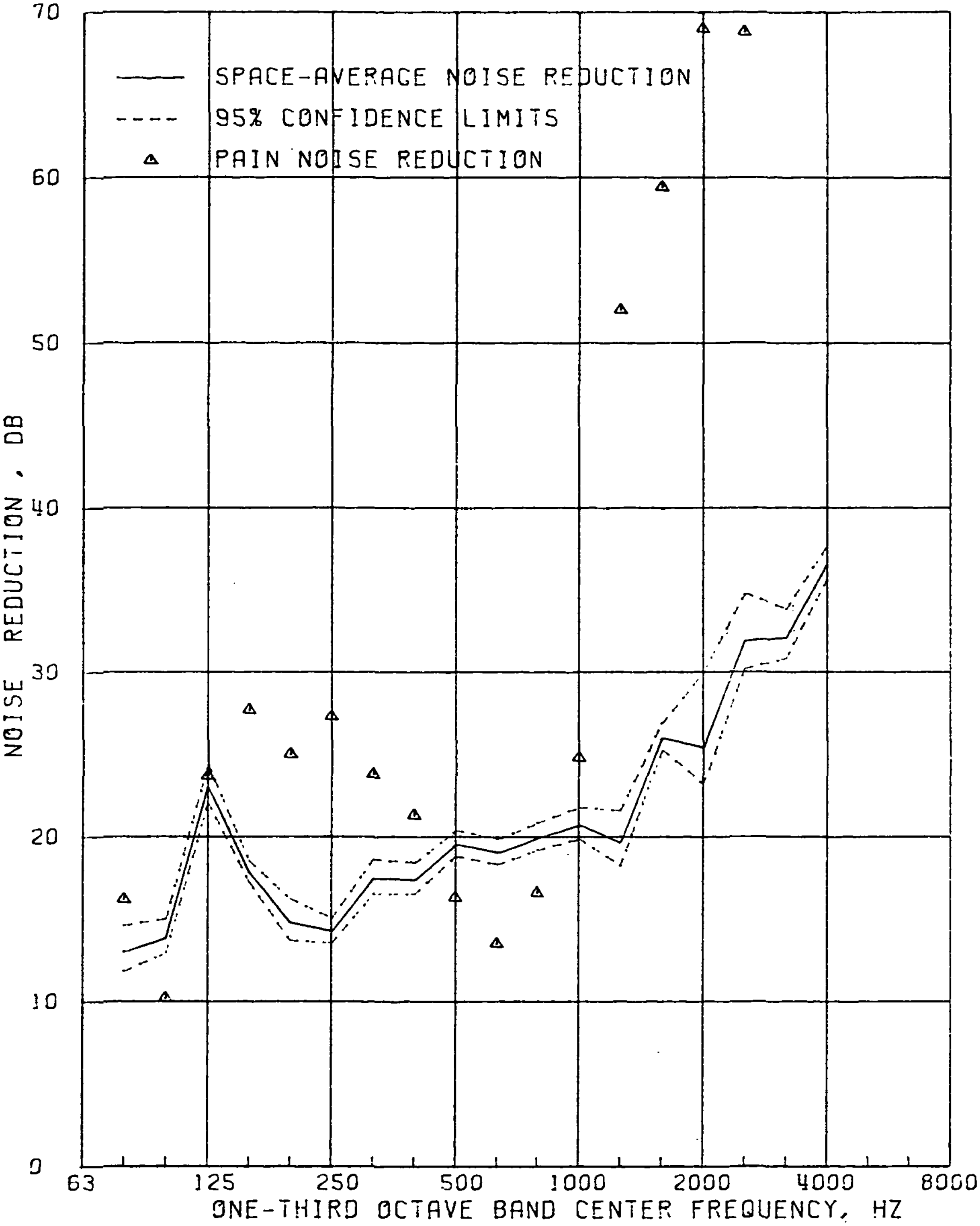

FIGURE E-22. COMPARISON OF MEASURED AND PREDICTED SPACE-AVERAGE NOISE REDUCTION FOR TEST CYLINDER (AVERAGE AND 95% CONFIDENCE LIMITS, TRIM LOSS FACTOR = 1.0, TOTAL STRUCTURAL LOSS FACTOR LIMITED TO 0.15 MAXIMUM)

The computer program assumes that no noise is transmitted through the ends of the cylinder, since such contributions are not usually important in aircraft. Furthermore, because of the directivity characteristics of propeller noise, the noise levels on the end plates of the test cylinder would be low when the cylinder was exposed to the propeller excitation. Thus, noise transmission through the end plates would be negligible in the propeller noise test. The contribution becomes significant only for reverberant field excitation.

The agreement between measured and predicted noise reductions is not as good as was the case for propeller noise excitation. The discrepancy between predicted and measured noise reductions at high frequencies was observed in previous data [7] where it was believed to be due to flanking paths through exposed stiffeners. There are no flanking paths of this type in the present test model. Two possible explanations for the discrepancy are (a) other flanking paths are present, and (b) the analytical model over-estimates the influence of the sidewall treatment.

The noise transmission measurements were repeated with the fiberglass treatment on the end plates increased from a thickness of 1.3 cm (0.5 inch) to 3.1 cm (2 inches). The resulting change in measured space-average noise reduction is shown in Figure E-23 which contains spectra associated with the two treatments. Figure E-23 contains corresponding predicted noise reduction spectra. The two figures show somewhat different trends with the predictions giving an increase in noise reduction in the frequency range 315 to 1250 Hz whereas the increase in measured noise reduction occurs mainly at frequencies above 800 Hz.

The predicted spectra in Figure E-24 are influenced directly by the analytical model for the fiber glass material on the end plates. Figure E-25 compares the acoustic loss factors computed

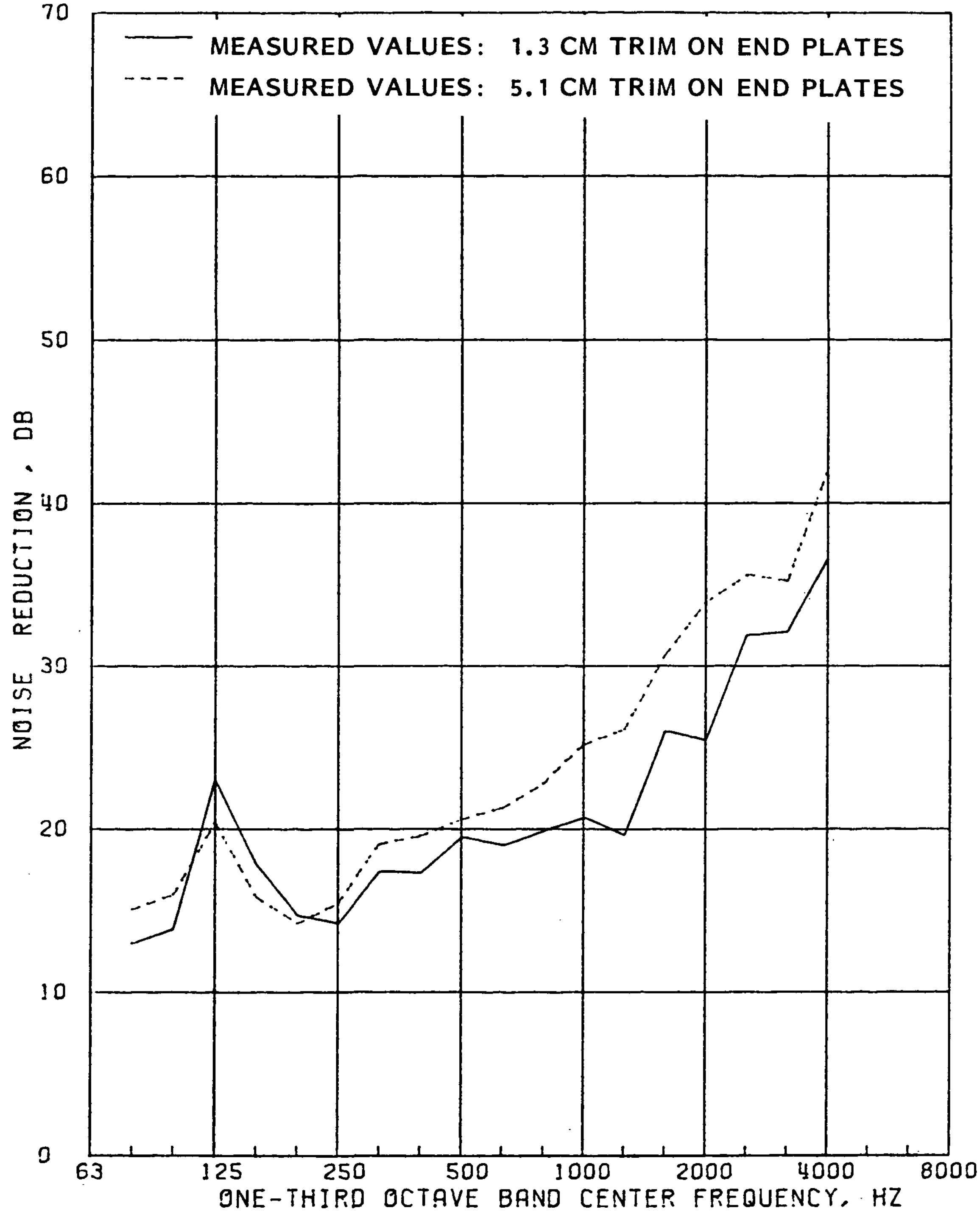

FIGURE E-23. MEASURED NOISE REDUCTIONS FOR CYLINDER WITH DIFFERENT THICKNESSES OF FIBERGLASS BATTS ON END PLATES

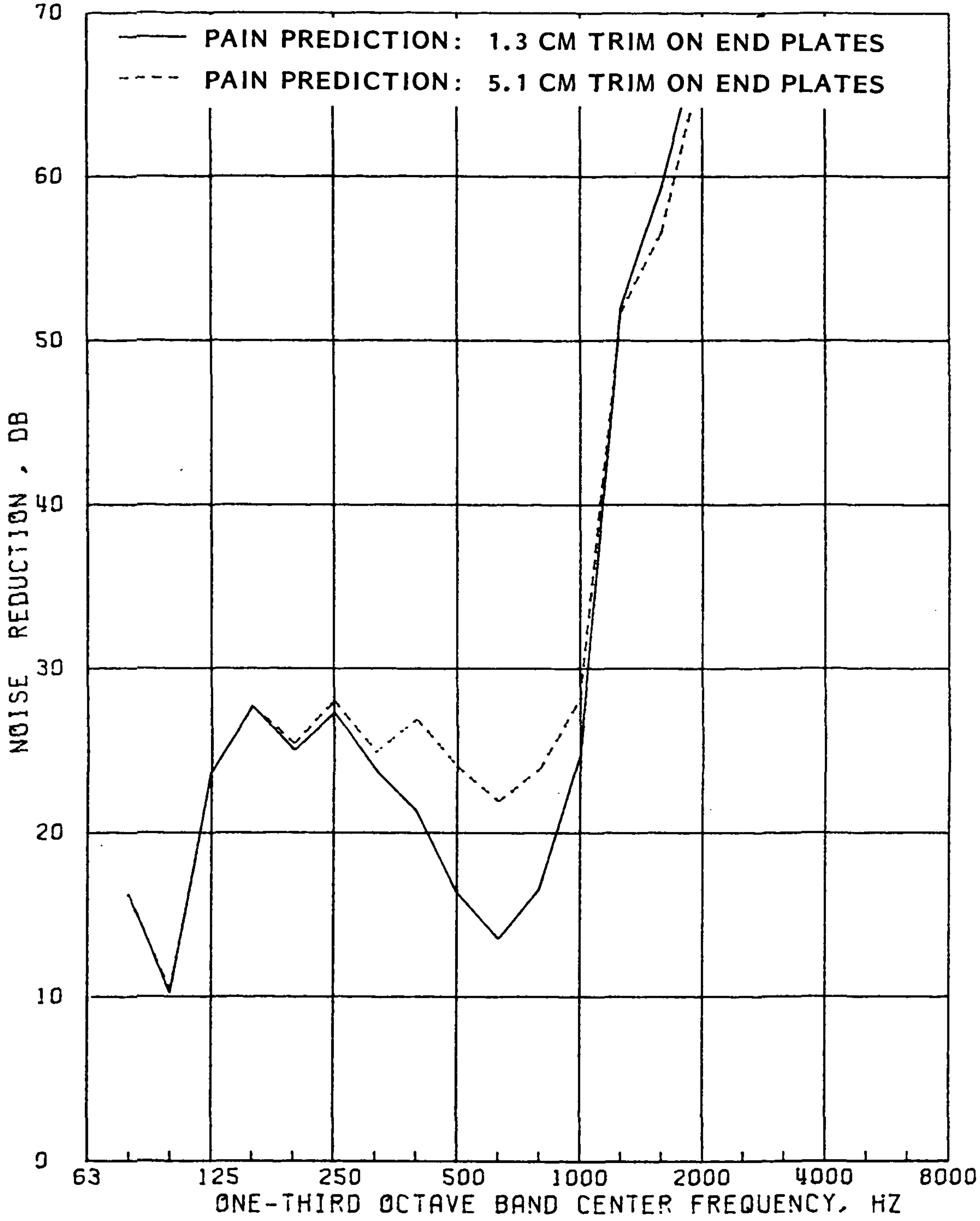

FIGURE E-24. PREDICTED NOISE REDUCTION FOR CYLINDER WITH DIFFERENT THICKNESSES OF FIBERGLASS BATTS ON END PLATES

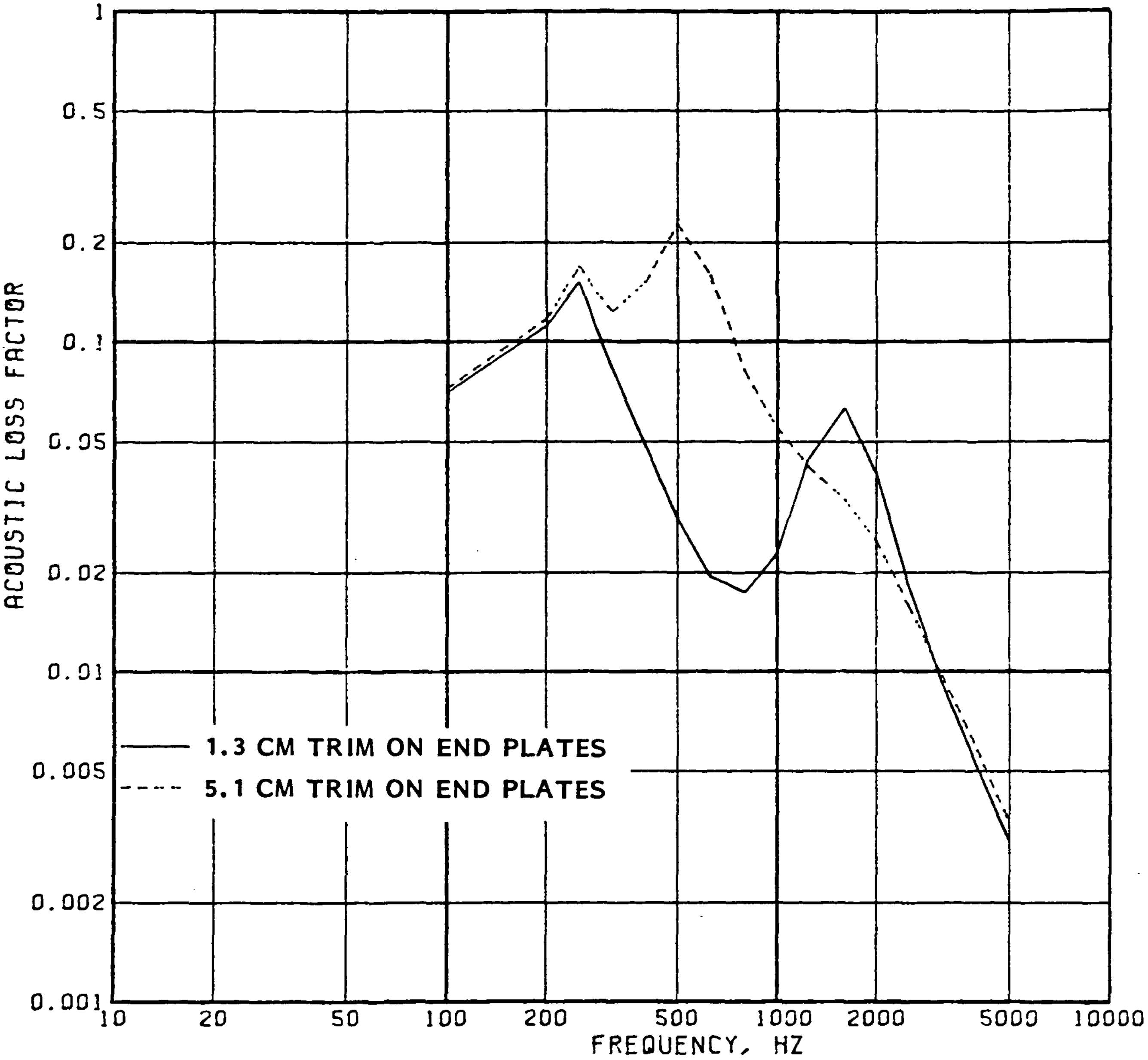

FIGURE E-25. PREDICTED ACOUSTIC LOSS FACTORS FOR CYLINDER WITH DIFFERENT THICKNESSES OF FIBERGLASS BATTS ON END PLATES for the interior of the cylinder for the two end plate treatments. The results show that a resonance-type effect predicted for the trim is shifted down in frequency from 1600 Hz for the 1.3 cm treatment on the end plates to 500 Hz for the 5.1 cm treatment.

General Comments

This brief discussion of validation studies for the analytical model has shown fairly good agreement between predicted and measured sound levels in a cylinder exposed to propeller noise excitation. The discussion has also identified several items for future study in order to improve the analytical model. For the propeller noise pressure field, the procedure for estimating pressure reflection effects should be reviewed. Also, the analytical model for relative phase between the upper and lower grids should be validated.

The present analysis represents the first time that the sidewall treatment has been incorprated as an integral part of the sound transmission model. As such, the analysis makes a major step in providing a comprehensive model for airplane interior noise. The validation studies indicate that some improvements to the sidewall treatment model are required in order to improve the agreement between predictions and measurements. It is recommended that these improvements be made.

APPENDIX F

LIST OF SYMBOLS

LIST OF SYMBOLS

A	Cylinder surface area, used in Eq.(4).
or	
A	Interior (cylinder & floor) surface area, used in conjunction with structural/acoustic coupling function $f'(n,r)$
A'	Transmitting area of cylinder without trim
$\bar{A}$	Exterior cylinder surface area
A_t	Transmitting area of cylinder with trim
$(A + A')$	Total transmitting area of cylinder, floor to floor
A_H^m	Amplitude of Fourier component of blocked propeller pressure signature at propeller harmonic H and grid location $m \equiv (k,\ell)$, see Eq.(43)
$\bar{A}_H^m$	Amplitude of Fourier component of free field propeller pressure at harmonic H and grid location $m \equiv (k,\ell)$
a	Radius of cylinder
a_H^m	Fourier series coeffficient of propeller pressure, for harmonic H at location m; see Eqs.(27),(29)
$a_o^m/2$	Mean propeller pressure amplitude at location m (defined in Eq.(28))
$\left.\begin{matrix}\text{arctan}_n\\ \text{arctan}_r\end{matrix}\right\}$	Functions defined in Section 3.3, Eq.(17), et seq
B	Number of propeller blades
BPF	Propeller blade passage frequency (Hz); $\text{BPF} = \frac{NB}{60}$

LIST OF SYMBOLS
(Continued)

b_n, b_r	Functions defined in Section 3.3, Eq.(17) et seq
b_H^m	Fourier series coefficient of propeller pressure for harmonic H at location m; see Eqs.(27),(29)
$C(j)$	Function defined in Eq.(76)
$Cin(z)$	Cosine integral; $Cin(z) = \int_0^z (1-\cos t)dt/t$
$C_{Mn}^{pr} C_{Mn}^{sr}$	Floor and shell generalized coordinates for structural mode $r \equiv (M,N)$; see Eqs.(46)-(49)
$C_{p_{bl}}(\bar{x} \mid \bar{x}';\omega)$	Cospectral density function of the blocked exterior pressure field
$C_p(\bar{x} \mid \bar{x}';\omega)$	Cospectral density function of the exterior pressure field
C_w, C_w^R, C_w^I	Trim parameter, derived from the trim transfer matrix, Eq.(A.8); $C_w = C_w^R + iC_w^I$
$C_x(\xi,\omega) C_y(\zeta,\omega)$	Cospectral density functions of the exterior pressure field in the axial and transverse directions respectively; see Eq.(60)
c_o	Speed of sound in air
c_n, c_r	Functions defined in Section 3.3, Eq.(17) et seq
c_ω	Constant percentage bandwidth parameter, where $\Delta\omega = c_\omega \omega$ [$c_\omega = 0.232$ for one-third octave bands]

LIST OF SYMBOLS
(Continued)

D_{nr}	Function defined in Section 3.3, Eq.(17) et seq
$E[\quad]$	Expected value of a function
$f'(n,r)$	Interior structural/acoustic coupling factor; see Eq.(45)
$\bar{f}'(n,r)=\bar{f}'(qi,r)$	Interior structural/acoustic coupling factor including effect of trim factor τ_t, see Eq.(52)
f_1	Frequency of propeller 1st harmonic; $f_1 = 1/T_o$ = BPF
f_H	Frequency of propeller harmonic H; $f_H = Hf_1$
f_{qm}	Acoustic/structural coupling factor in axial direction; see Eq.(57)
g_n, g_r	Functions defined in Section 3.2, page 3-11
H	Propeller harmonic order, used as superscript to denote functions evaluated at frequency ω_H
i	Acoustic mode number counter for fuselage cross-section modes, associated with mode $n \equiv (q,i)$
$I_1 I_2 I_3$	Integrals defined in Equations (63) and (70)-(73)
j	Circumferential location on fuselage wall, θ_j, a boundary point at which the acoustic eigenvector is evaluated (see Fig.C-2)

LIST OF SYMBOLS
(Continued)

$j_M^2(\omega)$	Structural joint acceptance function in axial direction
$j_N^2(\omega)$	Structural joint acceptance function in circumferential direction
$j_r^2(\omega)$	Structural joint acceptance in axial and circumferential directions; $j_r^2(\omega) \equiv j_{MN}^2(\omega) = j_M^2(\omega)\, j_N^2(\omega)$; see Eq.(58)
$j_r^{2\,rev}(\omega)$	Joint acceptance for reverberant/diffuse excitation
$\langle j^2(\omega)\rangle_r^{rev}$	Joint acceptance for reverberant excitation averaged over structural modes resonant in band $\Delta\omega$
k	Acoustic wave number, $k = 2\pi/\lambda$
or	
k	Axial non-dimensional coordinate for grid point; see Figure E-4
L	Fuselage structure length
L_p	Floor width (wall to wall)
ℓ	Circumferential non-dimensional coordinate for grid point; see Figure E-4)
ln_n, ln_r	Functions defined in Section 3.3, Eq.17 et seq
M	Number of axial half-wavelengths for structural mode $r \equiv (M,N)$

LIST OF SYMBOLS

(Continued)

M_r	Generalized modal mass, for structure mode r
$m \equiv (k,\ell)$	Grid point on surface of cylinder used for propeller noise predictions; see Figure E-4
or	
m	Average surface mass/unit area of cylinder
N	Structural mode counter, associated with mode $r \equiv (M,N)$
or	
N	Propeller rpm
N_n, N_r	Number of acoustic modes or structural modes in frequency band $\Delta\omega$
n	Symbolizes acoustic mode $n \equiv (q,i)$
or	
n	Number of circumferential wavelengths (or transverse half-wavelengths) in fuselage shell (or floor); see Eqs.46-49.
n*	Number of terms in displacement series for fuselage shell (or floor)
n_b, n_b'	Number of boundary points on the fuselage shell (or floor) at which the acoustic eigenvectors are defined
n_n	Modal density of acoustic modes
n_r	Modal density of structural modes

LIST OF SYMBOLS
(Continued)

$P(\omega_n)$	Probability distribution function for ω_n in $\Delta\omega$
$p(\omega_n)$	Probability density function for ω_n in $\Delta\omega$
$p_{bl}(\bar{x},t)$	Exterior pressure over the blocked (immobile) fuselage
$\langle p_{bl}^2 \rangle$	Band-limited mean square blocked pressure
$\langle p_i^2(\bar{\xi},\omega)\rangle_t$	Interior mean square pressure at location $\bar{\xi}$
$\langle p_i^2 \rangle_{s,t}$	Space-averaged band-limited mean square interior pressure
$\langle p_e^2 \rangle_{s,t}$	Space-averaged band-limited mean square exterior pressure for a reverberant field
$\langle p_n^2 \rangle_{s,t}$	Space-averaged band-limited mean square modal pressure, for nth mode in interior volume V
Q_H	Function defined in Section 3.2, Eq.(12)
q	Number of axial half-wavelengths for acoustic mode $n \equiv (q,i)$
r	Symbolizes structural mode $r \equiv (M,N)$
r_p	Radial distance from center of fuselage cylinder to the axis of rotation of the propeller.

LIST OF SYMBOLS

(Continued)

$R_{p_{bl}}(x\|x';\omega)$	Average cross correlation of the exterior blocked pressure over the fuselage
S	Absorbing surface area of fuselage sidewall
S_e	Absorbing surface area on each end surface (bulkhead)
$S_p(\omega)$	Power spectral density of exterior pressure
$S_{p_{bl}}(\omega)$	Power spectral density of exterior blocked pressure
$S_{p_{bl}}(\bar{x}\|\bar{x}';\omega)$	Cross spectral density of exterior blocked pressure
$Si(z)$	Sine integral; $Si(z) = \int_0^z \sin t.dt/t$
t	time
T	Period of rotation of propeller; $T = 60/N$
T_o, T_1	Period of propeller noise signature; $T_o = T_1 = (BPF)^{-1} = T/B$
u	In-plane axial displacement of cylinder wall (or floor)
V	Volume of cavity
v	Circumferential (or transverse) displacement of cylinder wall (or floor)
W_{diss}	Power dissipated on the cabin walls

LIST OF SYMBOLS
(Continued)

W_{in}	Net power inflow
$W^{int}_{rad}(\omega)$	Spectral density of power radiated by structure into interior acoustic space
$W^{int}_{abs}(\omega)$	Spectral density of power absorbed on inner wall of the space from interior acoustic field
w	Cylinder wall (or floor) normal displacement
x	Transverse coordinate; see Figure 1
$\bar{x}$	Location on exterior surface of fuselage
$\bar{x}_m$	Location of grid point on exterior surface of fuselage
$x_1 x_2 x_3$	Local coordinate systems; see Figure E-4
y	Vertical coordinate, relative to fuselage centerline (see Figure 1)
z	Axial coordinate, relative to forward end of the fuselage structure (of length L); see Figure E-4
z_k	Axial coordinate for grid point k, see Figure E-4
z_p	Location of propeller relative to the forward end of the fuselage structure (of length L); see Figure 1)

LIST OF SYMBOLS
(Continued)

$\bar{\alpha}$	Band average absorption coefficient
γ	Incidence angle between propeller and location $\bar{x}_m$; see Figure 2 (in degrees)
$\Delta = \frac{\pi a}{18}$	Grid spacing for propeller noise predictions
$\Delta A = \Delta^2$	Area associated with each grid point; see Figure E-4
$\Delta\omega$(radians/sec)	Frequency band of width $\Delta\omega = c_\omega \omega$ $n<\Delta\omega$ symbolizes modes resonant below band $n\varepsilon\Delta\omega$ symbolizes modes resonant inside band $n>\Delta\omega$ symbolizes modes resonant above band
$\delta(\ )$	Delta function
$\varepsilon_n = V/\int_V \phi_n^2 d\bar{v}$	Acoustic mode normalization factor
ε_q	Acoustic mode normalizing factor in axial direction (see Eq.C.11)
ζ	Transverse coordinate; see Section 3.6
η_n	Acoustic mode loss factor
η_r	Structural mode loss factor
η_r'	Structural loss factor, including damping due to trim; Eq.(82)
η_r''	Internal radiation loss factor, due to closely coupled structural and acoustic modes; Eq.(83)

LIST OF SYMBOLS

(Continued)

$\bar{\eta}_n$	Average one-third octave band acoustic mode loss factor
$\bar{\eta}_r = \eta_r' + \eta_r'' + \eta_{rad}^{ext}$	Average one-third octave band structural mode loss factor
η_r^{struc}	Average one-third octave band structural loss factor
η_r^{rad}	Average one-third octave band radiation loss factor
$\eta_{rad}^{int}, \eta_{rad}^{ext}$	Average one-third octave band internal and external radiation loss factors defined after Eq.(19)
θ	Angular coordinate, relative to fuselage bottom centerline; see Figure 1
θ_ℓ	Angular coordinate for grid location (k,ℓ)
θ_c	Angle at which fuselage shell/floor joint is located
θ_j	Angle θ for point j on fuselage wall, a boundary point for the acoustic eigenvectors
$\theta_{1j}\theta_{2j}$	Angles defining mid-points between boundary point j and adjacent boundary points
ξ	Axial coordinate; see Section 3.6
or	
ξ	Conductance for trim on end surface of cylinder interior

LIST OF SYMBOLS
(Continued)

$\bar{\xi}$	Interior cavity location
ξ_e	Conductance for trim on cylinder (fuselage) sidewall
ρ	Density of air inside the cylinder
ρ_o	Density of air outside the cylinder
τ	Time delay for cross-correlation
or	
τ	Acoustic transmission coefficient for diffuse field excitation; $\tau = \tau_f + \tau_R$
τ_f	Field incidence transmission coefficient for mass controlled panels; defined in Eq.(20)
$\tau_{mL} = \left(\frac{2\rho c_o}{m\omega}\right)^2$	Mass law sound transmission coefficient
τ_t	Trim transmission coefficient, defined in Eq.(A.22)
τ_R	Resonance transmission coefficient for diffuse field, defined in Eq.(19)
$\Phi_G(i)$	Generalized mass for two-dimensional acoustic mode i, defined in Appendix C
ϕ	Angular position of propeller hub relative to fuselage bottom centerline; see Figure 2
ϕ_H^m	Phase of Fourier component of propeller pressure signature at propeller harmonic H and grid location $m \equiv (k,\ell)$

LIST OF SYMBOLS
(Continued)

$\phi_n(\bar{\xi}) \equiv \phi_{qi}(\bar{\xi})$	Mode shape, or eigenfunction, of the nth mode of the cavity at location $\bar{\xi}$
$\phi_i(\theta_j)$	Mode shape of ith acoustic mode of the fuselage cross-section evaluated on the fuselage wall at location j, angle θ_j
$\Psi_G(r,H)$	Generalized modal forcing function due to propeller noise, mode r at propeller harmonic H; see Section 3.4
$\psi^r(\bar{x})$	Mode shape, or eigenfunction, of the rth mode of the structure, at location $\bar{x}$
$\psi_p^r(z,x)$	Floor displacement in structure mode r
$\psi_s^r(z,\theta)$	Fuselage shell displacement in structure mode r
ω	Angular frequency (rads/sec)
ω_H	Angular frequency of propeller harmonic H
ω_n	Acoustic mode resonance angular frequency
ω_r	Structure mode resonance angular frequency
$\langle \quad \rangle_{s,t}$	Band-limited, space-averaged and time-averaged value

1. Report No. NASA CR-3813	2. Government Accession No.	3. Recipient's Catalog No.
4. Title and Subtitle PROPELLER AIRCRAFT INTERIOR NOISE MODEL		5. Report Date July 1984 6. Performing Organization Code
7. Author(s) L. D. Pope, E. G. Wilby, and J. F. Wilby		8. Performing Organization Report No. 5058
9. Performing Organization Name and Address BOLT BERANEK AND NEWMAN INC. 21120 Vanowen Street Canoga Park, CA 91303		10. Work Unit No. 11. Contract or Grant No. NAS1-15782
12. Sponsoring Agency Name and Address National Aeronautics and Space Administration Washington, DC 20546		13. Type of Report and Period Covered Contractor Report 14. Sponsoring Agency Code

15. Supplementary Notes

Langley Technical Monitor: William H. Mayes

16. Abstract

An analytical model has been developed to predict the interior noise of propeller-driven aircraft. The fuselage model is that of a cylinder with a structurally-integral floor. The cabin sidewall is stiffened by stringers and ring frames, and the floor by longitudinal beams. The cabin interior is covered with a sidewall treatment consisting of layers of porous material and an impervious trim septum. Representation of the propeller pressure field is utilized as input data in the form of the propeller noise signature at a series of locations on a grid over the fuselage structure. Results obtained from the analytical model are compared with test data measured by NASA in a scale model cylindrical fuselage excited by a model propeller.

17. Key Words (Selected by Author(s)) Aircraft Interior Noise Propeller Noise Cylinder Noise Reduction Acoustic Power Flow	18. Distribution Statement Unclassified - Unlimited Subject Category 71

19. Security Classif. (of this report) Unclassified	20. Security Classif. (of this page) Unclassified	21. No. of Pages 166	22. Price* A08

*For sale by the National Technical Information Service, Springfield, Virginia 22161.